Final Report

Flow Visualization of Forced and Natural Convection in Internal Cavities

John Crepeau and Hugh M. McIlroy, Jr.
University of Idaho

Donald M. McEligot, Keith G. Condie and Glenn McCreery
Idaho National Engineering and Environmental Laboratory

Randy Clarksean
Clarksean and Associates

Robert S. Brodkey and Yann G. Guezennec
Ohio State University

January 2002

EMSP Project Number 60144

Flow Visualization of Forced and Natural Convection in Internal Cavities

John Crepeau and Hugh M. McIlroy, Jr.
University of Idaho

Donald M. McEligot, Keith G. Condie and Glenn McCreery
Idaho National Engineering and Environmental Laboratory

Randy Clarksean
Clarksean and Associates

Robert S. Brodkey and Yann G. Guezennec
Ohio State University

January 2002

Project Duration: September 1997-September 2001

Principal Investigator:
John Crepeau
Associate Professor of Mechanical Engineering
University of Idaho
P.O. Box 50778
Idaho Falls, Idaho 83405
Phone: (208)282-7955
Fax: (208)282-7950
Email: crepeau@uidaho.edu

Final report prepared for the
U.S. Department of Energy
Environmental Management Science Program
Under contract number DE-FG07-97ER14829
EMSP Project number 60144

Executive Summary

The goal of this program was to develop innovative flow visualization methods and reliable predictive techniques for the energy, mass, and momentum transfer in the presence of surface reactions for the passivation treatment operations of spent nuclear fuel (SNF) elements. A generic SNF canister, to store high- and medium-enriched fuels, was developed to serve as a common experimental configuration.

A unique flow visualization technique was developed to model a reaction between the passivating oxygen gas and uranium hydrides found on corroded areas of wet-stored SNF elements. In the experiments, hexanoic acid and sodium metal simulated the oxygen and uranium hydride respectively. The hexanoic acid and sodium metal reacted to form hydrogen, the same by-product of the passivation reaction. The hydrogen is buoyant compared to the surrounding fluid and therefore rises. To observe the effects of the reaction on the flow field, dye was injected upstream of the sodium. The experiments showed that the rising hydrogen behaved similarly to buoyant plumes, such as those observed in open fires or gases exiting a smokestack. The hydrogen entrained the surrounding fluid, introduced velocity fluctuations and instabilities into the flow, and enhanced fluid mixing. The entrainment caused the dye filaments to stretch and bend, and the buoyant hydrogen created counter-rotating vortices in the flow field that straddled the reaction site. While the hydrogen convected fluid away from the upstream portion of the reaction site and created vortices, these same vortices convected surrounding fluid into the downstream portion of the reaction. High resolution photographs contained in the report document this behavior. It was determined that a local surface reaction can affect the surrounding flow field.

Experiments were also conducted with the INEEL Matched Index of Refraction facility to study the overall flow field of the generic SNF canister. The canister had a perforated basket support plate through which an inlet pipe transported the passivating gases, and experiments were conducted on the perforated support plates with 50, 8, and 4 percent open areas. With the 50 percent open area, the flow was similar to a submerged impinging jet, with formation of a large vortex and entrainment and recirculation through the holes of the plate. With the 4 and 8 percent open area plates, recirculation regions arose downstream of the plate, and two main recirculation zones formed upstream of the plate. Flow did not reenter the inlet plenum through the smaller open area plates as it did with the 50 percent open area plate. The flow with the smaller holes in the support plate was similar to a confined impinging jet.

Velocity and turbulence measurements included the mean distributions of radial and axial components and their root-mean-squared fluctuations. The rms radial velocity fluctuations were considerably larger than the rms axial fluctuations. Large values of the radial fluctuations were observed in the wall jet, and moderate values were observed in its wake. Moderate to high values also appear near the perforated support plate in the region directly affected by the recirculating eddy. Local turbulent intensities were observed to be on the order of 100 percent or greater. The results show that flow in the plenum region of the canister upstream of the perforated support plate is sensitive to the inlet flow considerations. Downstream of the plate, the flow relaminarizes as it flows axially over the SNF elements. It is clear that despite the conceptual simplicity of the canister design, the overall flow pattern within the canister is very complex. An uneven flow distribution near the surface of the elements may lead to uneven passivation treatment of the elements.

Various numerical models were developed to analyze the complex nature of flow in the SNF canisters. Two- and three-dimensional models were developed to assess different flow features. The general-purpose code provided adequate results for the simulation of the low Re pipe flow. Agreement between the measured and predicted results was adequate, but refinements to the model could lead to improved comparisons. Modeling results that depended on inlet flow conditions to the plenum were found to be very sensitive to the assumptions made to the inlet pipe flow conditions. The selection of inlet boundary conditions is important to accurately predict turbulent flow conditions for these complex geometries. The modeling results are very sensitive to the type of turbulence model used for the simulations. Extremely large variations in the flowfield were noted for the different models. The most realistic results were obtained with a low Reynolds number turbulence model with accurate upwinding schemes. Low-order upwinding schemes and poor assumptions for the inlet flow profiles lead to drastic changes in the results.

It is necessary to include the details of the holes in the plate within the numerical model. It may be possible to develop a “porous plate” model for disperse holes, but model limitations may make it difficult to accurately model a wide range of design options. For example, if such a model impeded re-entrant flow into the plenum region, such a limitation may not detect situations where such flow truly exists. If a porous plate model were developed it would have to be developed with care to insure the appropriate physics are properly considered. Numerical convergence is slow for the three-dimensional flow fields modeled. The order of magnitude changes in the velocity field across the computational domain make it difficult to obtain fast convergence. As the next generation of computing platforms is developed, it will be easier to include the necessary details to analyze the details of the flowfield. More uniform flow up past the fuel elements will be obtained through the use of a plate that restricts the flow and does not allow it to re-enter the plenum region. Detailed analyses and testing would have to be conducted to truly assess the uniform characteristic of the flow.

Table of Contents

Executive Summary i

Nomenclature iv

1. Introduction 1

2. Generic Fuel Canister 3

3. Flow in a Model SNF Passivation Canister 5

4. Flow Over a Flat Plate With a Surface Reaction 13

5. Matched Index of Refraction Studies 28

6. Numerical Models of Flow in the SNF Canister 63

7. Conclusions and Recommendations 78

8. References 84

Nomenclature

{ }	function of
A_{cs}	cross-sectional area
D	tube diameter
D_h	hydraulic diameter, $4 A_{cs} / P$
f	frequency
g	acceleration of gravity
g_c	units conversion factor, e.g., 1 kg m /(N s^2), 32.174 (lbm/lbf)/(ft/sec^2), etc.
H	spacing between surfaces
k	turbulent kinetic energy
L	length
$\dot{m}$	mass flow rate
P	wetted perimeter
p	pressure
p_h	pitch
r	radial coordinate; r_o, canister wall radius
R	canister wall radius
s	spacing from jet inlet to impingement plate
T	absolute temperature
t	thickness
U	time-mean axial velocity component
u'	rms axial velocity fluctuation
u_τ	friction velocity, $(g_c \tau_w / \rho_w)^{1/2}$
V	time-mean radial velocity component (also U_r)
V_b	bulk or mixed-mean velocity
v	radial velocity fluctuation
v'	rms radial velocity fluctuation
w	local circumferential velocity component
W	time-mean circumferential velocity component
x	axial coordinate

y	coordinate perpendicular to the wall; also horizontal distance from centerline in experiment
z	vertical location in experiment

Non-dimensional quantities

K_p	streamwise pressure gradient, $(\nu/(\rho\, u_\tau^3))\, g_c\, dp/dx$
K_v	acceleration parameter, $(\nu/V_b^2)(dV_b/dx)$
L^+	length, $L/(r_w\, Re)$
Re	Reynolds number, $4\, \dot{m} / \Pi\, D\, \mu$ for tube; $Re_{D,h}$, based on hydraulic diameter, $V_b D_h/\nu$
St	Strouhal number, e.g., fD/U
u^+	streamwise velocity component, U/u_τ
x^+	axial distance, $x/(r_w\, Re)$
y^+	wall distance coordinate, $y\, (g_c\, \tau_w / \rho_w)^{1/2} / \nu_w$

Greek symbols

α	coefficient of thermal expansion
ε	dissipation of turbulence kinetic energy
γ	intermittency
λ	wave length
μ	absolute viscosity
ν	kinematic viscosity, μ/ρ
ρ	density
τ	shear stress
τ_w	wall shear stress

Subscripts

b	evaluated at bulk or mixed-mean temperature
c	centerline
h	hole
in	inlet
w	wall, evaluated at wall temperature

1. INTRODUCTION

The goal of this research program was to develop reliable predictive techniques for the energy, mass (including chemical reactions) and momentum transfer in drying, passivation and transfer operations of Spent Nuclear Fuel (SNF) from wet to dry storage. Such techniques were needed to assist in design of transfer and storage systems, prediction of the performance of existing and proposed systems and safety evaluation of systems as necessary at later dates. The goal of the present project was to provide the scientific knowledge required to develop numerical predictive methods treating the key flow phenomena in generic simulations of drying and passivation problems in Environmental Management. The objective of the tasks was to obtain fundamental measurements of the basic velocity and turbulence fields in generic idealizations of flow processes in SNF canisters during transfer and/or storage. These operating conditions give typically low Reynolds number flows.

A wide variety of fuel element geometries are accommodated in the storage of spent nuclear fuel. The fuel may have high-, medium- or low-enrichment so criticality considerations affect the number of fuel elements that can be stored in a single fuel basket or canister. Typically, only a few high- or medium-enriched elements can be stored in one basket whereas fuel elements with low-enrichment can be packed densely, approaching the appearance of arrays in a shell-and-tube heat exchanger. Element shapes may be circular rods, annuli, plates, squares, trapezoids, hexagons, etc. (Figure 1). Proposed canister sizes range from 14 to 24 inches (36 to 60 cm) with lengths of ten to fourteen feet (3-4 m). Typically, elements or assemblies are placed in baskets for dry storage, with drain holes in the basket support plates at the bottom. The hole pattern gives an open area ratio of three to nine percent, depending on the design. The number of baskets vertically in a canister depends on the lengths of the fuel elements being stored. Consequently, there is no one generic fuel element/assembly and no single generic fuel storage configuration.

One can, however, identify generic flow phenomena and paths. For example, in a passivation and/or drying system once suggested with flow arranged to pass from one end of a canister to the other (as in one earlier Hanford concept), the sequential flow paths would be: (1) Inlet downflow through a tube; (2) an impinging jet, spreading radially in a semi-confined region (formed between the bottom of the canister and the bottom support plate of the basket); (3) flow through a perforated

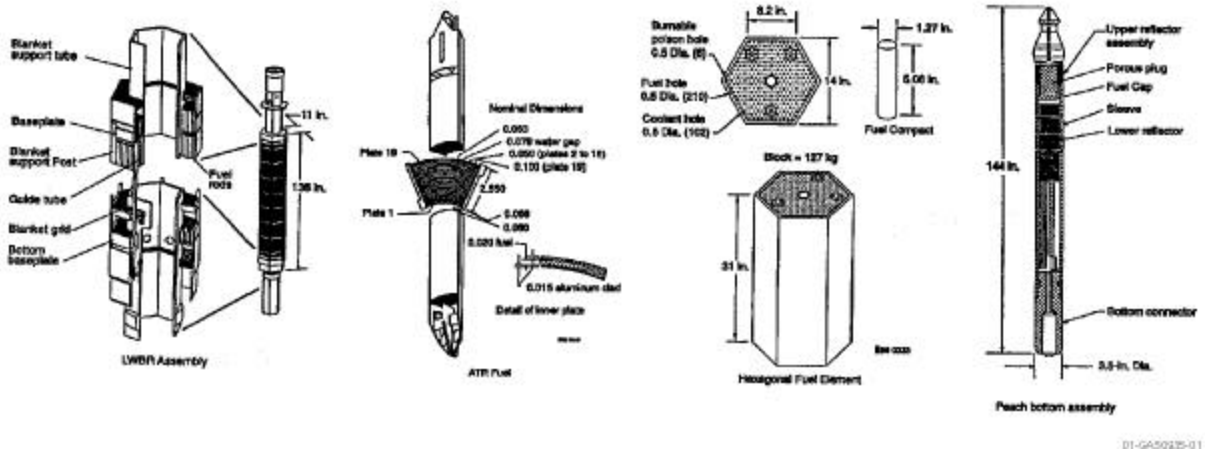

Figure 1. Examples of fuel elements considered for storage in SNF canisters.

plate, which is the bottom portion of the support basket; (4) vertical parallel flow paths around and between the fuel elements/assemblies; and (5) contraction into an exit.

The passivation and/or drying of the fuel is accomplished by convective mass transfer from the gas flow through and around the fuel elements. Distribution (or maldistribution) is determined by the relative flow resistances of all the paths. While this concept apparently has not been selected for application, it provides an excellent example of the coupled, complex phenomena which may be present in canister flows.

For effective passivation of potential pyrophoric reactions, a design aim would be to control and distribute evenly, high mass transfer rates to the fuel elements. These rates will depend on the flow pattern and turbulence levels in the vicinity of the elements. As noted in Figure 2, the fluid mechanic design for optimizing this process leads to a sequence of questions concerning the turbulence levels and flow patterns from the reacting surface to the inlet flow. In order to solve these questions several fundamental flow features are involved. First, one needs to determine the fluctuating velocity components in low Reynolds number turbulent or transitioning flow in a tube. Then, the turbulent transport and possible laminarization of a semi-enclosed impinging jet flow must be investigated. Finally, low Reynolds number flow through an array of holes (the basket support plates), and the decay of turbulence around an array of fuel elements must be known.

These features can be considered to be the generic flow phenomena of interest in the fluid physics of SNF transfer and storage. Despite extensive literature on impinging jets and flows in arrays, fundamental measurements of these phenomena at the conditions appropriate for some proposed SNF applications are meager to non-existent.

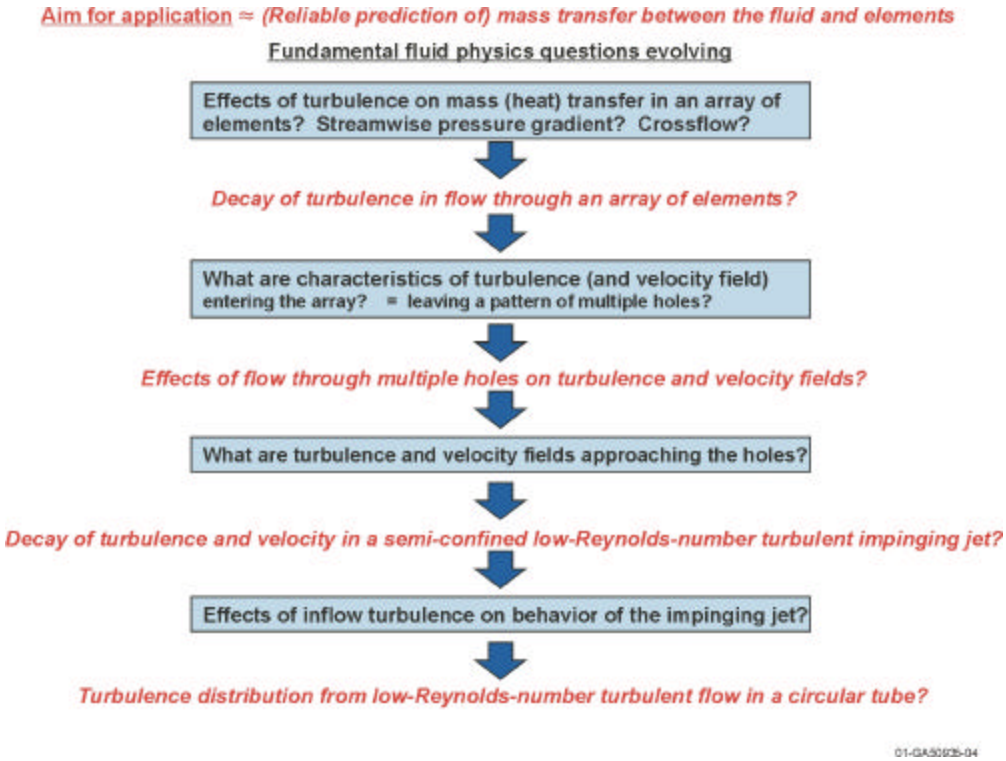

Figure 2. Identification of fundamental questions and flow phenomena in the fluid physics of SNF canisters.

2. GENERIC FUEL CANISTER

Although there is no single spent fuel storage configuration, one can identify generic flow phenomena and paths. Our research group developed a generic idealization of a combined drying and passivation (surface oxidation) approach, representing a section of a vertical cylindrical canister containing baskets of SNF elements. This simulation includes flow phenomena that occur in canisters for high-enrichment and medium-enrichment fuels, where fuel element spacing in the canister is increased as compared with low enrichment fuel. A steady flow of helium plus oxygen passivation gas is introduced at the bottom of the canister via a central tube from the top. Fluid spreads radially near the (circular) bottom canister wall and then flows through an array of holes in the perforated basket support plate. Fluid then flows around the elements and out the top. Dimensions and flow rates for the idealized situation are within the ranges for typical drying canisters. Approximate calculations have identified the ranges of values of flow parameters needed to determine the flow regimes occurring in practice.

This is an idealized description that has been developed for a geometry which induces the generic flow phenomena expected in typical SNF canisters, with provision for inflow to simulate purge gas flow, including an oxidizing component for passivation of uranium hydride surfaces. Initial models correspond to sparse loading of simulated elements as for highly- and moderately-enriched fuels. A perforated plate is employed to simulate characteristics of flow through the support plates of baskets in canisters. The idealization (Figure 3) was chosen to have a canister diameter of 18 inches (46 cm) and a basket length of about four feet (1.3 m). A long "dip tube" of one inch diameter (2.5 cm) serves as the inlet for the drying/passivation gas. It is recognized that current canisters may not have this configuration but comparable passages for circulation have been suggested in some proposed designs. Consequently, comparable generic phenomena could be expected to occur. Suggested design flow rates for the earlier hypothesized application indicate that the Reynolds number in the inlet tube would be expected to be between 2500 and 5000, i.e., relatively low. The distance between the basket support plate and the bottom of the canister was taken to be two inlet diameters (2 in. or 5 cm). For convenience in physical and numerical modeling, while retaining the key flow phenomena, symmetry and circumferential periodicity were employed to the extent possible.

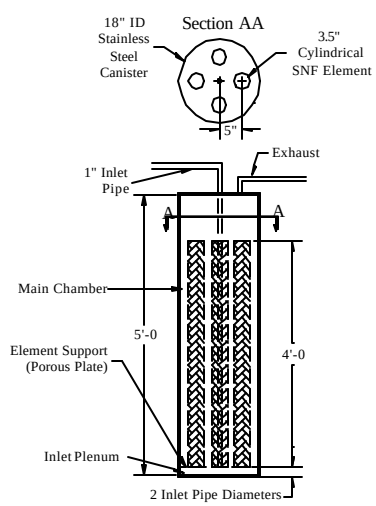

Figure 3. Schematic diagram of idealized SNF canister for study of generic flow processes occurring in drying and/or passivation.

For this idealization, at Re = 2500 the governing nondimensional parameters would be given approximately as shown in Table 1.

Table 1. Nondimensional parameters for the generic SNF canister.

Inlet circular tube	$Re \approx 2500$; $L/D \approx 80$
Axisymmetric impinging jet	$Re_{jet} \approx 2500$; $s/D \approx 2$; $H/D \approx 2$; $R/D \approx 6$
Perforated bottom support plate	$Re_{hole} \approx 40\text{-}160$; $p_h/D_{hole} \approx 4$; $t/D_{hole} \approx 1$
Array of fuel elements	$Re_{D,h,avg} \approx 70$; $L/D_h \approx 6$; $p/D_{element} \approx 2$ $L^+ \approx 0.4$; "Equivalent" $K_v \approx 0.02$; $K_p \approx -0.11$

Scientific needs

As noted, despite the wide range of previous work on individual fluid physics phenomena occurring in these generic problems, a number of scientific needs remain. These needs lead to the objectives and tasks being addressed in the present project. New fundamental experimental measurements needed include:

- Determination of the decay of turbulent fluctuations in the outflow of a low-Reynolds-number impinging jet along a semi-confined wall

- Determination of the decay of turbulence (relaminarization) in flow around a rod bundle

- Determination of the overall flow pattern and time-resolved distributions of mean velocity components and turbulent fluctuations from the central inlet tube through the vessel

- Determination of typical paths of (simulated) oxidizing molecules from introduction until interaction with a surface

Engineering needs

To develop useful, reliable predictive techniques for describing flow and turbulence fields plus related heat and mass transfer in applications to SNF canisters in general,

- Computer codes available or proposed to address heat and mass transfer in SNF canisters must be assessed by comparison to careful measurements -- at the (non-dimensional) conditions of the applications -- of the fundamental phenomena described above.

- Suitable computer codes must be improved or developed to treat successfully any significant discrepancies observed in the comparisons, using the fundamental measurements for guidance.

- Resulting computer codes or supporting subroutines must be verified by successful comparison to benchmark measurements at conditions corresponding to the ranges of parameters in the applications.

3. FLOW IN A MODEL SNF PASSIVATION CANISTER

Experimental Setup

Figure 3 from the previous section is a schematic drawing of the generic SNF passivation canister synthesized from various existing designs and passivation geometries. The purpose of this canister is to passivate up to four SNF elements. The SNF elements are placed in the main chamber supported by a porous support plate positioned approximately 2 inlet pipe diameters above the bottom of the canister. The SNF elements are spaced 90° apart on the support plate and 5 inches from the centerline of the canister. This design provides for both the drying and passivation of SNF elements.

One strategy to passivate the fuel rods is to inject a gas of 98% helium and 2% oxygen into the canister via the inlet pipe at a Reynolds number of about 2,500. This gas would then exit the inlet pipe at the bottom of the porous support plate and impinge on the bottom plate of the canister. The passivation gas would then spread within the inlet plenum and eventually flow through the porous support plate and into the main chamber. Once the passivation gas enters the main chamber it would flow along the SNF elements and passivate any corroded areas.

Flow visualization experiments were conducted with a ¼-scale model of this generic design. Figure 4 is a schematic drawing of the model SNF canister with model SNF elements used for this research.

The model canister, inlet tubes and exhaust tube were constructed from clear acrylic. The model canister was divided into two sections: a lower section consisting of the cylinder below the porous support plate, and an upper section consisting of the cylinder above the porous support plate. The porous support plate was constructed from a disk of 1/8” thick white PVC plastic. This plate was drilled in the center with a 3/8” hole for the inlet tube and with a square matrix of 1/16” holes spaced

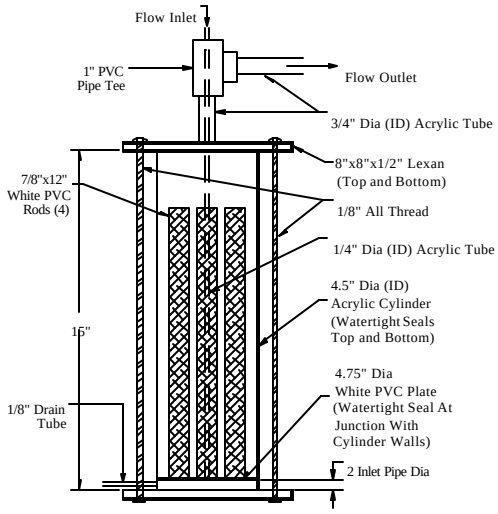

Figure 4. Schematic drawing of a model generic SNF passivation canister.

¼” apart to achieve approximately 4% porosity. The model elements were made from solid white PVC

plastic cylinders and the top and bottom plates were made of clear Lexan®. A metal soda pop dispensing cylinder was modified to perform as a pressure vessel. The pressure vessel was fitted with Swagelok® tube fittings and connected to a compressed air supply with metal tubing.

The pressure vessel air supply was routed through a precision control valve and to a vent also fitted with a control valve. The pressure vessel was connected to a Heise 15-psi pressure gauge. Water was pumped by a Masterflex® Console Drive pump with Easy-Load® pump head via neoprene tubing from the water supply to the pressure vessel and then to the inlet tube on the top of the model cylinder. A Swagelok® reducing union tee was inserted at a high point along this tube in which a hypodermic needle was inserted for dye injection. The inlet/exhaust valve was made from a 1" PVC pipe tee. The inlet pipe was secured in the valve (tee) with a 1/4" Swageloc® tube fitting and a PVC pipe plug. The exhaust tube was glued into the pipe tee with acrylic cement. A 4 ½" Parker O-Ring Seal was compressed into a groove cut into both the top and bottom Lexan plate and a similar seal was compressed between the upper and lower cylinders to hold the porous support plate in position and provide watertight operation. The entire apparatus was secured with 1/8" all thread bolts. Finally, a small 1/4" acrylic tube was attached to the bottom of the cylinder (lower section) to purge air bubbles and to provide a drain. The inlet tube was connected to the pressure vessel by ¼" ID neoprene tubing and Swagelok® tube fittings. A 1" neoprene tube was used to extend the exhaust tube to a drain.

Figure 5 is a photograph of the experimental apparatus. In a typical experiment, water is piped from the building water supply into an open supply tank (not shown in picture but located just to the left of the pumps). The open supply tank allows the water to reach thermal equilibrium with the laboratory environment and allows the air bubbles normally entrained in the supply water to escape through the free surface. This water is then pumped from the supply tank via neoprene

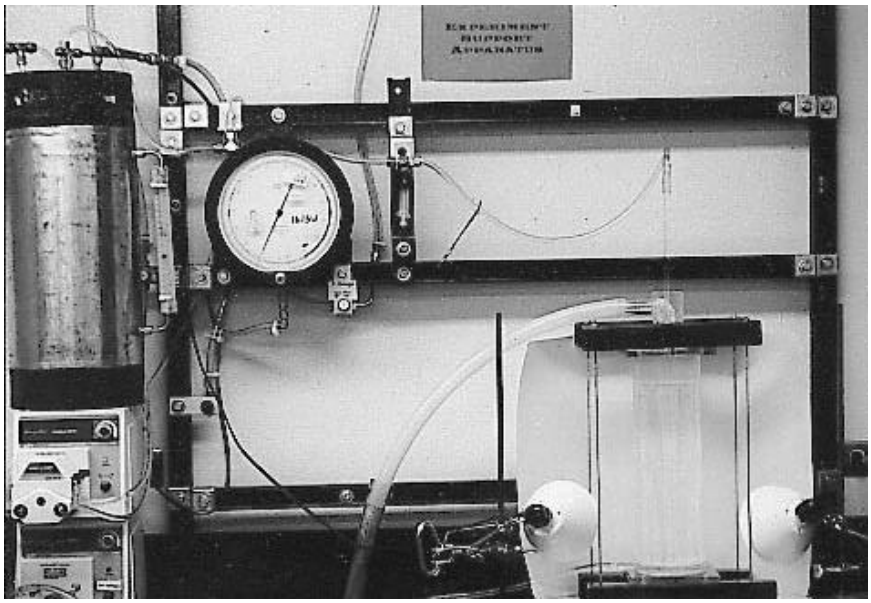

Figure 5. Photograph of the SNF canister flow visualization apparatus.

tubing and a console drive pump to the pressure vessel. The pressure vessel was fitted with a clear plastic tube that provided a visual indication of the water level and pressurized with compressed air

to maintain the water level at a constant level. The air pressure pushes the water out of the pressure vessel via an outlet tube that extends nearly to the bottom of the pressure vessel. The water then flows through neoprene tubing to the model canister flow inlet, through the model canister and through the flow outlet. Water from the flow outlet is piped directly to a drain and discarded.

The volume flow rate of water into the canister is controlled by varying the flow rate (rpm) of the water supply pump and the air pressure in the pressure vessel. The flow rate establishes the amount of water flowing into the pressure vessel and the air pressure maintained in the pressure vessel keeps the water level inside the pressure vessel at a constant level and dampens out pressure pulses caused by the pump head. Thus, the flow rate out of the pressure vessel and into the model canister can be maintained at a constant, steady state value. With standard viscosity and density information, the flow rate established by the pump and pressure vessel, and the dimensions of the inlet pipe (inside diameter), the Reynolds number of the inlet flow is calculated. Additionally, by using air pressure to maintain the water level inside the pressure vessel at a constant level, only the pressure indicated on the pressure gauge could be used to establish the inlet flow Reynolds number. With this system, inlet tube Reynolds numbers from less than 100 to approximately 12,500 were attainable.

Air bubbles inside the model cylinder presented a major problem in these experiments. Air bubbles would frequently attach to the cylinder walls and accumulate under the porous support plate. This problem was reduced by flushing the cylinder with a solution of soap and water before each experiment and by slowly injecting the initial charge of water into the cylinder while it was tilted at a steep angle and oriented so that the drain tube was on top. The soapy water appeared to coat the inside walls of the cylinder with a thin film that prevented air bubbles from adhering to the inside of the cylinder. Also, the slow initial water charge allowed the air bubbles that accumulated under the porous support plate to escape through the drain tube.

Experimental Procedures

For each experiment the model canister was cleaned and flushed with soapy water to prevent the buildup of air bubbles inside the canister. The apparatus was then thoroughly rinsed to remove all soap and soap residue and slowly charged with water from the pressure vessel. Colored poster board was placed behind the apparatus and 65W flood lamps provided indirect lighting. Once the flow was established at the prescribed flow rate (Reynolds number), 1-2 ml of blue propylene glycol dye (food coloring) was injected into the water stream well upstream of the inlet tube. The dye was observed as it flowed through the inlet tube, impinged on the bottom plate, flowed through the porous support plate and, finally, circulated through the main chamber and into the flow outlet tubing. A 35mm SLR camera with motor drive and a CCD color video camera were used to record pictures of the flow.

Experimental Results

Figure 6 is a sequence of six photographs that describe the flow from the inlet pipe into the main chamber of the model canister. The photographs were taken from a position directly in front of the canister and slightly above the plane of the porous support plate. The first picture in the sequence shows flow in the inlet pipe as it approaches the inlet plenum. The characteristic parabolic shape of the boundary layer inside the inlet pipe is distinguishable and establishes that this flow is fully developed. The next shot shows the flow just after it enters the inlet plenum and

begins to impinge on the bottom plate. This photograph describes how the inlet flow impacts on the bottom plate and begins to flow radially along the bottom of the canister toward the outer walls. Continuing on in the next picture, the flow spreads throughout the inlet plenum and begins to develop counter rotational vortices characteristic of confined, submerged impinging jets on a flat, semi-infinite plate (Fitzgerald and Garimella, 1988).

At this point in the injection process, the flow is just about to pass through the porous support plate and enter the main chamber of the canister. Because of the perforated plate, this geometry has been

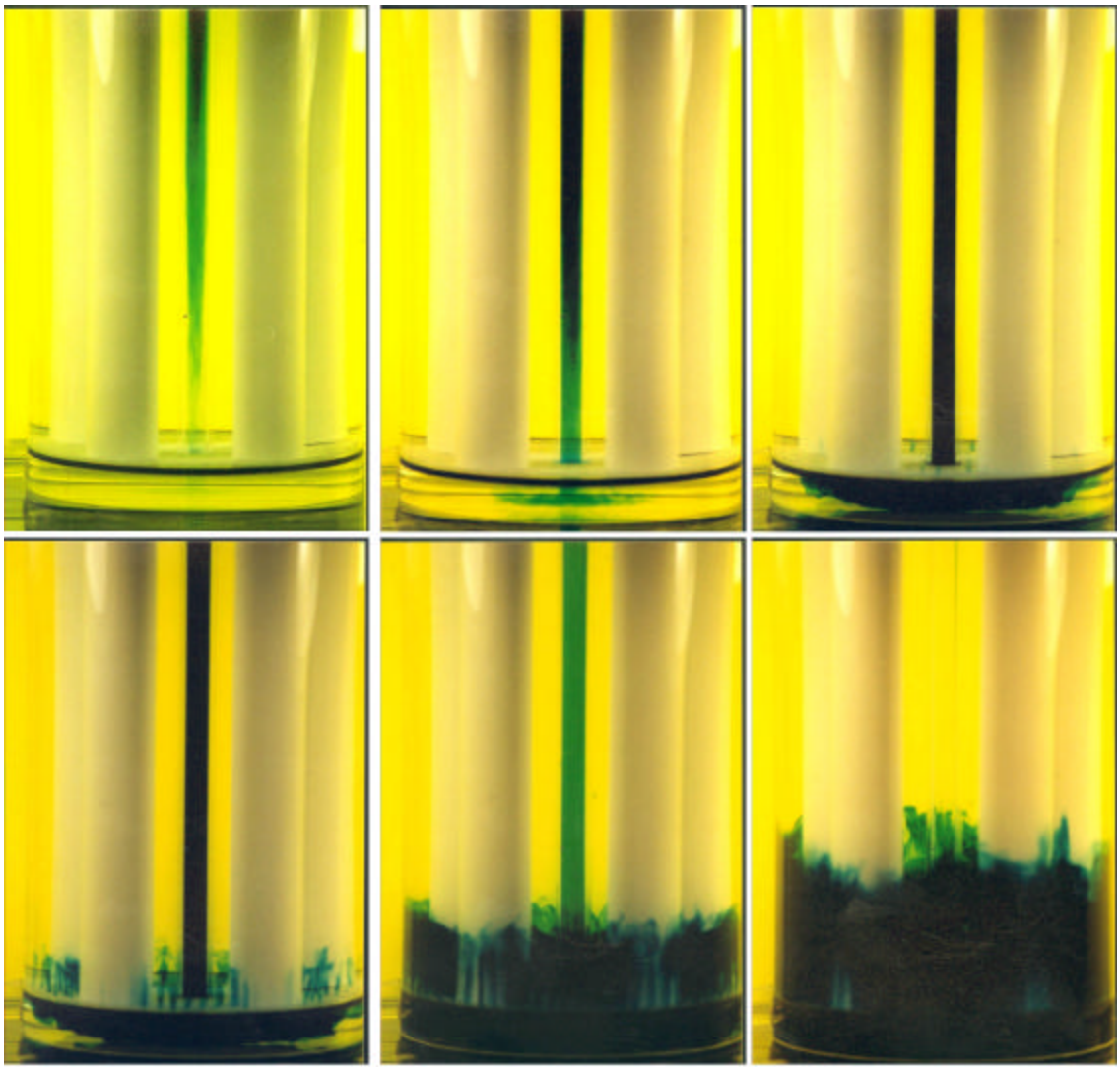

Figure 6. Flow visualization of semi-confined impinging jet, and subsequent flow through perforated plate and into main treatment chamber. Pictures are take at a rate of three frames per second.

called a semi-confined, submerged impinging jet.

The picture on the bottom left shows the flow as it just begins to flow through the porous support plate. Note that the flow that emerges above the porous support plate is non-uniform and unevenly distributed. The next picture in sequence shows the flow as it continues to pass into the main chamber and confirms the uneven, non-uniform nature of the initial flow into the main chamber. The final picture shows the flow in the main chamber several seconds after passing through the perforated support plate. As this flow continues into the main chamber the flow velocity is dramatically reduced because of the much larger volume in the main chamber. Viscous effects begin to dominate this stage of the flow causing the flow instabilities observed earlier to dampen out, allowing the flow to relaminarize as it moves upward. The relaminarization phenomena at this point in the flow is important because this establishes that the flow in the main chamber can be modeled in the laminar flow regime.

Figure 7 is a series of photographs showing the flow as it emerges through the porous support plate at an inlet pipe Reynolds number of approximately 2500. The photographs were taken from a position directly above the model canister and are looking down through clear water toward the bottom of the main chamber. The white PVC plastic porous support plate with the square matrix of holes can be seen on the bottom of the canister. The narrow inlet tube is visible in the center and the two somewhat larger model SNF elements are visible just to the left and right of center.

The first figure in the sequence shows the flow after it has entered the inlet plenum and just before it begins to pass through the perforated support plate. The next picture shows the flow as it begins passing through the porous support plate. This photograph clearly shows how the flow first emerges in the area between the model SNF elements at a distance of about 70% of the canister radius. The following picture shows the flow as it continues to pass through the porous support plate in the area between the model SNF elements and also begins to flow through the other areas of the porous support plate. Fluid can be observed emerging in the area inboard of the model SNF elements as well as in the area radially outboard of the model SNF elements. Close inspection of the flow plumes arising from the porous support plate give the first indication of flow non-uniformities in this section of the model canister. The last three pictures describe how the flow into the main chamber continues to be dominated by flow in the area between the model SNF elements and the continuing uneven, non-uniform flow that develops in this lower section of the canister.

Figure 8 is a sequence of photographs showing the inlet flow as it emerges through the porous support plate at various Reynolds numbers. The photographs were taken from a position directly above the model canister and are again looking down through clear water toward the bottom of the main chamber. In these photographs a portion of the white PVC porous plate with its square matrix of holes is visible on the bottom of the main chamber with the model SNF elements appear as large, dark, circular shadows at left center. The larger, dark shadow at right center is the inlet/exhaust valve at the top of the model canister. These shadows are due to the camera position. For these photographs, the camera was mounted almost directly above the model SNF elements and therefore the large valve located on the top of the canister obscured a portion of the main chamber.

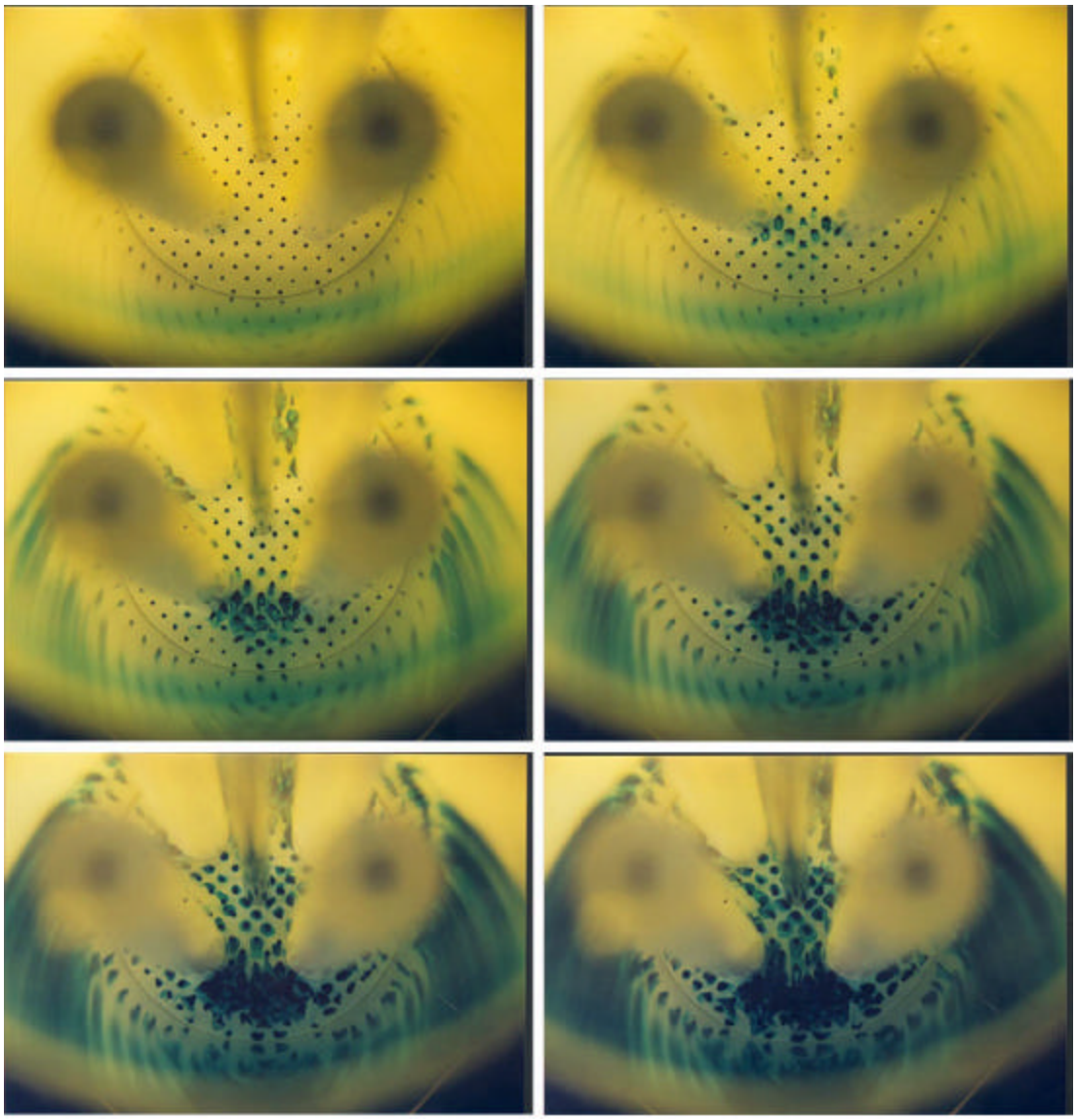

Figure 7. Top view of flow through the perforated plate at a inlet Reynolds number of Re = 2500. Pictures are take at a rate of three frames per second.

The photographs clearly describe the inlet flow as it emerges through the holes in the porous support plate. Note that at low Reynolds number (Re = 2500) the flow emerges from the porous support plate in an area generally between the model SNF elements and at a distance of about 70% of the radius from the center of the plate exactly like that observed in Figure 5. The remaining photographs describe how the area where the flow first emerges from the porous support plate moves radially outward as the Reynolds number increases.

The phenomenon described in this series of photographs is important because of its relationship to the overall mission of SNF passivation. Observations indicate that introducing flows into the plenum chamber at higher inlet Reynolds numbers introduces additional instabilities into the lower region of the main canister and increases the tendency for non-uniform flow in the main chamber.

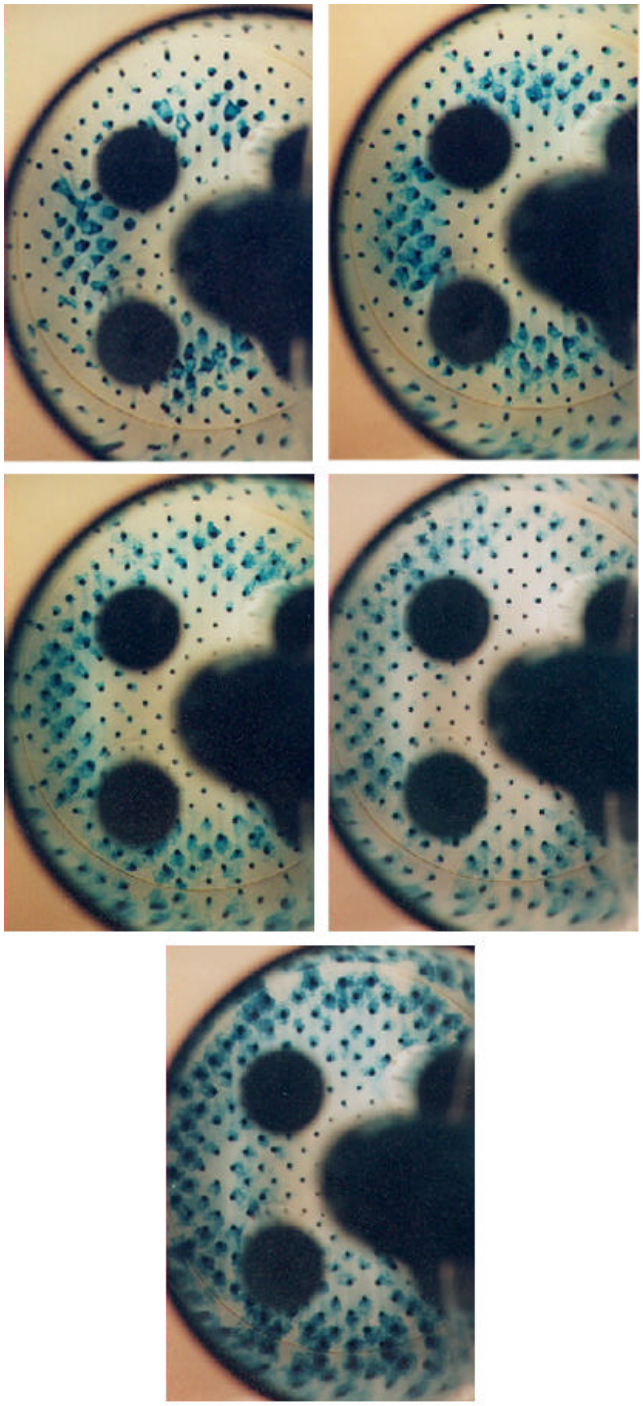

Figure 8. Flow as it begins to pass through the perforated plate at various Reynolds numbers. The flow in the upper left hand corner is at Re = 2500, and in sequence, the Reynolds numbers are at 5000, 7500, 10,000, and 12,500 respectively.

Flow into a model SNF passivation canister exits the inlet pipe at the porous support plate, impinges on the bottom plate of the canister and flows radially outward, being roughly uniform about the centerline. Two counter rotating, torodial vortices form in the inlet plenum: one at a distance of about 70% of the radius, the second near the outside wall. The inner vortex causes non-uniform and uneven flow to be pushed through the porous support plate at a distance of about 70% of the radius of the canister, generally in the area between the model SNF elements. Several non-uniform, slow, upward moving vortices develop in the main chamber just above the porous support plate. As this non-uniform, uneven flow continues to migrate upward into the main chamber, the change in volume slows the flow where viscous effects begin to dominate and many of the flow instabilities are dampened out. Flow along the model SNF elements appears to relaminarize and flow evenly toward the exhaust tube. Higher Reynolds number flow introduces additional instabilities in the inlet flow and could cause the flow in the main chamber to remain unstable and non-uniform for a longer time as it migrates upward into the main chamber before being dampened out by viscous effects. The relaminarization of flow in the main chamber by lower Reynolds number inlet flows establishes that the surface reaction phenomena that occurs on a cylindrical surface in a SNF passivation canister can be adequately modeled and examined using a flat plate in the laminar flow regime. Additional results and description can be found in McIlroy [2000].

4. FLOW OVER A FLAT PLATE WITH A SURFACE REACTION

Experimental Setup

Figure 9 is a schematic drawing of the surface reaction flow apparatus which was designed and built to support this research.

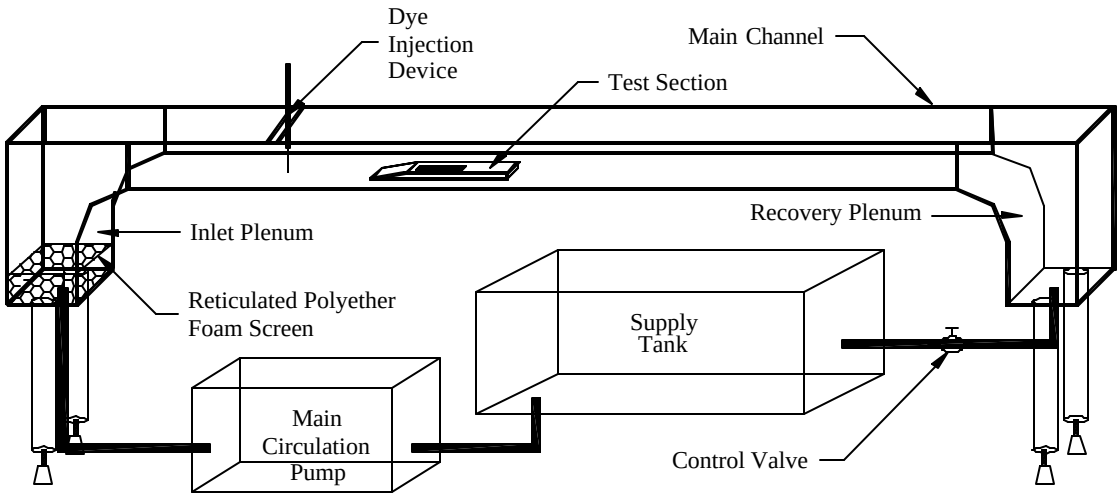

Figure 9. Schematic Drawing of Surface Reaction Flow Apparatus

The inlet plenum, main channel, recovery plenum and dye injection device were constructed from clear ½" acrylic and joined together with Weld-On No. 4 Clear, Water Thin, Moderately Fast Curing Solvent Cement. These main components were mounted on legs made of 1" acrylic rods and fitted with adjustable feet so that the apparatus could be leveled. The lower section of the inlet plenum was packed tightly with Reticulated Polyether Foam. A 21-liter acrylic container was used as the supply tank. A 7 gallon per minute (gpm) variable speed, centrifugal drive micropump was used as the main circulation pump. The main apparatus was connected to the supply tank by 1" stainless steel piping and ½" neoprene tubing with Swagelok® fittings and Masterflex® tubing connectors. A large lever-action ball valve controlled flow to the supply tank in the 1" stainless steel piping and a smaller lever action ball valve controlled flow to the supply tank in the neoprene tubing. The pump was connected to the supply tank and inlet plenum by ½" neoprene tubing, Swagelok® fittings and Masterflex® tubing connectors. The dye injection device consisted of a bridge, injector support, connection tubing and injector. The bridge was constructed of 1" clear acrylic. The injector support was constructed of ½" and 1/8" clear acrylic and the connection tubing was constructed from a ¼" (OD) rigid acrylic tube. The injector was constructed from a 2" long 0.0512" diameter metal tube drilled along the centerline with 8 holes 0.0135" in diameter (No.80 drill) approximately 0.2" apart. The bottom (end) of the injector tube below the lowest injection hole was sealed with liquid metal. The injector was joined to the connection tube by an 18-gauge veterinary needle base. The connection tube was connected to the dye supply with ¼" (ID) clear No. 16 Tygon® Tubing. A 0-100 rpm Masterflex® L/S variable speed console drive

pump with Easyload® roller pump head was used as the dye injection pump. A GraLab Model 451 Electronic Timer/Intervalometer was used to pulse the dye injection pump thus ensuring a small, accurate and consistent volume of dye was injected into the main solution flow. The test section was a 3” x 6” x ¼” aluminum plate. The plate was tapered to a point on the leading edge and a ½” x 2” x 1/8” cavity was machined along the long axis of the plate, centered along both the length and width of the plate. The test section cavity was filled with pure sodium metal by pressing a small amount of sodium into the cavity and then trimming the sodium so that it was even with the top of the plate and smooth. The test section with embedded sodium is stored in mineral oil between experiments for safety.

The flow solution consisted of a mixture by volume of 80% mineral oil and 20% hexanoic acid. Hexanoic acid ($C_5H_{11}COOH$) is soluble in mineral oil and reacts well with sodium. As the solution of mineral oil and hexanoic acid flow over the sodium in the test section, the acid in the flow solution reacts with the sodium in the test section. This reaction produces a hexanoic salt ($C_5H_{11}COONa$) on the surface of the sodium and releases hydrogen bubbles into the flow. The chemical equation for this reaction is,

$$C_5H_{11}COOH + Na \rightarrow C_5H_{11}COONa + \tfrac{1}{2} H_2$$

The injection fluid consisted of a similar mixture by volume of mineral oil, hexanoic acid and Sudan Black B high purity biological stain. The density of the injection fluid was carefully matched to the density of the main flow solution by adding the necessary volume of hexanoic acid to 150 milliliters of mineral oil and 1 gram of biological stain. The density of this solution was compared to the density of the main flow solution by placing a drop of injection fluid in a graduated cylinder filled with main flow solution. The density of the injection fluid was adjusted until the drop of injection fluid was neutrally buoyant in the flow solution.

The test section was prepared by hand-pressing a thin slab of metallic sodium into the cavity in the aluminum plate. Sodium metal is quite soft so this was accomplished with little effort. However, because sodium is so soft, it often proved difficult to trim the excess metal even with the surface of the aluminum plate. Every attempt to trim the entire slab of sodium with one continuous cut resulted in the slab being pulled out of the cavity. The problem was minimized by using very sharp razor blades and only trimming a small a section of the excess sodium at a time.

In a typical experiment, a solution of mineral oil and acid is thoroughly mixed and placed in the supply tank. The main circulation pump then pumps the solution from the supply tank into the inlet plenum. The solution flows through the polyether foam screen where flow irregularities are dampened out and into the main flow channel. The solution then flows into the recovery plenum where it is drained into the recovery piping/tubing and back into the supply tank. The liquid level and velocity of flow in the main channel is controlled by the speed of the main circulation pump and the two lever-action ball valves that control flow from the recovery plenum into the supply tank. When this flow is stabilized at a constant pump speed and flow level in the main flow channel the test section is placed in the main channel and the dye injection device positioned upstream of the test section. Dye is injected into the main flow and the effects of the surface reaction on the filaments of the dye are observed and recorded. Once the dye passes the test section it is vacuumed from the flow to prevent contamination of the main flow solution which was recycled. Failure to remove this dye would result in a very dark flow solution at some point and

make observation and photography very difficult and require changing the working fluid often (periodically).

Experimental Procedures

Because the Reynolds number of the flow in the main chamber of the idealized SNF Passivation Canister is approximately 350, all experiments were conducted with similar a Reynolds number in order to match the flow characteristics of the experiment and actual flow in the canister. Because flow at Reynolds number 350 proved to be somewhat fast in some applications, experiments were also conducted with Reynolds numbers of approximately 100 and 160. When the solution in the main channel is at the desired velocity and at the correct level, the test section is placed in the main channel with the centerline of the test section aligned with the centerline of the main channel. After a few minutes the sodium in the test section begins to react with the hexanoic acid in the flow solution. The slight delay before the acid and sodium begin to react is due to an oxide layer that forms on the sodium during storage.

When this reaction was well established, the dye injection device was mounted on the sidewalls of the main channel. The injector was positioned in the center of the main channel and the spring-loading mechanism was adjusted to provide a slight downward pressure of the injector on the bottom of the main channel. The timer/intervalometer was programmed with the appropriate on/off timing for the dye injection pump and the dye injection pump was set for the desired speed. With this system, when the timer/intervalometer was energized, it provided a pulse of electrical power to the dye injection pump for a specific period of time. When the dye injection pump was energized by the timer/intervalometer, the pump then operates at the preset speed (rpm) pumping a small, specific volume of dye into the dye injection device. When the necessary photographic equipment was in place, the timer/intervalometer was energized, dye was injected into the main flow solution and the effect of the surface reaction was photographed as the dye filaments passed over the test section.

Safety Procedures

Because hexanoic acid is a strong corrosive and sodium is a very dangerous metal, safety was a priority during the experiments. Material Safety Data Sheets were obtained and posted at various locations in the lab. Sodium metal (received in ingot form) was maintained in a mineral oil bath and stowed in a fume hood. The aluminum test sections that had sodium pressed into the test cavity were also stowed in a mineral oil bath. During periods when the apparatus was idle and no experiments were being performed the entire apparatus was covered and plainly marked with a hazard/danger sign. Also, before experiments were conducted, proper operation of the building's ventilation system was confirmed and hazard signs were posted in the laboratory. Additionally, adequate supplies of personal protective equipment such as rubber gloves, safety goggles, lab coats and aprons were maintained in the lab.

Experimental Results

Figure 10 is a sequence of twelve side view photographs that describe the flow of a solution of 80% mineral oil and 20% hexanoic acid at a Reynolds number of approximately 350 as it passes over the test section where a surface reaction takes place. The photographs were taken with a Nikon D-1 digital SLR camera with a 28-70 mm zoom lens and Nikon Capture software. The

camera was positioned on the side of the main channel, perpendicular to the main flow on a plane roughly level with the center of the flow solution. Lighting was provided by a Nikon SB-28X Autofocus speedlight equipped with a flash-diffusion lens in a rear-curtain mode and with the laboratory fluorescent lights turned off. The camera was operated in the continuous shutter mode at 2 frames per second (0.5 seconds between photos). The image data format is JPEG (8-bit), the shutter speed was 1/80th second, the aperture opening was f3.2, the sensitivity was ISO 800 and the white balance was on automatic.

The flow is from left to right and approximately 1 ¾" deep. A total of 8 dye filaments are injected into the main flow approximately 6" upstream of the test section. The dye filaments from the dye injector and the hydrogen bubbles resulting from the reaction between hexanoic acid and sodium are clearly visible. Also, note that bubbles are rising from the entire length of sodium metal in the test cavity. The first picture describes the flow as the top six dye filaments approach the rising bubbles from the surface reaction. The six visible dye filaments describe the upper regions of a laminar boundary layer consistent with classical low Reynolds number boundary layer flow. Additionally, note that the dye filaments are level and roughly uniform as they approach the reaction site. Also, note the pronounced hump in the rising bubbles about half way up the bubble stream between the aluminum plate and top of the photograph. The next picture describes the initial interaction between the rising bubbles and the top dye filament. Note that the hump in the rising bubble stream has moved about the same distance downstream as the dye filaments. This indicates that the rising bubbles, which have both horizontal and vertical velocity components, have a horizontal velocity component that is roughly equal to the horizontal component of the dye filaments. Accordingly, the bubbles are being convected downstream at about the same velocity as the dye filaments. Note how the top two dye filaments are turned slightly upward.

In the next row, the pictures describe the continuing interaction between the dye filaments and rising bubbles. Note that the leading edge of the hump of bubbles previously identified is now almost exactly coincident with the leading edge of the top dye filament. The top dye filament has been pushed slightly upward and developed a barely visible curl at the tip that indicates the initial roll-up into a vortex. Also, note that the tips of the top four dye elements have all been imparted with a vertical velocity component before they actually come in contact with the bubble stream. The following picture is the first photograph of direct interaction between the bubbles and dye filaments. In this photograph, the top four dye filaments are clearly being convected upwards and the third from the top dye filament has been pulled into what appears to be a void between two pronounced humps in the rising bubble stream. Also, the top two dye filaments appear to be passing among and between several bubbles in the leading edge of the bubble stream.

The next pictures describe how the top four dye filaments are now fully involved with the bubble stream. These photographs show additional evidence of the interaction between the bubbles and dye streams. The upper right corner of the next picture describes vertical humps in the top two dye filaments, which are actually the initial stages of a vortex rollup on the near side of the bubble stream. On the fourth row, the pictures describe the continuing vortex formation by the top three dye filaments and clearly show the fourth from the top filament curling up and around the third filament. These pictures clearly describe the vortex forming just above the end of the aluminum plate. The rest of the pictures show continuing convection downstream of the curled dye filaments, and the interaction between dye filaments and the bubbles. The figures demonstrate well-developed vortex patterns combined with buoyant bubble convection.

Figure 11 is an enlarged view of the ninth picture in sequence shown in Figure 10, along with an expanded view of the dye and bubble interaction. In the top picture, one notices a distinct periodicity of the bubble humps on the leading edge of the bubbles. This is similar to the billowing effect that one observes on rising smoke plumes in crossflow. We believe this arises due to the Kelvin-Helmholtz instability. This instability occurs when the flat plate boundary layer interacts with the rising, buoyant fluid that is entrained by the bubbles. This interaction causes an inflection point in the velocity profile, which in turn generates an instability [Crepeau and McIlroy, 1999].

The bottom portion of Figure 11 clearly shows the beautiful and complex interaction between the rising bubbles and the dye filaments. Some of the bubbles interact individually with a single dye filament generating a sharp peak, while other bubbles rise as a group, pushing filaments up and deforming en masse.

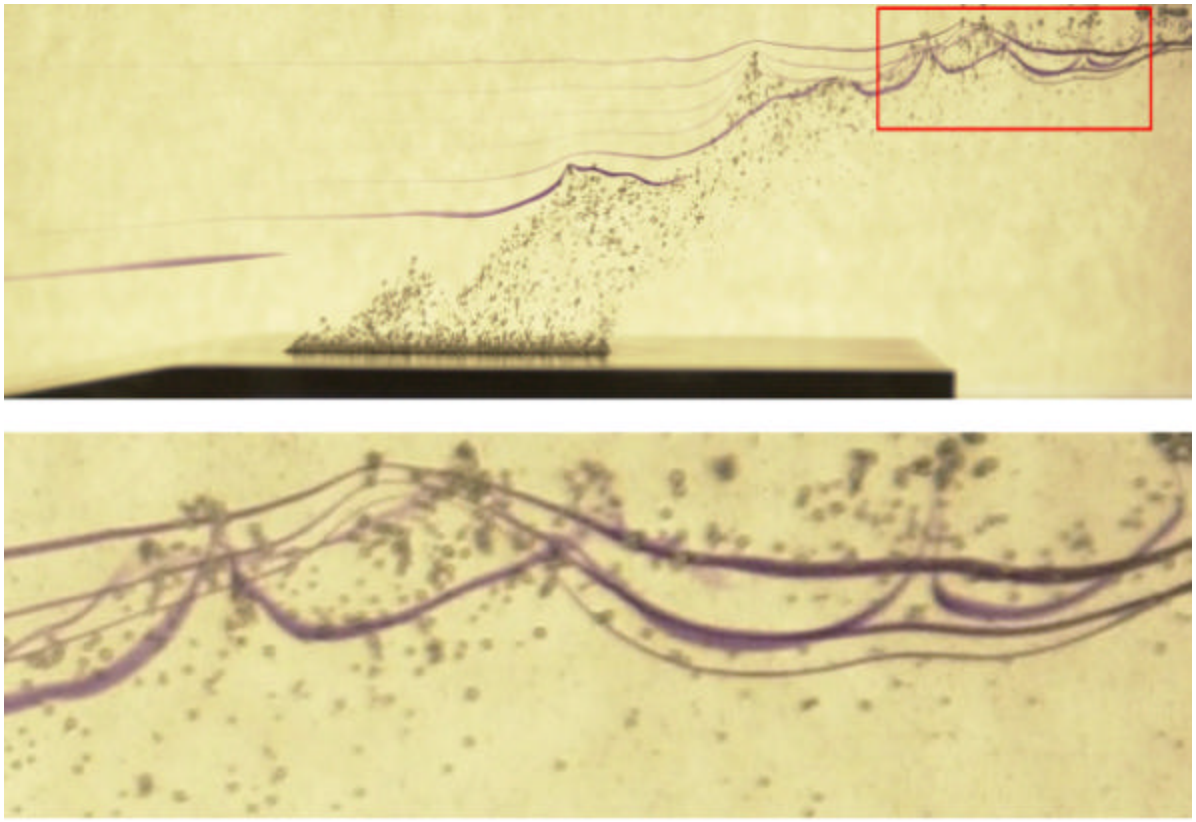

Figure 11. Expanded view of the ninth picture in the sequence shown in Figure 10, and an enlarged view of the dye-bubble interaction.

Figure 10. Side view of the dye bubble interaction at Re = 350. Sequence goes from left-to-right. Note the periodic humps (billowing) of the leading edge of the bubbles, and the complex interaction between the dye and the bubbles farther downstream. Pictures are taken at half-second intervals.

Figure 12 is a sequence of six top-view photographs that describe the same type of flow from a position above the test section. The Reynolds number is approximately 350. The same camera was used for these photos but the lighting was changed. The laboratory fluorescent lights were turned on and two 20-Watt incandescent mini flood lamps were positioned on either side of the main

channel at the test section. A 65-Watt incandescent flood lamp was positioned above and downstream of the test section. The camera settings were the same as in the previous sequence but the shutter speed was set at 1/125th second and the aperture was set at f6.3. Again, the flow is from left to right and the dye filaments and hydrogen bubbles resulting from the reaction between hexanoic acid and sodium are clearly visible.

The first two pictures describe the flow as it approaches the bubbles from the surface reaction. Note that the dye filaments are straight and intersect the test section almost perfectly on the test section centerline. The next picture describes the initial interaction between the dye filaments and rising bubbles. Note that the top dye filament has been pushed to the side of the bubbles and the next dye filament has already begun to interact with the bubbles and is also being pushed to the

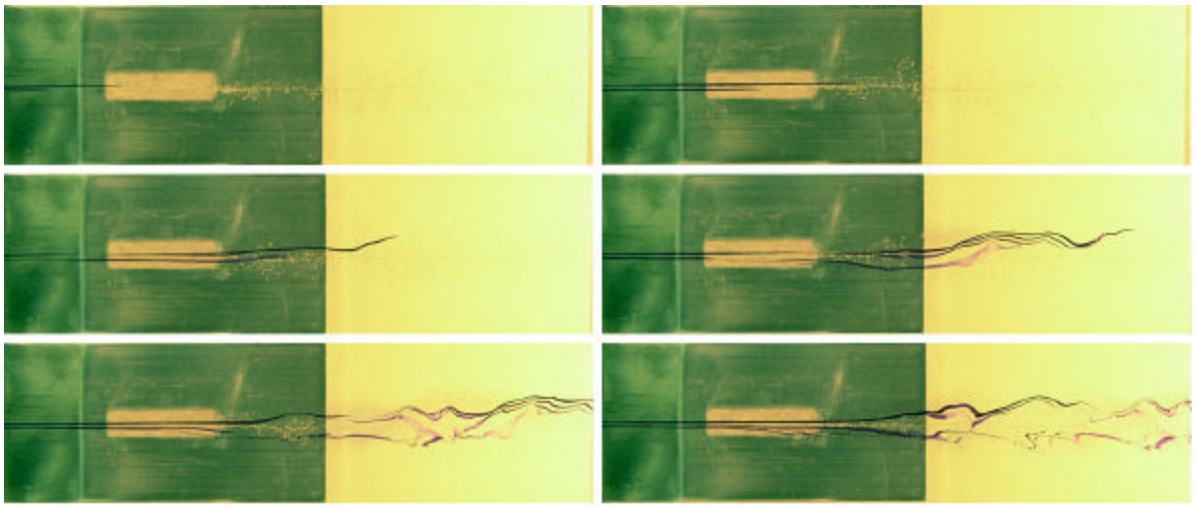

Figure 12. Top view of the dye-bubble interaction at Re = 350. Pictures are taken at two frames per second.

side of the rising bubble stream. This photograph also displays the early stages of the top filament rolling up into a vortex as it is convected downstream. The fourth picture clearly describes the dye filaments being pushed to the sides of the bubble stream downstream of the reaction site. Also, note that the last filament to interact with the bubbles has been broken up and is diffusing into the main stream flow. The last two pictures describe the dye filaments being pushed to both sides of the bubble stream and the continuing downstream interaction between the filaments and bubbles. They clearly show the vortex formations downstream of the reaction site. These downstream vortices stop rotating as they are convected downstream because of viscous dampening.

Figure 13 is a sequence of ten side view photographs that describe the same type of flow at a Reynolds number of approximately 100. Again, the photographs were taken with a Nikon D-1 digital SLR camera with a 28-70 mm zoom lens and Nikon Capture software. The flow is from left to right and approximately 1 ¾" deep. Note that the bubble stream rises at a much steeper angle because the flow is considerably slower than it was for the previous photographs. Also, note that bubbles are rising from the entire length of sodium metal in the test cavity indicating that the entire surface of the sodium is actively involved in a chemical reaction with hexanoic acid from the flow medium.

The first picture in Figure 13 describes the approach of the top six dye filaments to the reaction site. Note that the dye filaments are level and describe the same characteristic shape of a fully developed boundary layer flow observed previously. Also, note that the humps in the rising bubble stream are not as pronounced as they were in the higher Reynolds number flow. The second picture shows the initial interaction between the rising bubbles and the dye filaments. The top two dye filaments are being turned slightly upward before they actually encounter the bubble stream. The second row of pictures describe the top four dye filaments as they appear to begin to be stretched, thinned and convected upward by the bubble stream exactly as what was observed previously. The third row describes the first hint of a curl being formed downstream of the reaction site. Note the rollup formation just below the free surface and about half way between the reaction site and the end of the aluminum plate. The rest of the pictures display similar behavior described in Figure 10. The dye filaments flow level until they encounter an upward velocity component imparted by the rising bubble stream. The filaments are then convected upward toward the free surface and begin to form small vortices as they are pushed outboard and downstream.

Figure 14 is a sequence of twelve top-view photographs that describe the same type of flow from a position above the test section. The flow is from left to right at a Reynolds number of approximately 100. The photographs look down at the dye filaments at a slight angle to the left of vertical (as one looks upstream toward the dye injection device) because the camera was offset slightly in order to observe the lower dye filaments as they approached the reaction site.

The first row of pictures shown in Figure 14 describes the initial approach of the dye filaments to the rising bubble stream. Note that the dye filaments are straight and echeloned upstream which again describes the characteristic boundary layer of low Reynolds number flow over a flat plate. The second pictures in the first row describes the top filament as it is just beginning to be turned by the bubble stream near the free surface.

The second row shows the top dye filament as it is fully involved with the bubbles as they spread out laterally to both sides of the flow at or near the surface. Also, note that the second dye filament from the top has traveled some distance into the region of the surface reaction and not yet encountered the rising bubble stream. The pictures show the initial rollup of the 2nd from the top dye filament as it is pushed up and to the left of the bubble stream and the 3rd from the top dye filament as it is being pushed to the right of the bubble stream. The pictures describe a fully developed vortex curl on the left side of the bubble stream being convected downstream and the 3rd and 4th from the top dye filaments being turned to the right and pushed upward toward the surface. Note that the 2nd from the top dye filament has been redirected back toward the right side of the bubble stream and diffused by interaction with bubbles. These photographs clearly describe the formation of vortices on both sides of the flow. The remaining pictures in the sequence describe the

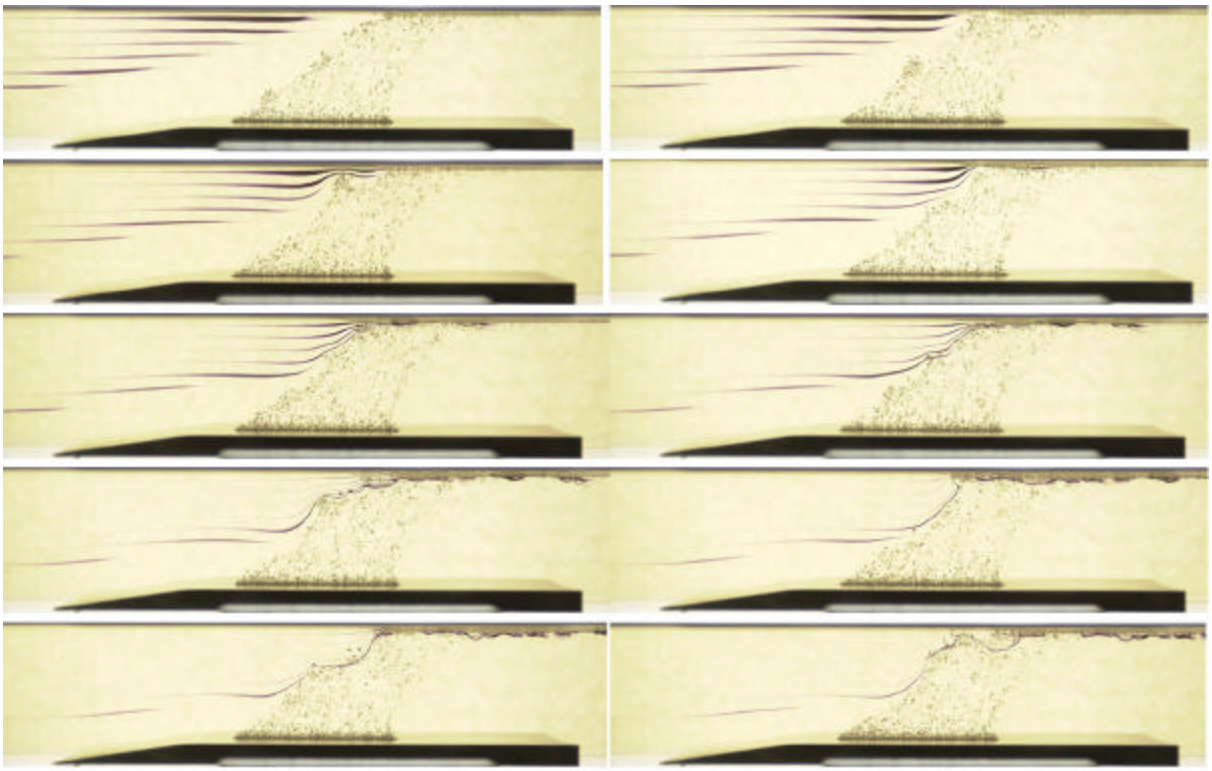

Figure 13. Side view of dye-bubble interactions at Re = 100. Pictures are taken at half-second intervals, and proceed from left to right in sequence.

dye filaments on both sides of the flow stream being convected downstream without dramatic changes. This indicates that the vortices developed on either side of the rising bubble stream stop rotating as they are convected downstream and the instabilities encountered earlier die out due to viscous dampening.

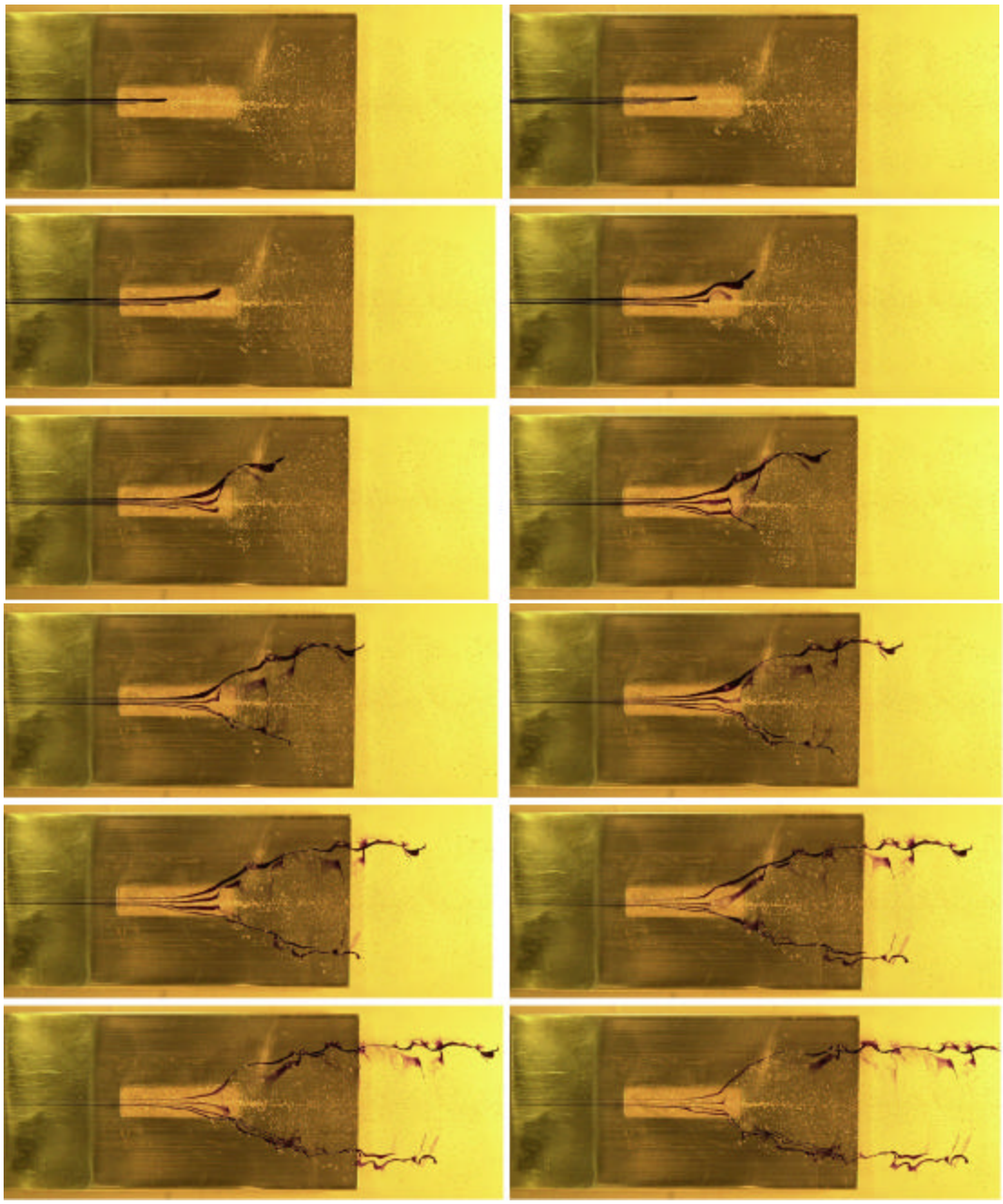

Figure 14. Top view of the dye-bubble interaction at Re = 100. Pictures are taken every half-second. Note the formation of vortices that form downstream of the reaction site.

Figure 15 is a sequence of ten end-view photographs that describe the same type of flow at a Reynolds number of approximately 100. These photographs were taken downstream of the reaction as the flow approaches the observer. The camera was positioned at the end of the main channel, parallel to and coincident with the long axis of the main flow channel on a plane roughly level with the center of the flow solution. Lighting was provided by two 20-Watt incandescent

mini-flood lamps on each side of the main channel, a 65-Watt incandescent flood lamp shining indirectly on the inlet end of the main channel, and a 65-Watt incandescent flood lamp shining on the test section from a position downstream from and above the test section. The laboratory fluorescent lights were on. The camera was operated in the continuous shutter mode at 2 frames per second. The image data format was black and white TIFF-RGB (8-bit), the shutter speed was 1/80th second, the aperture opening was f3.2, the sensitivity was ISO 1600 and the white balance was on automatic. The flow is approximately 1 ¾" deep and a total of 8 dye filaments are nearly simultaneously injected into the main flow approximately 6" upstream of the test section. Again, note that the entire width of the cavity embedded with sodium metal is covered with hydrogen bubbles. This establishes that the entire slab of sodium is reacting with hexanoic acid from the flow medium.

The initial picture in Figure 15 describes the dye filaments as they encounter the rising bubble stream and are being convected upward and outboard of the reaction site. The next shows the dye filaments as they are carried outboard by the bubble stream and the initial evidence of the vortex rollup on the tip of the 2nd from the top dye filament. The second row of pictures describes the top dye filament being rolled under the 2nd from the top dye filament as it continues to be convected upward, outboard and downstream. The rest of the pictures clearly show the vortex (curling) action imparted to the dye filaments by the rising bubble stream, then stabilizing and losing their rotating action after viscous dampening.

Figure 16 is a sequence of twelve top view photographs describing off-center flow from a position above the test section. The flow is from left to right and at a Reynolds number of approximately 160. The dye injections for these photographs were injected about 5/16" off center in order to observe the affect of the rising bubble stream on the flow on either side of the reaction site.

The first three pictures in the sequence given in Figure 16 describe the flow as it approaches the test section, then turn outboard. Note that the dye filaments are straight and pass to the right of the embedded sodium. Note that the top dye filament has been turned further than the dye filament directly underneath. The next three pictures also describe the turning action imparted to the top dye filaments by the bubble stream. Again, the top dye filament has been pushed further outboard than the lower dye filaments. The rest of the pictures in the sequence describe the outboard motion imparted to the upper dye filaments and that downstream of the reaction site, these dye filaments are convected downstream without significant change to their orientation.

Figure 17 is an enlarged view of the last picture in Figure 16, and it describes how the lowest dye filament turns toward the reaction site. This phenomena is due to the counterrotating vortices formed on both sides of the rising stream of bubbles and the fluid transports the reacting fluid downstream of the reaction site. This phenomenon is interesting because it gives some insight into how the reaction over the entire length of the test section is able to continue.

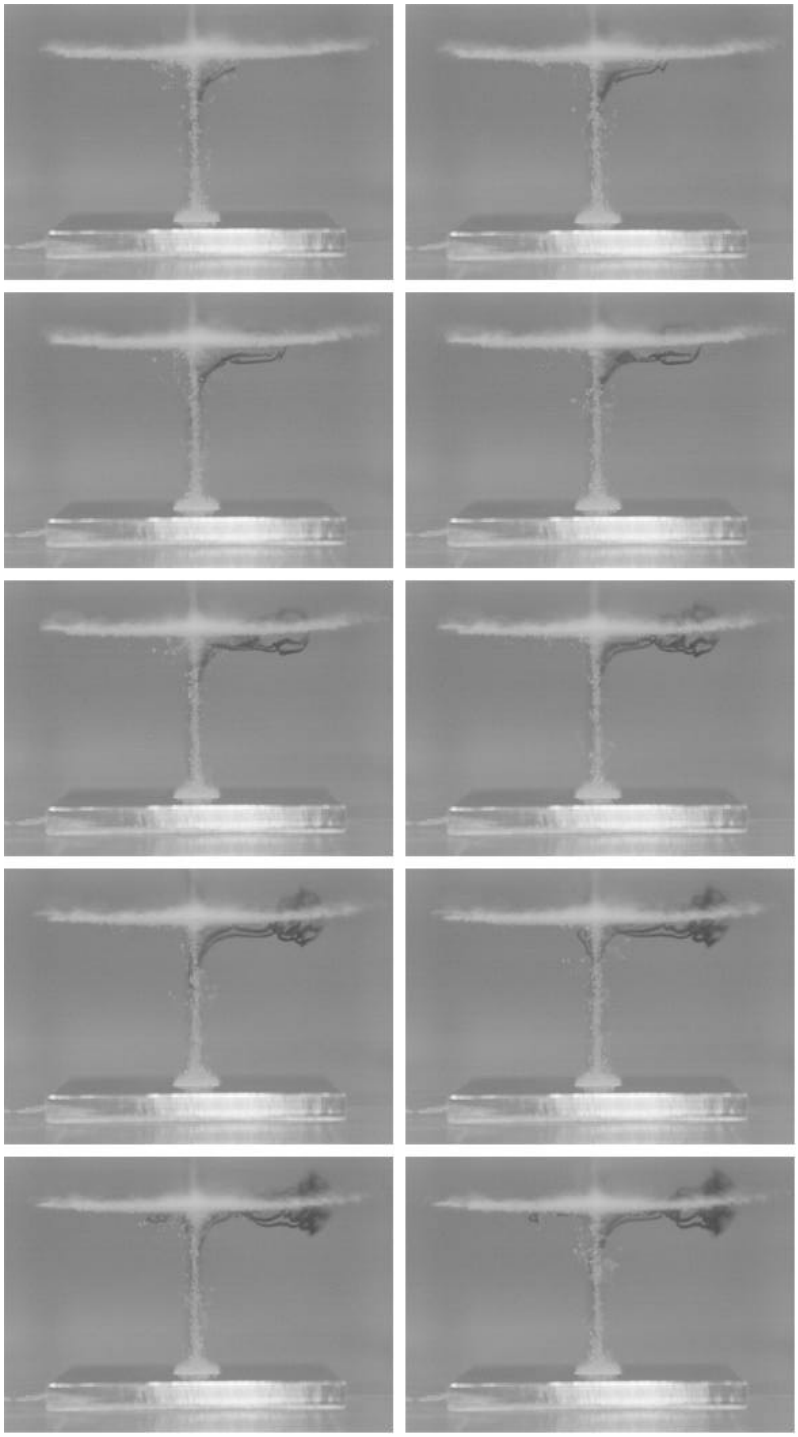

Figure 15. End view of the dye-bubble interaction taken at two frames per second. The Reynolds number is Re = 100.

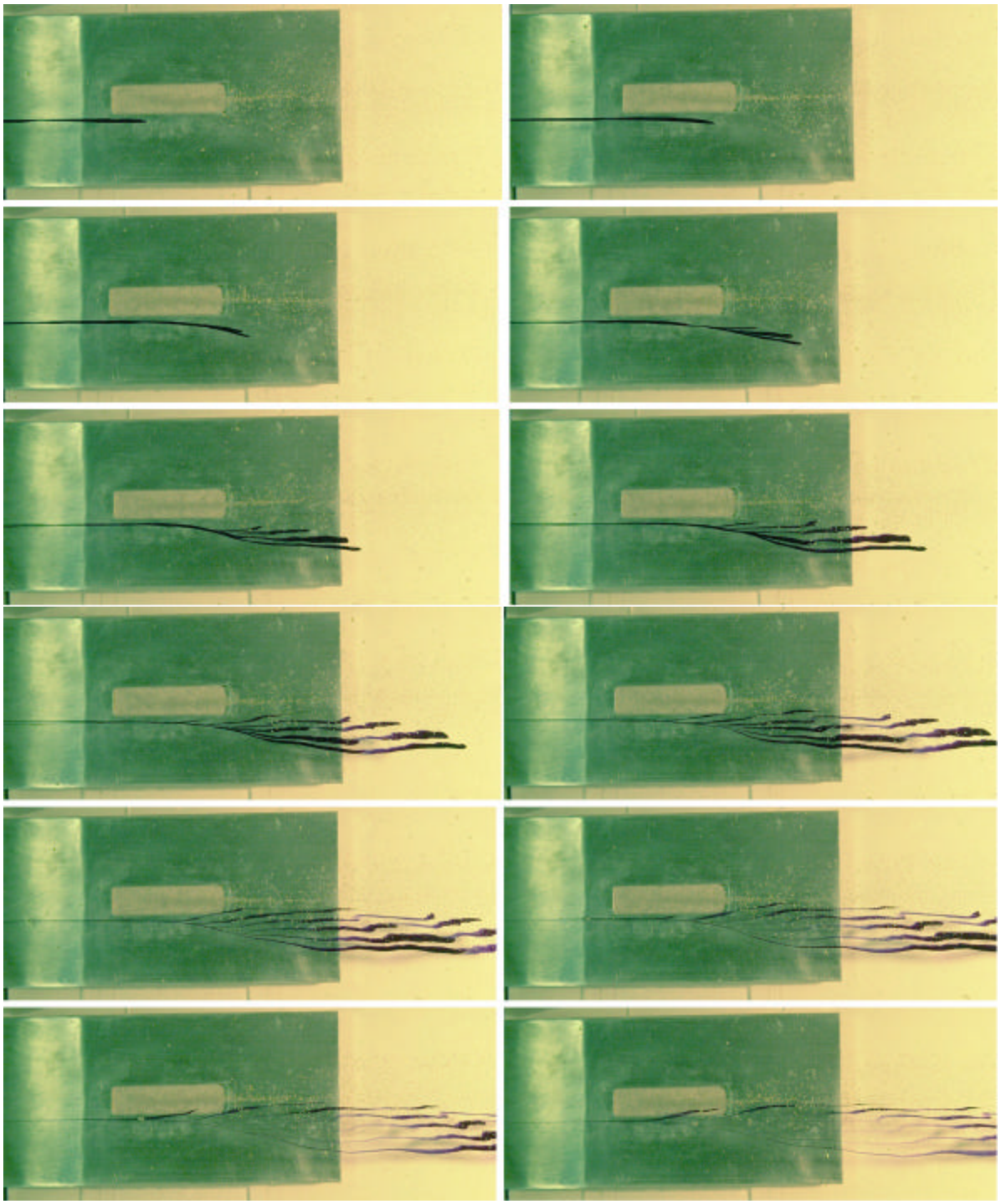

Figure 16. Top view of the off-center dye injection at Re = 160. The flow visualization clearly shows the formation of counterrotating vortices caused by the rising bubbles. The last pictures show that the fluid near the plate is convected toward the reaction site by the vortices.

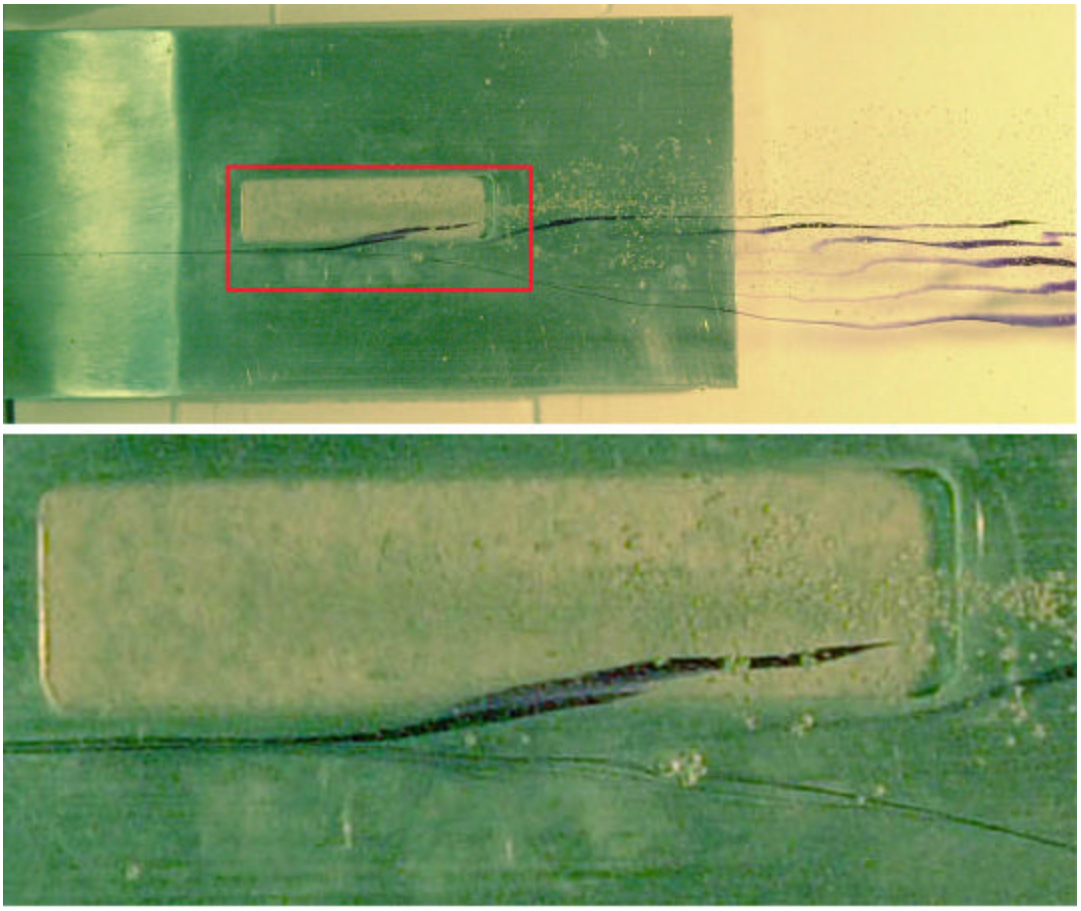

Figure 17. Expanded view of the last picture shown in Figure 16. Note that the dye filaments are being convected into the downstream portion of the reaction site by the counter-rotating vortices created by the rising bubbles.

The chemical reaction on the surface of the test section produces hydrogen bubbles that rise to the surface due to buoyancy forces. The bubbles develop a vertical, upward velocity. Bernoulli's principle establishes that the inside of the bubble stream develops a slightly lower pressure than the free stream flow on either side of the bubble stream. The higher pressure on the sides of the bubble stream push the bubble stream inboard forming a thin stream of bubbles rising to the surface. The main flow streamlines upstream of the area of the reaction site are stable, straight and level. As these streamlines approach the rising hydrogen bubbles they encounter the vertical flow of the rising bubble stream and are turned upward and compressed toward the free surface.

When the bubbles reach the free surface they are slowed by the free surface boundary layer and pushed outboard toward the sides of the main flow channel by continuity considerations. As the main flow streamlines encounter the slower and spreading bubbles near the surface, they are in turn slowed and pushed outboard as they are also being convected downstream. The main flow streamlines cannot continue to move sideways toward the channel walls so they are convected downward and back toward the bottom of the flow channel. This combination of upward and outboard motion imparted to the streamlines by the rising and spreading hydrogen bubble stream

creates the counter-rotating vortices observed on both sides of the flow centerline just downstream from the reaction site. As the flow continues to be convected downstream the vortex rotations die out and the flow resumes relatively stable non-rotational and uniform flow. All but the lowest regions of the main flow that travels along the sides of the reaction site are also turned upward and outboard, away from the reaction site. However, the lowest regions of this flow, that very close to the surface, is turned inward and convected toward the reaction site before also being turned upward and outboard by the rising bubble stream. Figure 18 is a two dimensional schematic drawing of the flow imparted to the main stream by the rising bubbles.
The motions described for streamlines on and near the centerline of the test section are consistent with classical flow phenomena. The rising bubbles impart both vertical and horizontal velocity components to the flow that are perpendicular to the main flow streamlines near the reaction site. When the main flow interacts with these components the main flow streamlines are twisted, curled and stretched into counter-rotating vortices that dampen out once the flow travels some distance downstream. A more subtle relationship exists between reactants in the chemical reaction that takes place on the surface of the test section.

Almost all of the evidence suggests that, for the horizontal geometry used in this investigation, the main flow filaments are convected away from the reaction site. However, as has been described in the photographs, the chemical reaction is continuous and vigorous along the entire length of the surface of the sodium metal. This indicates that sufficient hexanoic acid to sustain this reaction is present along the entire length of the sodium surface. Chambré and Acrivos [1956] suggest that the parameter $k/0.339S_c^{1/2}\beta$, relating to the rate of reaction at the surface, describes whether a reaction is chemically controlled or transport controlled. High values indicate a high reaction rate at the surface whereas low values indicate a low rate of reaction at the surface. Therefore, very small values of this parameter establish that the reaction is chemically controlled and very large values

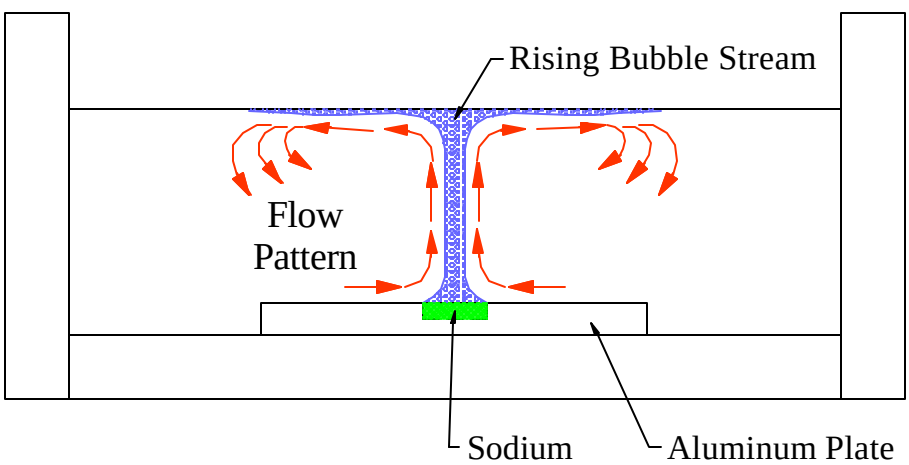

Figure 18. Schematic drawing of flow imparted to mainstream flow by rising bubbles.

establish that the reaction is transport controlled. In this parameter, k is the reaction rate constant, $S_c = \nu/D$ where D is the coefficient of diffusion in the mixture and $\beta = Re^{1/2} D/L$. Although the exact

values of k, D, S_c and β are not known, an order of magnitude approximation can be made from available data. This establishes that the value of the k is very, very small (on the order of 10^{-10} to 10^{-16} cm^3/molecule second) and D is very small (on the order of 10^{-5} cm^2/second). From knowledge of the main flow solution density and viscosity, $\nu = \mu/\rho$ so $\nu \approx 0.0042$ cm^2/sec^2 and $S_c^{1/2} \approx 20$. Finally $\beta = Re^{1/2} D/L$ where $Re \approx 350$, $D \approx 10^{-5}$ cm^2/second and $L \approx 45$ cm, so $\beta \approx 10^{-6}$. From these estimates, $k/0.339S_c^{1/2}\beta$ is on the order of 10^{-7} – very, very small. Accordingly, the Chambré and Acrivos parameter indicates this reaction is chemically controlled. Observations cannot dispute this finding but the last sequence of photographs indicate that at least some of the hexanoic acid necessary for a reaction may be coming from the lower portions of the flow that travels down each side of the reaction site.

5. MATCHED INDEX OF REFRACTION STUDIES

One of the tasks performed by the INEEL was take pointwise turbulence and velocity measurements with two-component laser Doppler velocimetry in the unique INEEL Matched-Index-of-Refraction flow system. Additional flow visualization work was also performed.

The goal of this portion of the study was to provide the scientific knowledge required to develop and to assess numerical predictive methods treating the key flow phenomena in generic simulations of drying/passivation problems in the environmental management of spent nuclear fuels. The objective of the INEEL tasks was to obtain fundamental measurements of the basic velocity and turbulence fields in generic idealizations of flow processes in SNF canisters during transfer and/or storage. As noted, proposed operating conditions give typically low Reynolds number flows. For an extensive literature survey of related work, see Condie, et al. [2001].

Choice of Experiments

The objective of the present tasks is to obtain fundamental measurements of the basic velocity and turbulence fields in the generic SNF canisters during the treatment process. As noted earlier, the expected range of inlet Reynolds number is about 2500 to 5000 for the potential applications. However, in the range $2000 < Re < 3000$ or so, the flow may be laminar, turbulent or intermittent depending on the entry geometry and the distance from the entry [Rotta, 1956; Lindgren, 1953; Patel and Head, 1969]. So at the lower end of the expected application range, the flow state at the exit of the tube (the jet) would be uncertain unless experiments were performed with the identical inlet geometry and flow rate. At some time in the future direct numerical simulations [Moin and Mahesh, 1998] may be able to predict this flow state adequately.

Two experiments were designed and conducted. The first was aimed at providing overall flow visualization for a fully-developed, turbulent entering flow. As a consequence of its simplicity, it was possible to obtain data for several flow configurations of interest. The second was a more detailed design to take advantage of the INEEL Matched Index of Refraction flow system and its two-component laser Doppler velocimeter for pointwise velocity and turbulence measurements. The inlet flow configuration selected could be expected to provide an intermittent flow, undergoing transition from turbulent to laminar [Patel and Head, 1969]. Consequently, the present study is expected to provide two inlet flows representing the range of conditions likely at the lower Reynolds numbers. While the second apparatus was designed for several configurations, only one configuration could be employed in the time available due the required duration of the time series measurements at each measuring location. For both experiments, most but not all measurements were obtained for Re 2500.

Overall flow visualization

Corroded spent nuclear fuel (SNF) elements may be passivated by injecting treatment gases into a storage canister containing the elements. For effective passivation, a design aim would be controlled, moderately high mass transfer rates to the fuel elements. These rates would depend on the flow pattern and turbulence levels in the vicinity of the elements. By developing a reliable predictive technique for the energy, mass and momentum transfer in the presence of surface reactions, transfer and storage systems can be efficiently and safely designed. An overall objective

of the research program described in this report is to understand the fluid physics of the passivation process. This objective was pursued by using flow visualization techniques and experimental measurements of the flow field to support computational models.

A water-flow experiment with a 3/4-scale model (relative to the idealized canister) has been used for overall flow visualization and velocity measurements, with and without an array of simulated fuel elements. Its purposes were to obtain initial indications of the gross flow behavior and to investigate the circumferential periodicity of the flow. Standard flow visualization techniques, using fluorescent dyes and neutrally buoyant particles illuminated by laser and white light, were employed. Observations have been made with perforated plates (representing basket support plates) having three hole geometries, with and without simulated fuel elements.

Flow visualization experiments were performed in a transparent, approximately 3/4-scale geometric model of our idealized canister in a water loop. The apparatus is shown schematically in Figure 19. The cylindrical canister contains four simulated fuel element tubes symmetrically distributed. The region contained between the bottom plate of the simulated canister and simulated bottom plate of a basket will frequently be called the "inlet plenum" or plenum region since it has some features of the plenum of a shell-and-tube heat exchanger or a nuclear reactor. The inlet plenum width is twice that of the inlet pipe diameter. The interface between the inlet plenum and the simulated fuel element bundle consists of a perforated (porous) plate, which simulates a basket support plate. Three geometries of simulated basket support plates with 50%, 8%, and 4% porosity were used. The 4% and 8% porosity plates lie within the 3% to 9% range of porosities of typical storage canisters. Plate perforations consist of holes drilled in a square lattice array with 1.90 cm spacing between holes. The spacing is three-quarters that of the idealized prototype. The 50% porosity plate was used to investigate the effects of plate porosity on the flow field further.

The inlet flow to the apparatus is provided by gravity feed from an approximately 60 liter

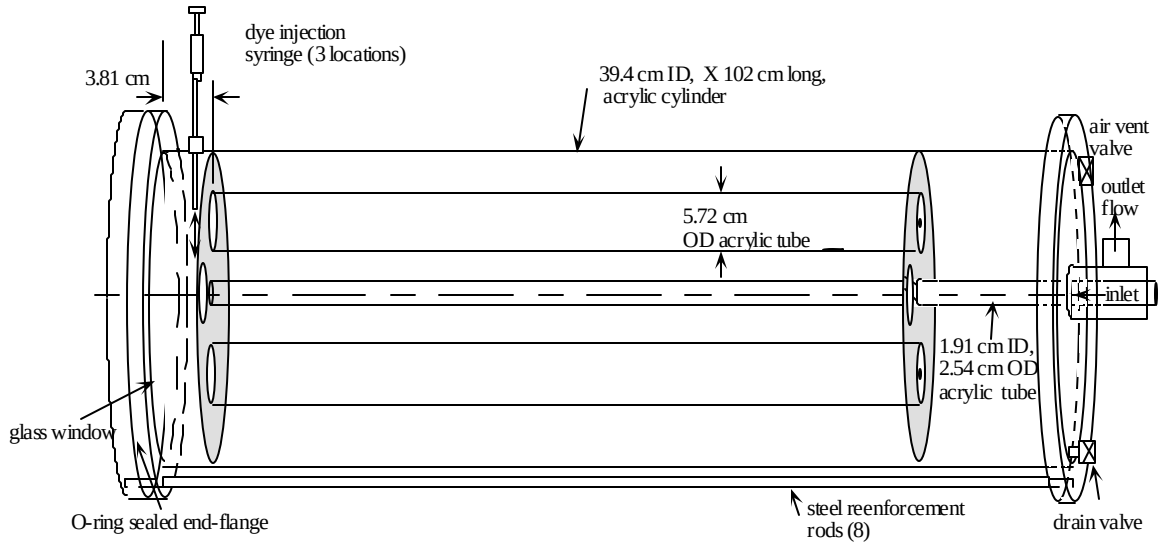

Figure 19. Schematic diagram of apparatus for flow visualization.

reservoir which is elevated about one meter above the apparatus inlet. Flow from the apparatus is

collected in a separate reservoir where it is pumped continuously back to the inlet reservoir. Gravity feed and pump flow rates are controlled by valves. Reynolds number scaling of flow rate to the prototype is employed. The experiments reported employ an inlet tube Reynolds number of 2,500 ± 100.

Due to the low velocities in the apparatus the fluid temperature profile in the flow loop must be close to isothermal if currents induced by natural circulation are to be avoided. The induced velocity is small in comparison with forced convection if the Richardson number, $Ri = g\alpha\Delta TL/V^2$, the ratio of buoyant to viscous forces, is significantly less than one. Because inlet fluid is effectively mixed with fluid in the apparatus in the inlet plenum, it is difficult to prescribe an effective ΔT. It was observed from flow visualization that fluid in the apparatus and reservoirs must be within approximately 1•C to avoid noticeable distortion of the flow pattern. The fluid is typically within 0.2•C of ambient temperature during experiments. The small temperature difference is due to pumping power and friction. The apparatus and reservoirs are filled several days before experiments are conducted to achieve near isothermal conditions. This waiting period also insures that the water is well deaerated so that bubbles do not leave solution and attach to walls (using Kodak Photoflo surfactant also helps prevent bubble formation and attachment). Bubbles are more of a problem for light scattering than for flow perturbation.

Flow visualization was performed using fluorescent dye and neutrally buoyant particles with laser light sheet illumination. A typical configuration for laser illumination is shown in Figure 20. The configuration for white light illumination is similar to that for laser illumination except that a collimated light source and a slit are substituted for the laser and light sheet generator. Collimated laser or white light sheets were also configured to bisect the inlet plenum and downstream of the perforated plate perpendicular to the flow axis. An example photograph of inlet plenum flow is shown in Figure 21 which shows a cross-section of an inner ring vortex (compare with later Figures 23 and 24). For the photograph, Rhodamine WT fluorescent dye was illuminated with a light sheet generated by an argon-ion laser. The light sheet approximately illuminated a plane midway between the perforated plate and the wall (window).

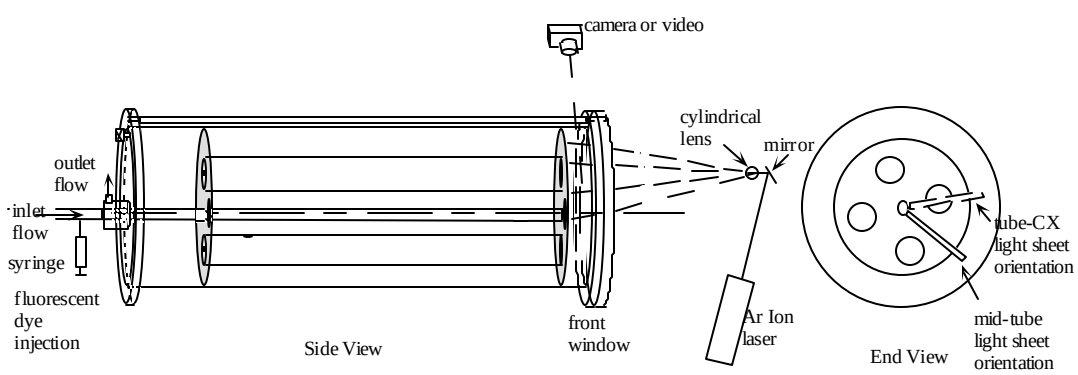

Figure 20. Schematic diagram of illumination for flow visualization using a laser light sheet.

The motions of neutrally buoyant particles were tracked from long duration photographs and from video recordings. The photographs and video images were then analyzed to provide fluid velocity information. The procedure for extracting two-dimensional, radial and axial, velocity

information from particle pathline photographs is as follows. First, photograph a dilute cloud of particles using collimated white light sheet illumination with sufficient sheet width (0.5 cm is typical) to insure that the majority of particles do not wander out of the beam during the exposure. A typical exposure duration is from 1/2 s for flow in the inlet plenum to 6 s for flow downstream of the perforated plate. Second, scan enlarged prints of the negatives into Canvas software (Deneba Software Inc.). Third, correct for distortion caused by refraction from photographing at an acute angle through a cylindrical wall. This process was done by linearly scaling to provide the same cylinder inside radius as equal axial length. Fourth, trace particle pathlines on a separate image layer in Canvas, then use flow visualization information and video recordings to determine velocity direction. Finally, transfer the velocity vectors to a cross-section drawing of the apparatus.

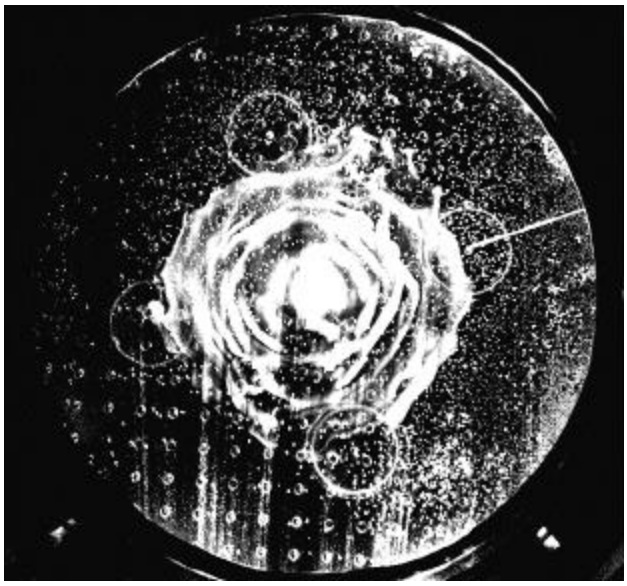

Figure 21. Visualization of vortex formed in the region contained between the bottom plate of the simulated canister and simulated bottom plate of a basket ("inlet plenum").

Another technique employed for extracting velocity information was to capture video images of the neutrally buoyant particles using a RaasterOps frame grabber board in a computer and then overlaying images for known time intervals. This technique was successful for characterizing the higher velocity flow field outside the wall jet in the inlet plenum. The velocity in the wall jet was too high to track individual particles between frames taken at 1/30 s intervals. Particle path line photography proved to be more successful outside the higher velocity eddies in the inlet plenum and downstream of the perforated plate. The much higher resolution of 35 mm black and white film compared to video images permitted a wider field of view for particle tracking.

The neutrally buoyant particles were silver coated hollow glass spheres of approximately fourteen microns in diameter. These spheres are available from TSI Incorporated. The spheres exhibit a fairly broad range of densities. This density variation would not be a problem for turbulent flow. However, for low Reynolds number laminar flow the spheres must be more closely neutrally buoyant. Near-neutral buoyancy was achieved by mixing a batch of spheres with water in a beaker and waiting several hours. The majority of the particles settle to the bottom and many float on the surface. The remaining particles in suspension (calculated to be less than one per cent of the

total) plus water were removed using a hypodermic syringe and then injected directly into the apparatus. This method proved to be quite successful in providing the highly reflective neutrally buoyant particles necessary for particle tracking. One objective of these experiments was to find a suitable particle for PTV experiments proposed for the MIR model. We would use a similar technique to sequester silver-coated hollow glass spheres that are neutrally buoyant in the oil used in the flow loop)

Experimental uncertainties

The experimental uncertainties associated with the velocity vectors to be shown in Figures 23 and 24 result from a number of sources and vary with position. The sources include (1) uncertainty of visually interpreting path line length, (2) distortion caused by refraction through a cylindrical wall at varying angles to normal and (3) uncertainty associated with the transient shifting of flow patterns. The uncertainty in estimating flow rate is measured to be less than five per cent of measured value and is not significant relative to the uncertainties in velocity vectors.

The uncertainty of interpreting particle path line length is estimated as ± 20% of the measured length. The correction for distortion caused by refraction from photographing at an acute angle through a cylindrical wall was performed by linearly scaling the radial dimension to provide the same cylinder inside radius as equal axial length. This approach does not account for distortion due to the uncorrected wall curvature (somewhat similar to spherical aberration in a lens). This distortion increases with the angle from normal to the cylinder wall and was determined from photographs of a rule placed inside the water filled cylinder. The maximum distortion for camera view angles used in the photographs is estimated to be ± 20% of the measured length.

The overall RMS uncertainty [Cook and Rabinowicz, 1963] of determining the velocity vector due to the above sources, without considering the transient shifting of flow patterns, is approximately ± 30%. It should be understood that the vectors do not represent an average velocity for their positions. Average and instantaneous velocities could be determined in experiments using Particle Tracking Velocimetry (PTV). This technique would provide more accurate velocity measurements with three-dimensional velocity components rather than the two-dimensional components described in this report.

Results

Experiments were conducted to determine the canister flow field with three perforated plates with open areas of 50%, 8% and 4% (porosities). Experiments reported are for inlet tube Re = 2,500 ± 100. Although laminar flow in a smooth tube can occur at Reynolds number as high as approximately 40,000, it is believed that the tube is sufficiently long and the entrance conditions sufficiently abrupt to insure that turbulent flow exits the tube and impinges on the plate.

With a 50% open area plate, the flow pattern is comparable to that of a submerged impinging jet on a semi-infinite plate with formation of a large vortex and entrainment and recirculation through the holes in the perforated plate near the center. Downstream flow is primarily through the outer holes. A single main recirculating eddy forms encompassing the plenum and part of the region for the element array. The flow pattern, as determined from the various flow visualization techniques, is shown in Figure 22.

With the 4% and 8% open area perforated support plates, recirculation regions occur downstream of the plate and two main recirculation zones (plus a small corner flow vortex) form upstream of the plate. Flow does not reenter the inlet plenum through the plates with less open area as it does with the 50% open area plate. In these cases the flow pattern in the inlet plenum has some features of a confined impinging jet [Morris and Garimella, 1996].

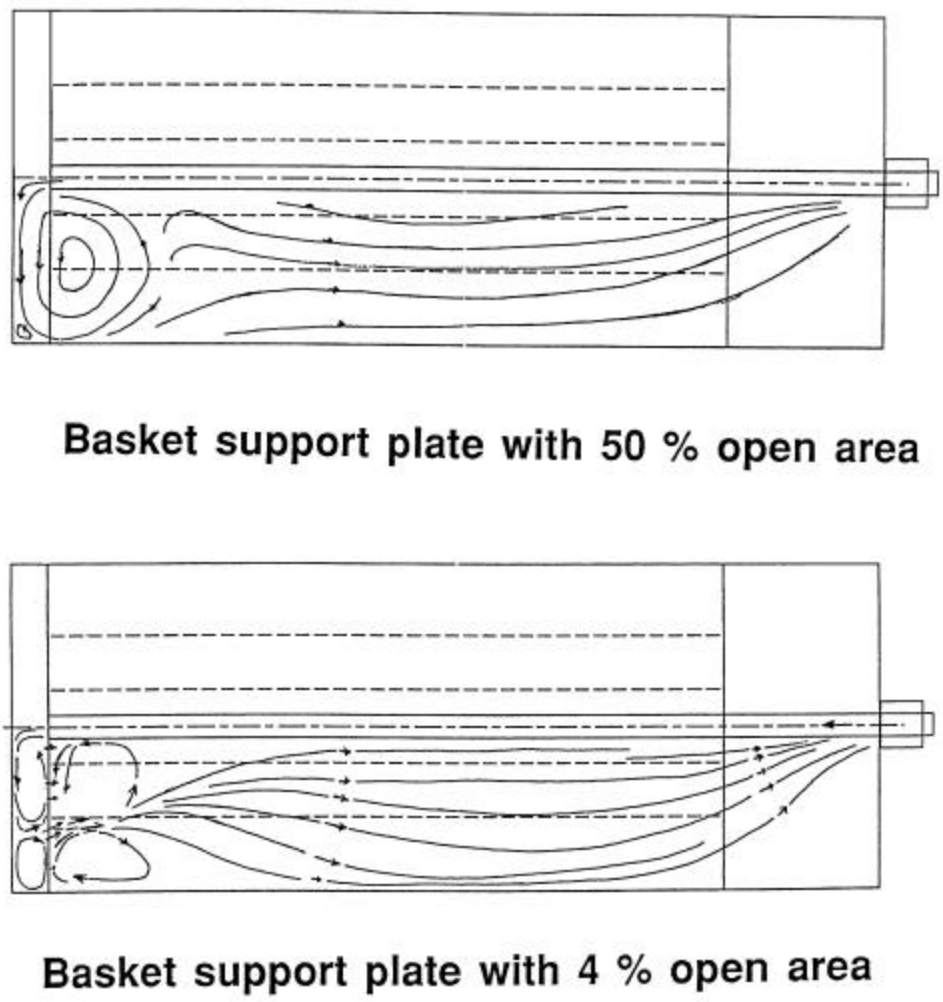

Figure 22. Effects of design of basket support plate on simulated canister flow shown by deduced streamline patterns for (top) fifty percent open area and (bottom) four percent open area.

The flow is approximately circumferentially periodic and symmetrical about cross-sections through the four outer tubes for experiments using each of the three perforated plates. This observation implies that numerical predictions and detailed measurements can concentrate on an 1/8-the sector of the idealized geometry rather than the full cross section. The flow is only approximately symmetrical because of time varying asymmetry of flow development in the inlet plenum, shown in Figure 21, and vortices downstream of the 4% porosity plate that slowly oscillate in position. The positions of the vortex centers may vary by one or two centimeters

(approximately D_{tube}) over a period on the order of one minute. Although the vortices are similar in different quadrants, the positions of their centers do not appear synchronized in time.

Flow visualization experiments show tube cross-flow and resultant vortex shedding, although the vortices do not show the clear alternating pattern of a Karman vortex street [Tritton, 1977]. A Reynolds number based on tube diameter of approximately 40 is about the highest number for which there is no unsteadiness due to vortex shedding [Tritton, 1977]. This Reynolds number corresponds to a cross-flow velocity of only approximately 0.004 cm/s for water flow across the 5.72 cm diameter outer tubes. The measured tube cross-flow velocities near the 4% open area plate (Figure 23) are position dependent, but are of the order of 0.1 cm/s, which corresponds to $Re_D \approx$ 1,000 (transition to turbulence occurs at approximately $Re_D = 3 \times 10^5$ for a cylinder in cross flow).

The vortex shedding frequency should scale with Strouhal number, St = fD/U, a non-dimensional frequency. A typical value of St for laminar flow is about 0.2 [Tritton, 1977] although there is no reason to expect one specific value for a non-uniform velocity distribution. Overall the Strouhal number is observed to be a function of Reynolds number [Tritton, 1977]. The observed variations in eddy positions occur with a frequency of approximately one minute with a variation of at least ±30 s. The variation implies that this behavior may be a chaotic process, in the sense that the flow has uncorrelated behavior, exhibiting sensitive dependence on initial conditions [Tufillaro, Abbott and Reilly, 1992]. The three dimensions of fluid motion further the possibility of chaos. (We have not investigated this aspect mathematically.) Strouhal number scaling may be used to estimate the vortex shedding periods to be expected in the MIR model and in the prototype canister, which would be approximately 3 s and 0.3 s respectively, assuming Reynolds number scaling of cross-flow velocity for Re = 2500. A non-dimensional wavelength (λ/D) for the vortices may be expressed as $\lambda/D = U/fD = 1/St$. If St is approximately constant in the models and the prototype for the same Reynolds number then the non-dimensional wavelength should also be approximately the same in the model and the prototype. This non-dimensional wavelength preserves the geometric scaling implied in Reynolds number scaling.

Results from experiments using the apparatus containing the inlet tube and the 4% porosity plate, but with the outer tubes removed, indicate that the vortices downstream of the plate are not solely formed by vortex shedding from the tubes. The circulation pattern within a distance of about one cylinder radius downstream of the plate is similar to the mid-tube cross section flow shown in Figure 24, complete with the vortex near the plate and one vortex downstream of the plate. The two main counter rotating vortices in the inlet plenum shown in Figures 23 and 24 are present in about the same positions.

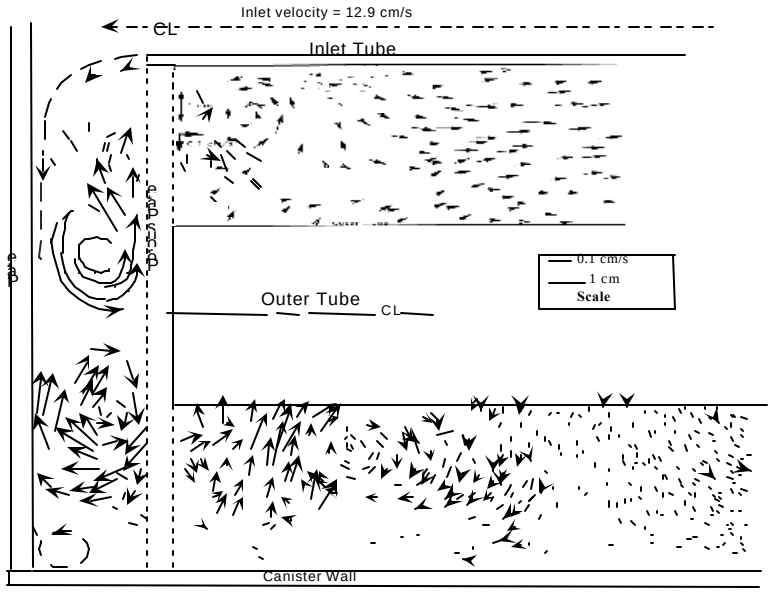

Figure 23. Instantaneous velocity distribution in a plane through the simulated fuel elements, $Re_{tube} \approx 2500$.

With the tubes removed, subsequent vortices downstream of the plate as shown in Figure 24 are not present and the flow approaches an approximately parabolic laminar velocity profile within about three cylinder radii downstream of the plate. The fully developed laminar velocity profile for an annulus has the form $U(r) = -r^2 + A*\ln\{r\} + B$, where r is radius and A and B are constants. This approach to a laminar profile is consistent with the criterion that, for a circular tube flow, fully-developed flow is approximately achieved within about L/D = Re/30 [Smith, 1960]. The Reynolds number in the array downstream of the plate based on hydraulic diameter is approximately 70 for an inlet Re = 2,500. With the tubes present, vortices persist for the majority of the tube bundle length and the flow only starts to approach a fully-developed laminar profile near the exit of the bundle ($L/D_h \approx 6$, where D_h is the hydraulic diameter ≈ 18.3 cm).

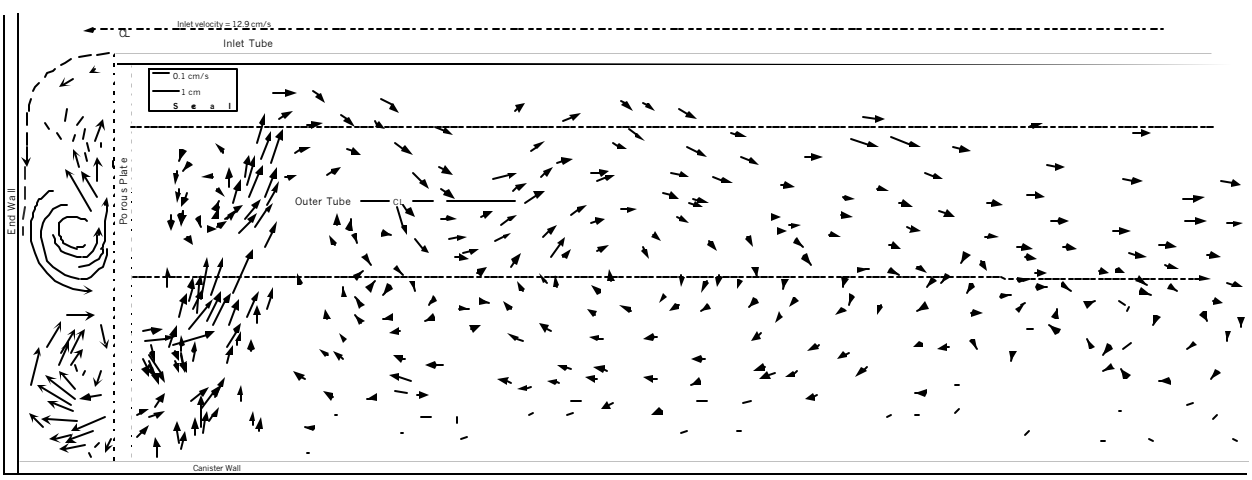

Figure 24. Instantaneous velocity distribution in a plane mid-way between the simulated fuel elements, $Re_{tube} \approx 2500$.

Discussion

The experiments fulfilled the objective of providing flow field information to be used for design of the experiments conducted in the Matched Index of Refraction (MIR) flow loop. A successful means of selecting neutrally buoyant particles for use in either this water flow loop or in the oil-filled MIR flow loop was also demonstrated. The experiments accentuate the difficulties of obtaining accurate velocity information in a non-index matching flow loop and of characterizing a transient three-dimensional flow field with two-dimensional short duration representations.

It is apparent from these experiments that despite the conceptual simplicity of the canister design, the flow pattern is very complex. Of concern is the uneven flow distribution near the surface of the simulated fuel rods. Higher velocity is observed near the surface towards the canister centerline than towards the outside, where, except near the perforated plate, the velocity is an order of magnitude lower than near the inside. A more even flow distribution is expected to provide more uniform drying and passivation in the radial direction. Possible design changes that could provide a more uniform distribution include (1) an optimized distribution of perforated plate holes; (2) a longer inlet plenum length (to decrease radial velocity tangent to the perforated plate which will presumably provide a more even flow distribution); and, (3) a higher packing density of fuel rods, although criticality considerations may not permit this approach. The canister and plate geometry might be optimized using a CFD code once it has been verified that the code can predict the flow field reliably.

The mean flow in the semi-confined impinging jet region between the bottom of the canister and the perforated plate ("plenum" region) was not sensitive to the presence of fuel elements in the basket. However, in independent studies, McCreery [1999] found that the location of the vortices that form at the separation of the wall jet was sensitive to the plenum aspect ratio, s/D. This trend is comparable to that found by Morris and Garimella [1996] for confined impinging jets. For both the semi-confined (present) and confined cases, the non-dimensional location varies approximately as the square root of the aspect ratio. An additional influence is to provide a more even distribution of flow through the plate as aspect ratio increases. The most evenly distributed flow (although far from perfect) was found for an aspect ratio of four. This result may be due to the occurrence of decreasing radial velocity and a more even pressure distribution adjacent to the plate as aspect ratio increases.

Matched-Index-of-Refraction Experiments

At the INEEL Matched-Index-of-Refraction (MIR) facility, matching of the refractive indices of models and fluid allows measurements in and around complex geometries by optical techniques without disturbing the flow. A 0.6-scale model of the generic SNF canister was installed in this facility to obtain detailed pointwise data for the three-dimensional turbulence field (and mean velocity field) by laser Doppler velocimetry (LDV). New velocity and turbulence measurements concentrated on low Reynolds number turbulent flow in the entry tube and the semi-enclosed impinging jet outflow or plenum region for a tube/jet Reynolds number of 2510. These measurements examine the first two flow phenomena in the sequence that leads to surface passivation and/or drying.

The benefit of the MIR technique is that it permits optical measurements to determine flow characteristics in passages and around objects to be obtained without locating a disturbing transducer in the flow field and without distortion of the optical paths. With a transparent model of different refractive index than the working fluid, the optical rays can be refracted in such a manner that measurements are either impossible (e.g., cannot "see" the desired location) or require extensive, difficult calibrations. Thompson, Bouchery and Lowney [1995] demonstrated this situation conceptually when laser Doppler velocimetry is applied to a rod bundle; with refractive-index-matching the measurement and position determination are relatively straight forward while without matching the beams may not cross to form the measurement control volume at the desired focal length, if they cross at all. The MIR technique is not new itself. Corino and Brodkey [1969] employed it to measure turbulence structure in a circular tube earlier. Recent applications of the technique include, but are not limited to, those of Durst, Jovanovic and Sender [1993], Parker and Merati [1996], Cui and Adrian [1997] and Becker et al. [1999, 2002].

The advantage of the INEEL system is its large size, leading to improved spatial and temporal resolution. To date most other experiments with index matching have been small, with characteristic lengths of the order of five cm or less. In contrast, the INEEL MIR flow test section has a cross section of about 60 cm x 60 cm and is about two meters long, allowing the use of models of substantial size. Since the system volume is over 3000 gallons, a light mineral oil was selected as the working fluid due to environmental and safety considerations; its refractive index matches that of some quartz. Figure 25 shows the test section with a test model installed for the present study. With the fluid temperature controlled, the quartz model can barely be seen at some wave lengths in the visible spectrum, e.g., the plates aligned vertically near the intersecting laser beams; indices are matched for the blue and green beams of an argon-ion laser (the external end containment plate is easily seen since it is made of acrylic plastic). The design flow rate can give Reynolds numbers up to about 10^5 based on the cross section of the test section. The refractive index of the fluid is maintained at the desired value by a parallel temperature control system which maintains a constant temperature in the test section to within 0.1ºC. In measurements in an experiment on transition induced by a square rib, meaningful velocity and turbulence data were obtained as close to the surface as $y^+ \approx 0.1$ and less [Becker et al., 1999].

Budwig and his students measured the viscosity, density and refractive index of the mineral oil used in the INEEL MIR as a function of temperature in his laboratory at the University of Idaho [Orr, Thomson and Budwig, 1997]. The thermal conductivity of the preliminary sample of the oil was measured by Sparell [1995] at three temperatures using the test method of ASTM E1225, modified for liquids. Based on the specific gravity one may estimate the specific heat from handbook relations. From this information, one may estimate the Prandtl number ($Pr = \nu/\alpha$) to be about 250 at 24°C. The main loop and temperature-control loop were equipped with several thermistor probes for temperature measurements. Differential pressure transducers and manometers can measure flow speed and static pressure using several pitot-static probes and various wall static pressure taps. An available hot-film anemometer system, for velocity or wall shear stress data, consists of a Dantec 56B10 Main Frame unit equipped with a 56N22 Mean Value unit and seven 56C17 constant-temperature bridges. The output of the constant temperature bridges can be acquired using a Power MacIntosh personal computer and its National Instruments MIO board. Available LabView software can display and store mean velocities, rms velocities and spectra information.

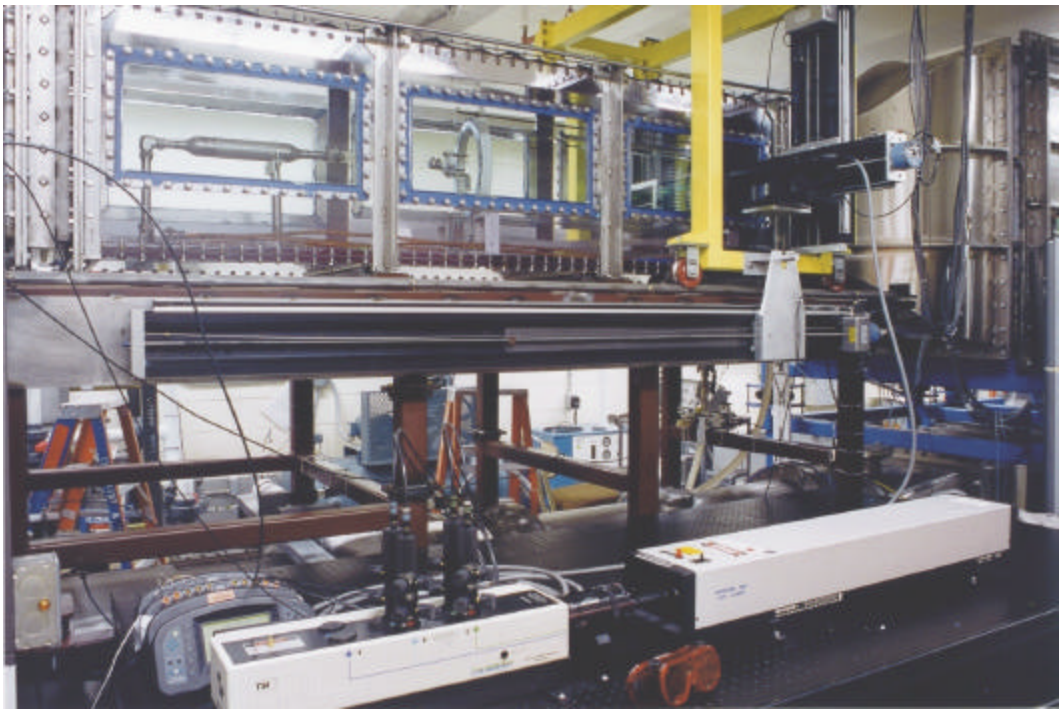

Figure 25. INEEL Matched-Index-of-Refraction flow system with quartz model installed to study the fluid physics of an idealized SNF storage canister (present study). Also seen are the LDV transmitting optics and three-directional traversing mechanism.

Velocity and turbulence measurements are primarily obtained with a two-component, TSI fiberoptic-based laser Doppler velocimeter. Transmitting (and receiving) optics are provided by a Model 9832 two-component fiber optic probe for 514.5 and 488 nm with a lens of 350 mm focal distance. Included in the probe is a Model 9832-XX-Lens collimating lens option to reduce the measuring control volume; the diameter is estimated to be about 60 μm in the MIR mineral oil. The laser is a water-cooled, 4 watt argon-ion Model Lexel 95. Beam splitting and frequency shifting are provided by a Model CB-2F ColorBurst system. Signal analysis and data processing are accomplished via a Model S65-2 two component signal analysis system including a two-channel IFA 655 digital burst correlator and FIND-W (Flow INformation Display-Windows-based) software. For acquiring additional signals such as flow rate, temperature and hot-film measurements simultaneously, a TSI Model DL4 four-channel "Datalink" multichannel interface is available.

Data acquisition is controlled via the FIND-W software for the LDV system. Desired traversing locations plus measuring parameters are specified by the operator and then the sequence is initiated. Data reduction to determine mean quantities and/or spectra is accomplished later, using other FIND-W subprograms. Ultimately, the raw time series data are transferred to permanent magnetic or optical storage media such as compact discs.

While the backscattering LDV mode [Durst, Melling and Whitelaw, 1976] is more convenient in operation, the validated data rate is much lower than when using forward scattering for the same conditions. To obtain statistically meaningful results, longer measuring times are required with

backscatter than forward scatter. Since its low velocities lead to inherently “slow” characteristic times for flow phenomena in the MIR system, it is desirable to employ forward scattering to avoid longer measuring times than needed.The traversing mechanism was designed to use the LDV in the forward scattering mode and to avoid relative motion between the test section and the optics. To accomplish the latter objective, it is mounted directly on the structure supporting the test section. For vertical motion, platforms on each side of the test section are moved simultaneously under precise computer control to maintain alignment of the transmitting and receiving optics.

In order to match the refractive indices, the refractive index of the oil is varied by adjusting the oil temperature via the temperature control system. The temperature at which the indices are matched best was determined by experiment. With the LDV placed so one blue beam passed through a quartz rib and one green beam passed through a horizontal plate of a test model, the LDV data acquisition was operated in the two-velocity coincidence mode and oil temperature was gradually varied [Stoots et al., 2001]. The maximum sampling rate that was obtained served to indicate the best temperature for operation so that the blue and green measuring control volumes were most coincident (the refractive indices vary with wave length so there would be a slight difference in positions when in oil). For the oil in the MIR flow system this maximum occurred at about 23.7°C.

Experimental uncertainties

The following uncertainty analysis is derived largely following the approach of MacManus et al. [1996]. Instead of presenting a single overall uncertainty value, individual sources of uncertainty are discussed.

Particle Behavior. LDV measurements require seeding of the flow field with a second phase such as particles, bubbles or droplets. In this work, it is believed microbubbles were the seeding particles. There are two criteria that must be met to ensure that the movement of the bubbles truly represents the turbulent movement of the continuous phase. First, the size of the bubbles must be smaller than the Kolmogorov microscale. Second, the inertial relaxation time of the bubbles should be less than the Kolmogorov time scale. The procedure recommended by Calabrese and Middleman [1979] may be used to estimate the inertial relaxation time [Stoots et al., 2001].

Frequency Measurement. The manufacturer's specifications claim that their IFA 655 digital burst correlator has a resolution of 0.05 per cent of the reading.

Optical Errors. Great care has been taken by the investigators to ensure that the alignment and intersection of the beams within the flow field are correct. Since the index of refraction of the oil is wavelength-dependent as well as temperature-dependent, matching indices of refraction for both beam wavelengths simultaneously is impossible; the optimum temperature for the green component of laser light is not exactly the optimum for the blue. Thus, some misalignment can be expected when more than one beam passes through quartz and oil. The temperature at which the indices are matched best for both components was ultimately determined experimentally. In order to match the refractive indices, the refractive index of the oil was varied by adjusting the oil temperature via the temperature control system. In an earlier experiment, with the LDV placed so one blue beam passed through a quartz rib and one green beam passed through a quartz horizontal plate of test model, the LDV data acquisition was operated in the two velocity coincidence mode for short time series and the oil temperature was gradually varied [Stoots et al., 2001]. The maximum sampling

rate that was obtained served to indicate the best temperature for operation so that the blue and green measuring control volumes are most coincident. For the oil in the MIR flow system this maximum in coincidence sampling rate occurred at about 23.7°C. A comparable test conducted with the small central tube of the present model reconfirmed this temperature as best for its GE 214 quartz. At this condition the reduction in overlap of the two MCVs is estimated to be about thirty percent of their lengths, thereby reducing the size of the effective MCV when operating with the coincidence mode. There is also an uncertainty in the crossing angles of the beams (and focal distances) in air or oil that leads to uncertainties in the velocities [Schwartz, Lesniak and Murthy, 1999]. The value is an approximately constant error but usually our normalized presentation will cause this error to cancel from the results presented.

Statistical Uncertainties Due to Finite Sample Size. Estimation of the statistical errors encountered due to a finite sample size followed the approach presented by Bendat and Piersol [1986] and used a typical sample size of 10,000 and measurement time of six to eight minutes. Yanta and Smith [1973] have plotted the number of points required to obtain desired accuracies in the statistical estimation of mean velocity and its standard deviation (rms fluctuation) within a given confidence level. They conclude that with u'/U of about fifteen per cent, 1000 data points would provide uncertainties of about one per cent in the mean velocity with a 95 % confidence level. For u' they predict that 1000 data points would give a statistical uncertainty within about five per cent with a 95 % confidence level. These estimates likely do not take into account the duration required to obtain the specified number of independent samples [Becker, 2001]. Further, in some low velocity regions considerable fewer samples were obtained at individual locations.

Positional Accuracy. For all three directions, motion is accomplished with traversing mechanisms consisting of a spindle and a stepper motor. The spindle advance is 40 threads/inch. The stepper motor gives 200 steps per revolution, corresponding to an advance of about 3μm per step. The position is determined with an “Accu-Rite” indicator with manufacturer's specifications of an accuracy of +/- 0.0001 inch or about 2.5 μm; its meter reads in increments of 2 μm. Indicated variation in position while the system is warming is about 5 μm. The positional accuracy becomes important in deducing the wall shear stress and the wall location from fitting the measurements for $y^+ < \sim 3$. Thus, the absolute uncertainty of a position is of the order of 5μm but for positioning during a continuous traverse the relative positioning uncertainty is less.

Temperature Accuracy. The index of refraction for the oil is a relatively strong function of temperature [Orr, Thomson and Budwig, 1997]. Mismatch of the indices of refraction for the oil and quartz plate can result in movement of the measurement volume as well as distortion of the fringes within the measurement volume. Durst, Keck and Kline [1979] recommended that the indices of refraction should be matched to the fourth decimal point (i.e., 0.0001). For the oil used in this work, the temperature control must therefore be better than +/- 0.3°C. Temperature control tests were conducted with both water and oil in the loop. Measurements of the spatial and temporal variation with a precision thermistor probe have shown spanwise uniformity and steadiness within 0.1°C [Stoots et al., 2001].

Uncertainties in oil properties. The properties of the light mineral oil were measured by Orr, Thomson and Budwig [1997]. An indication of the precision of these data is provided by their variations for 3σ; these were 0.002 g/cm^3 and 0.3 centistokes or about 0.3 and two per cent of

typical values, respectively. The latter uncertainty would dominate the uncertainties in Reynolds numbers, making them of the order of two percent of their calculated values.

Calibration. To obtain a measure of the accuracy of the overall LDV system during its initial installation, the mean velocity indicated by the data processing system was compared to that of a rotating "calibration wheel" passing through the measuring volume formed by the laser beams. The indicated velocity agreed with this standard to within about 0.3 percent. The variation along the axis of the measuring volume was less than one per cent of its average value. This variation is a contributor to the apparent turbulence intensities of the LDV technique [Condie et al., 1998].

Turbulence and Velocity Distributions by Laser Doppler Velocimetry

For the turbulent fluid physics experiments, a circular quartz model was designed, fabricated and installed horizontally. The design is described in Figure 26. With the exception of the bolts providing axial constraint, the materials are transparent; the structural end plates are acrylic and the remaining sections are finished quartz tubes and plates to match the refractive index of the light mineral oil. Tubular sections were fabricated from GE 214 quartz while flat ones were of GE 124 quartz.

The central tube has an internal diameter D of 14.99 mm and a length of about 105 cm ($L/D \approx 70$). In the present configuration the nominal dimensions are plenum spacing $H/D = s/D = 2$, canister internal radius $r_o/D = 9$, pitch of holes in the perforated plate $p_h/D = 1$ and hole diameter $d_h/D = 1/4$ in a square pattern. The configuration and dimensions of the perforated bottom support plate are presented in Figure 27. Quartz tubes representing spent fuel elements may be installed in the 71 cm long space corresponding to a basket. These dimensions are about 0.6 times those of the reference idealization. Figure 28 shows the model installed in the MIR test section with oil temperature approximately at the level for matching of the refractive indices. Since the matching is aimed at the blue and green wave lengths one can see some components faintly in other regions of the visible spectrum. Also visible are some rough surfaces, such as the holes in the perforated tube.

The inlet configuration is evident in Figure 25 on the left. A small circular plenum contains a flow straightener to avoid swirl from the upstream plumbing. The flow then passes through a standard reducer and extension to a flexible tube of one inch (25 mm) inside diameter and approximate length of 18 in. (460 mm) before an abrupt geometrical contraction into the quartz central tube of the model (I.D. = 14.99 mm and $L/D \approx 70$). The oil was circulated to the model through an auxiliary flow loop by a centrifugal pump driven by a motor controlled by a variable frequency drive. Flow was measured with a Micro Motion Coriolis mass flowmeter, Model CMF 100. The time-averaged mass flow rate was typically held constant to within about 0.05 percent from run to run and its rms fluctuation during a run was of the order of 0.4 percent.

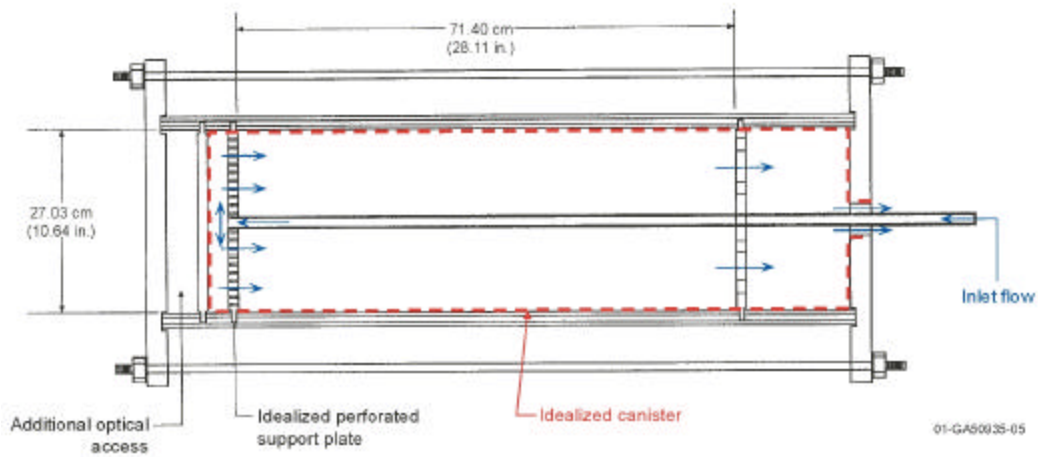

Figure 26. Design of 0.6-scale model for studies of the generic turbulent flow processes of idealized SNF canisters.

In accordance with the earlier discussions of the fundamental fluid physics questions involved, the objectives of the LDV experiments were to determine the inflow turbulence of the impinging jet and the turbulence and velocity fields of the flow approaching the perforated plate. The examination of these questions requires fundamental measurements of the decay of turbulence and velocity in the low Reynolds number impinging jet and its surroundings and of the low Reynolds number turbulent flow in the inlet tube.

For the present applications, design flow rates are expected to give tube Reynolds numbers between 2500 and 5000. Tabulated LDV data for mean and rms axial velocities are available from Lekakis for pipe flow at Re ≈ 4130 [Durst et al., 1996] and Satake et al. [2000] have direct numerical simulations at Re ≈ 4300, corresponding to the inlet conditions of Shehata and McEligot [1998]. Otherwise, the only profile data known in the range of interest are the tabulated mean velocity profiles by H. C. Reynolds with an impact tube at Re ≈ 3020 and 4080 [Reynolds, Davenport and McEligot, 1968] and the figures of Patel and Head [1969] at Re ≈ 2440, 2615, 2680, 3000, 4060 and 4430 with a pitot tube. Consequently, a byproduct of the present measurements is a set of new data for Reynolds stresses and mean velocities for flow in the range 2500 < Re < 4000 (along with laminar measurements for comparison to the analytical prediction, e.g., Kays [1966]).

As noted, most of the present data were obtained at Re ≈ 2500. At this Reynolds number for a tube of the present L/D of about 70, the velocity field can be expected to be fully laminar, fully turbulent or an intermittent flow undergoing a transition from the former to the latter [Rotta, 1956; Patel and Head, 1969]. For the development of a laminar flow from a uniform inlet velocity, Kays [1966] suggests that the approach of the friction factor towards 16/Re is a reasonable measure of the development of the velocity profile. Based on the analysis of Langhaar [1942], he notes that the friction factor is within two per cent by about (x/D) = Re/20 which converts to $x^+ = x/(r_w Re) \approx 0.1$ in terms of laminar entry coordinates. For a Reynolds number of 1500, this distance is about 75 diameters and at Re ≈ 2500 it would be about 125 diameters.

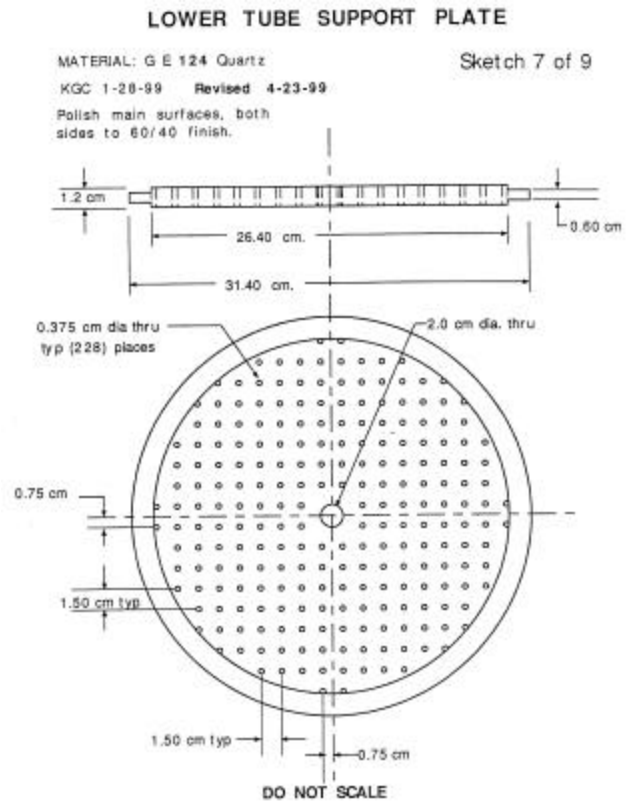

Figure 27. Fabrication sketch for simulated basket support plate.

Initial measurements of U, V, u′, v′ and $\overline{uv}$ have been obtained in the tube, about 1.7 diameters upstream from the exit for Re ≈ 1500, 2510 and 3500. These data provide the initial conditions for the jet which impinges on the bottom of the simulated canister. They also permit assessment of the models employed in numerical predictions.

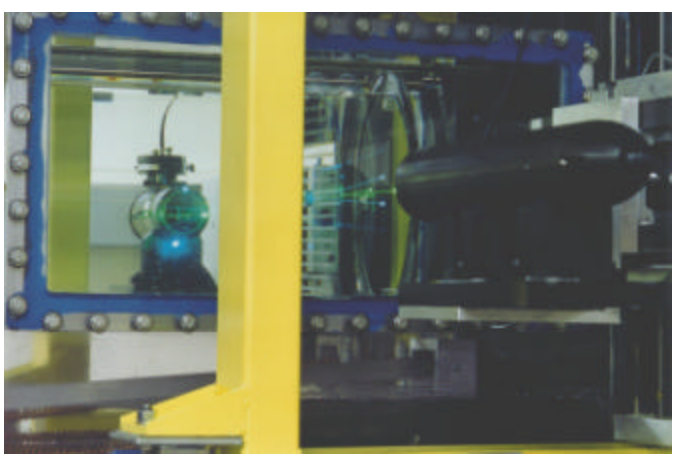

Figure 28. Model installed in MIR test section. The black ring is a gasket sealing the acrylic end plate.

At Re ≈ 1500 the mean axial velocity profile U{r} agrees closely with the expected parabolic profile for a fully-developed flow in a tube. At Re = 2510 this profile is flat across the central region of the tube as shown in Figure 29 (the data from the tube are represented by the diamond symbols). For a fully-developed laminar flow, the centerline velocity would be twice the bulk velocity whereas for fully-developed turbulent flow it would be expected to be $U_c/V_b \approx 1.3$ or so. The appearance of the profile is that of a developing one with a laminar boundary layer growing near the wall but not yet reaching the centerline. Since the measurement station is about 68 diameters from the tube entrance, this observation would be consistent with a laminar development length of about 125 diameters for this Reynolds number. However, the data for root-mean-squared fluctuations, u′ and v′, show evidence of turbulent behavior.

The data for Re = 2510 and 3510 have been examined in terms of the wall coordinates employed normally for developed turbulent flows. The variable y is the distance from the surface. Since the high Reynolds number asymptote is approximately logarithmic ($u^+ \approx 5 + 2.5 \ln y^+$), semi-logarithmic coordinates are employed [Kays and Crawford, 1980]. Results for the mean velocity are compared in Figure 30 to each other, to other investigators, to a laminar asymptote and to the turbulent law-of-the-wall. For fully-developed, low Reynolds number turbulent flow the levels of the profiles decrease as the Reynolds number is increased until they approach the law-of-the-wall or universal velocity profile approximately [McEligot, Ormand and Perkins, 1966]. The data for Re = 2510 have the appearance of a Blasius (laminar) boundary layer profile [Schlichting, 1979] when plotted in this form. Measurements from other investigators for the range 3000 < Re < 4400 are taken from the experiments of Reynolds [1969], Shehata [1984] and Durst et al. [1996]. It is seen that our values for Re = 3510 and x/D ≈ 68 are consistent with the data of others and their trends, as well as the observation of Patel and Head [1969] that the transition from laminar to turbulent flow proceeds rapidly along the tube for Re > 3000.

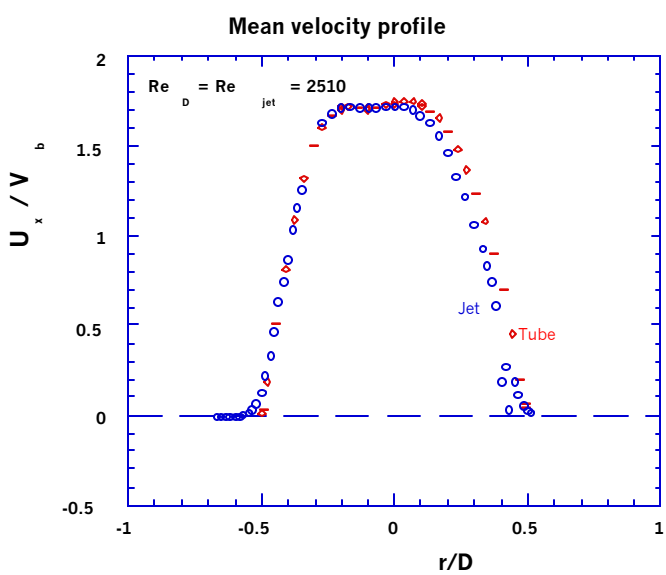

Figure 29. Axial mean velocity distribution entering the plenum region. The diamonds indicate the flow in the tube near exit, circles the initial station of entering jet.

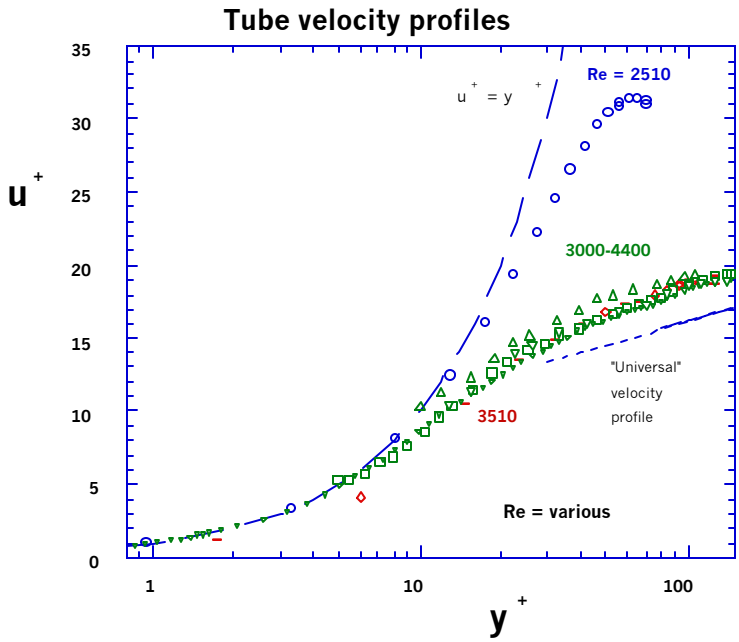

Figure 30. Mean velocity profiles at low Reynolds numbers in circular tubes. The circles and diamonds represent present data at Re = 2510 and 3510, respectively.

Some preliminary turbulence measurements were examined (Figure 31). Here the rms fluctuations have also been plotted in terms of wall coordinates; the non-dimensional axial component $(u')^+$ is represented by diamonds and the radial ones $(v')^+$ by circles. These data suffer from statistical uncertainty due to low data rates or short duration of sampling but they do demonstrate significant levels of turbulence. For comparison, Figure 32 presents typical results from a number of other investigators using a variety of methods plus direct numerical simulation [McEligot and Eckelmann, 2001]. While these data are for low Reynolds number turbulent flow in channels, results for circular tubes have approximately the same magnitudes [Durst et al. 1996]. One sees that for fully-developed turbulent flow, $(u')^+$ peaks at a value of about 2.5 near $y^+ = 15$ and $(v')^+$ has lower values with its peak further from the wall (not shown, but peak magnitudes are typically 0.8-1). The present data generally have lower values at comparable locations in Figure 32.

One can conclude that the flow from the inlet tube is one that is intermittently turbulent and laminar, i.e., undergoing axial transition. However, the mean velocity profile still has predominantly laminar behavior.

In the remainder of the results to be presented, most velocities and their fluctuations are normalized by the bulk velocity in the inlet tube ($V_{b,in}$) as one useful reference velocity. This quantity is equivalent to the bulk velocity at the jet entry and is about 55 per cent of the maximum velocity of the jet (or tube). For reporting the turbulence levels, turbulence intensities normalized by pointwise mean velocities are avoided because they can give misleading high values in regions of low velocities.

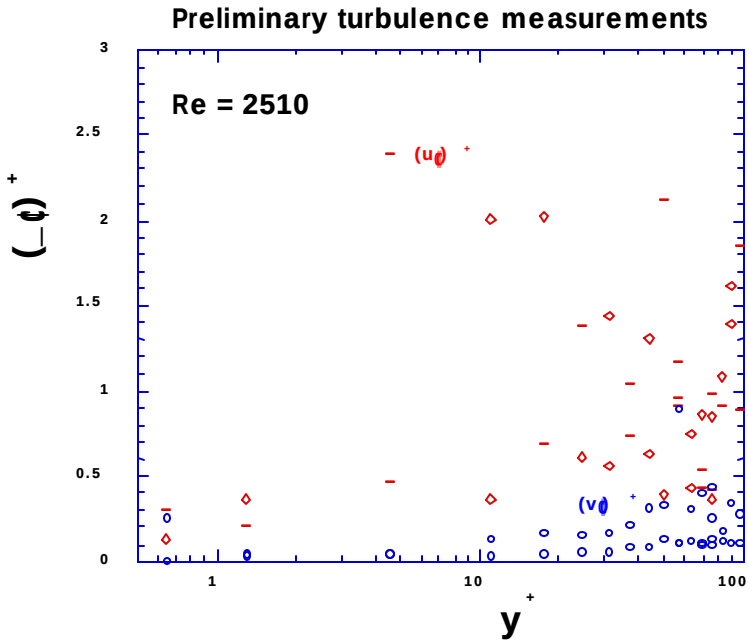

Figure 31. Root-mean-squared velocity fluctuations near exit of central tube normalized in wall coordinates, Re = 2510.

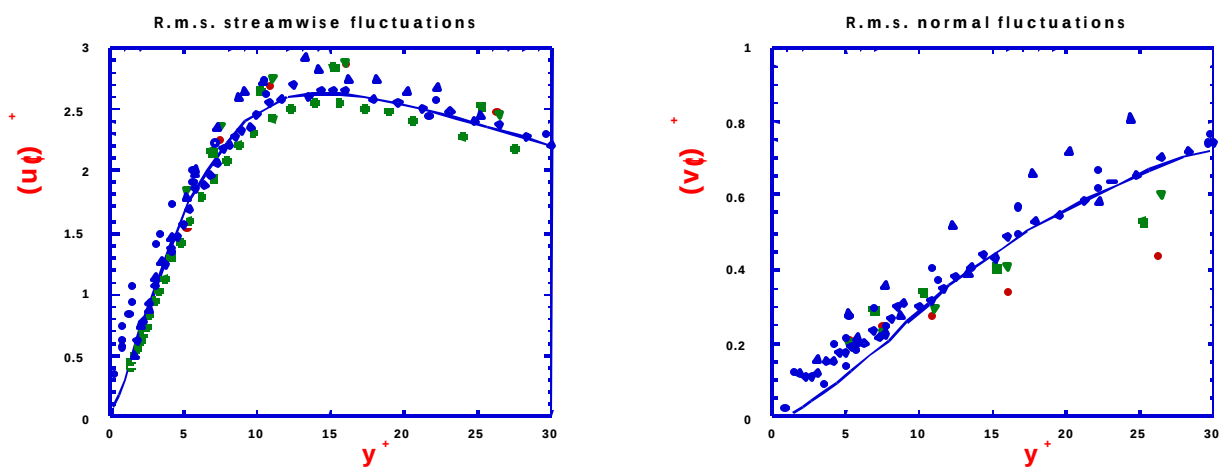

Figure 32. Typical measurements and direct numerical simulation of root-mean-squared velocity fluctuations at low Reynolds numbers by a variety of investigators [McEligot and Eckelmann, 2001].

The initial jet profiles are shown in Figures 29 and 33. The mean axial velocity is in the former and turbulence components in the latter. These measurements are at approximately 0.07 diameters from the tube exit. As expected, the mean profile is essentially the same as it is 1.7 diameters upstream inside the tube although one can see slight evidence of spreading or entrainment at the edges. For the jet, the axial fluctuations dominate over the radial ones. Highest values of u′ occur in the shear layer between the flat central region and the surroundings in the plenum region and reach magnitudes that are about twenty per cent of the inlet bulk velocity. This shear layer corresponds to

the upstream boundary layer in the tube. At this location the radial fluctuations are small with maximum values of the order of two per cent of $V_{b,in}$. Later it will be seen that in the semi-confined plenum region the radial fluctuations are much greater than the axial ones.

As noted previously, fluid physics data for impinging jets are sparse. Most of the extensive literature deals with heat transfer measurements. Only a few investigators report flow measurements for confined impinging jets and apparently none have examined the semi-confined geometry of the present study. Further, only a few experiments utilized a well-developed inlet flow for the jet [Cooper et al., 1993] as in the SNF application. The present objectives include understanding the turbulent or laminarizing flow field approaching the perforated plate, i.e., the upstream conditions for that plate. Even for confined jets, only Fitzgerald and Garimella [1996] appear to have measured turbulence quantities outside the impinging jet and its wall jet. They present rms radial velocity fluctuations, primarily in and near the wall jet at high Reynolds numbers. Emphasis on the region outside the wall jet is lacking in their study.

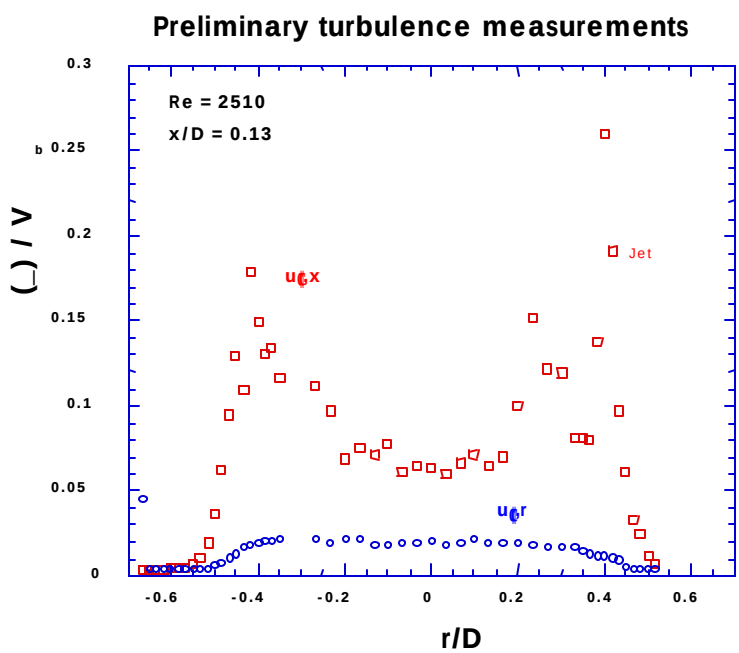

Figure 33. Root-mean-squared velocity fluctuations of inlet jet at initial station, normalized by bulk velocity in inlet tube.

Two-component LDV measurements of the turbulence structure and mean velocity distributions for the semi-confined impinging jet and its surroundings upstream of the perforated plate were conducted. Time series data have been obtained for: (1) radial profiles in the semi-confined region at $0.046 < x'/D < 1.97$; (2) free jet profiles at $-x/D \approx 0.07$, 0.5, 1.0 and 1.5; and (3) wall jet profiles at $r/D \approx 1$ and 1.3. The term x' is measured from the solid bottom plate and x is taken from the tube exit opposite to the direction of jet flow (however, the axial velocity U is taken as positive in the direction of the jet flow). These locations are on the vertical centerplane between the two middle rows of holes in the perforated plate so they are not directly affected significantly

by upstream influence from the holes. Additional subtasks would be desirable to address the behavior in a plane through a line of holes for comparison. The last two data sets provide data for comparisons of the initial behavior predicted numerically and to the higher Reynolds number experiment of Cooper et al. [1993].

The development of the free jet is shown in Figure 34 in terms of its axial mean velocity profiles. The circles are for the initial profile at 0.07 diameters and the profile at x/D = -1.5 is given by squares. There is no significant change as the jet proceeds halfway across the plenum (H/D = 2) except a slight increase in its breadth. By a half diameter from the impinging plate the velocity in the central region decreases as radial outflow from the stagnation region begins to feed the ensuing radial wall jet.

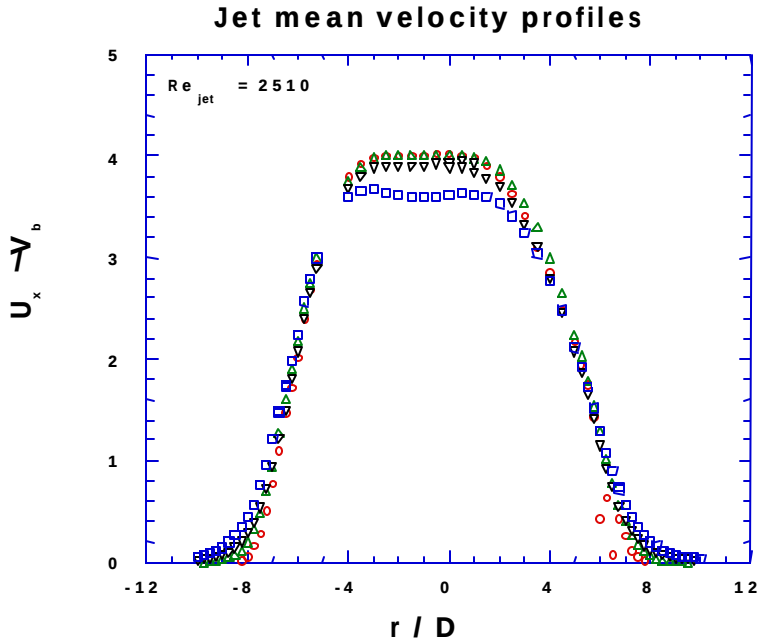

Figure 34. Development of impinging jet from initial station to x′/D ≈ 0.5 from impingement plate.

Overall behavior of the radial wall jet is shown later with the plenum region results. The initial conditions of this jet were measured at r/D ≈ 1, a location where tabulated data are also available from the experiment of Cooper et al. [1993] (courtesy of David Jackson, UMIST). Cooper et al. had an impinging jet from a fully-developed turbulent tube flow at Re ≈ 23,000, about an order-of-magnitude higher than the present experiment. Their impingement plate did not have another surface opposite to confine the flow. Consequently, we refer to it as a semi-infinite impinging jet. Though there are obvious differences from the present experiment, it is one of the few experiments with time-resolved data on the flow structure of impinging jets with a well-developed initial flow. The spacing from the tube to the plate was the same, s/D = 2. Available were profiles of the mean and fluctuation radial velocities at a number of radial stations. Figure 35 compares the mean velocity profiles and the turbulence measurements are in Figure 36. In these figures, the variable y is the distance from the impinging plate.

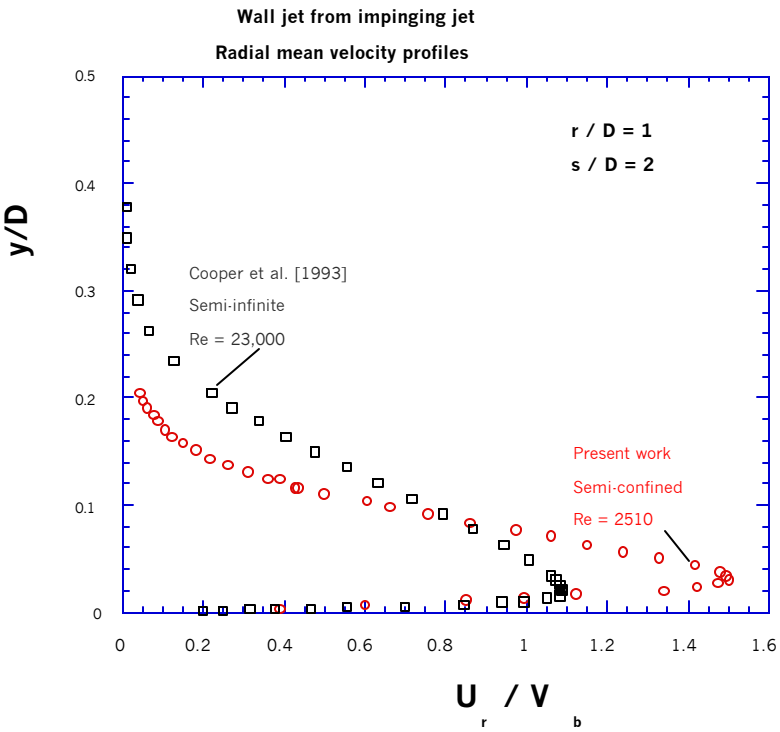

Figure 35. Mean velocity profiles of wall jets evolving from impinging jets near impingement region, r/D ≈ 1.

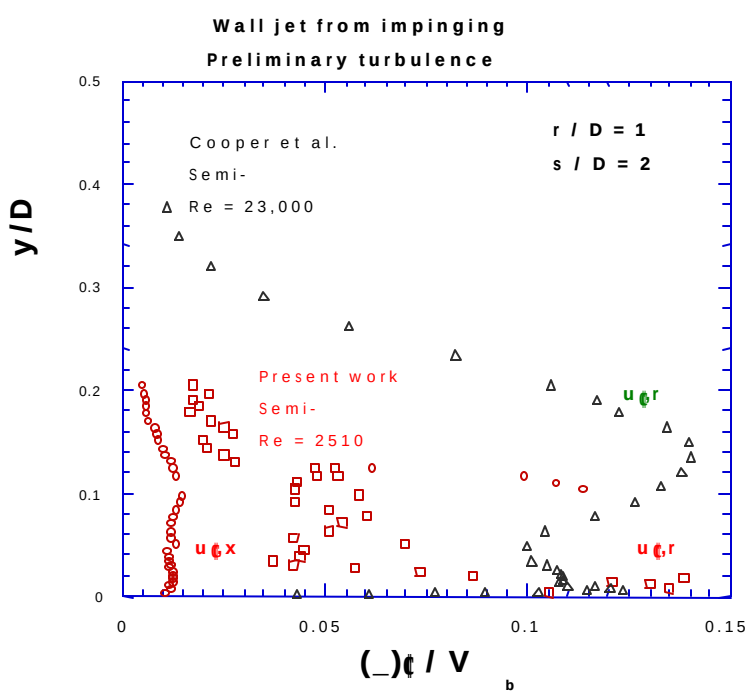

Figure 36. Comparison of profiles of root-mean-squared radial and axial velocity fluctuations in wall jet near initiation.

At the same non-dimensional location (one diameter from the centerline) the present wall jet is significantly thinner than the one of Cooper et al. and, consequently, the peak value of U_r/V_b (or

$V/V_{b,in}$) is greater. In the present experiment the maximum axial inlet velocity was about 1.8 times $V_{b,in}$, and the peak radial mean velocity was about 1.5 at this location. In the experiment by Cooper et al. the fully-developed turbulent tube flow had a lower centerline velocity, giving a lower non-dimensional momentum flow rate and the resulting peak radial mean velocity was only about 1.1 at the same radial position. Despite the thicker boundary layer, the peak in their turbulent wall jet was closer to the wall than observed in the present study.

In contrast to the free jet, the radial fluctuations in the wall jet are mostly greater than the axial ones. The root cause is likely the different orientation of the nearby constraining surface. In Figure 36 the radial fluctuations $v'/V_{b,in}$ (denoted u′,r) are represented by the squares the axial ones by the circles, and triangles show the radial fluctuations of Cooper et al. In both experiments significant radial fluctuations are seen further from the wall than the apparent mean boundary layer. Again the region of Cooper et al. is thicker than ours. Their fluctuation profile shows two peaks, one corresponding to the region of maximum shear stress in the outer region and the other in the near-wall region as turbulent boundary layers with an imposed freestream flow. Our v′ peak is about the same magnitude as the maximum of theirs, about fourteen per cent of $V_{b,in}$, but its location corresponds to the high shear region near the wall whereas their highest values are in the outer region. Although v′ is generally greater then u′ there appears to be a “spike” in the present data approximately at the high shear region at the outer edge of the wall jet (it is not clear whether this occurrence is fortuitous).

The flow in the inlet plenum provides the upstream conditions for the flow through the perforated plate simulating a basket support plate. For Re = 2510 this flow pattern is presented in Figure 37 in terms of mean velocity vectors. This plane is on the vertical centerline of the model between two vertical rows of holes as seen in Figure 27. Main features are the high velocity impinging jet, the thin expanding wall jet, a large recirculating eddy near the outer wall of the canister and relatively low velocities near the perforated plate. The flow in the wall jet remains attached until it impinges on the outer wall of the plenum region and induces the main recirculating eddy. Only a single major eddy is seen rather than the two observed with the water flow visualization. Outside the impinging and wall jets, flow is relatively quiescent with velocities about an order-of-magnitude less than the inlet velocity. In the plenum region upstream of the perforated plate, the radial velocity component at a point is generally greater than the axial component, except in the recirculating eddy. In the vicinity of the perforated plate, flow is primarily radially inward. Tabulated values of this velocity distribution can be made available for comparison with the predictions of CFD codes proposed for canister flows.

The turbulence field upstream of the perforated plate may be examined in terms of contour plots of the magnitudes of the root-mean-squared fluctuating velocity components. Presumably, the higher the turbulent kinetic energy ($k = (u^2 + v^2 + w^2) / 2$) carried into the element array, the more effective the mass transfer to the elements. In the present experiment radial and axial components were determined. The present data would be suitable for comparison to predictions from Reynolds stress models [Hanjalic, 1999] or k-ε-v^2 models.

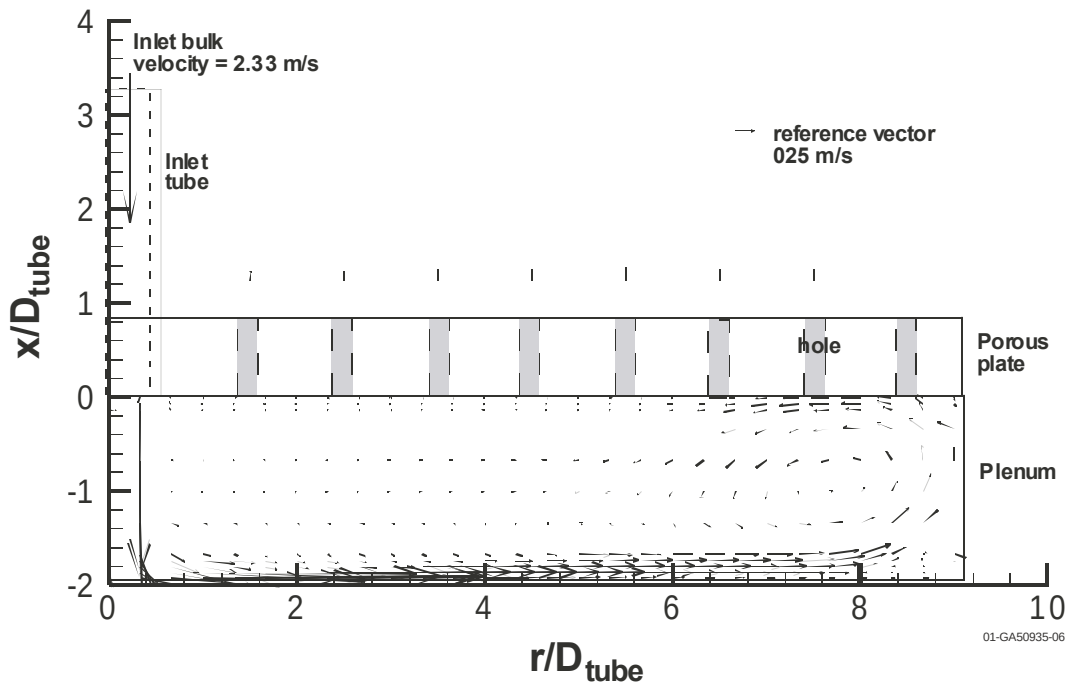

Figure 37. Mean flow pattern of a semi-confined impinging jet and its surroundings, Re_{jet} = 2510.

By using quartz for the canister end plate and perforated plates so that these transparent elements had the same refractive index as the mineral oil, it was possible to obtain LDV data for the component normal to those surfaces much closer than other investigators could. In this configuration, this component corresponds to the axial direction.

Contours for rms axial fluctuations normalized by the inlet bulk velocity are displayed in Figure 38. At the inlet jet, values are moderate, consistent with the inlet profile shown earlier in Figure 33. In the rest of the flow, $u'/V_{b,in}$ (denoted u′/U in the figure legend) is low with a slight increase in the region of the main recirculating eddy. With the exception of the outer region (r/D ‰ 7), values immediately upstream of the perforated plate are less than one percent of $V_{b,in}$.

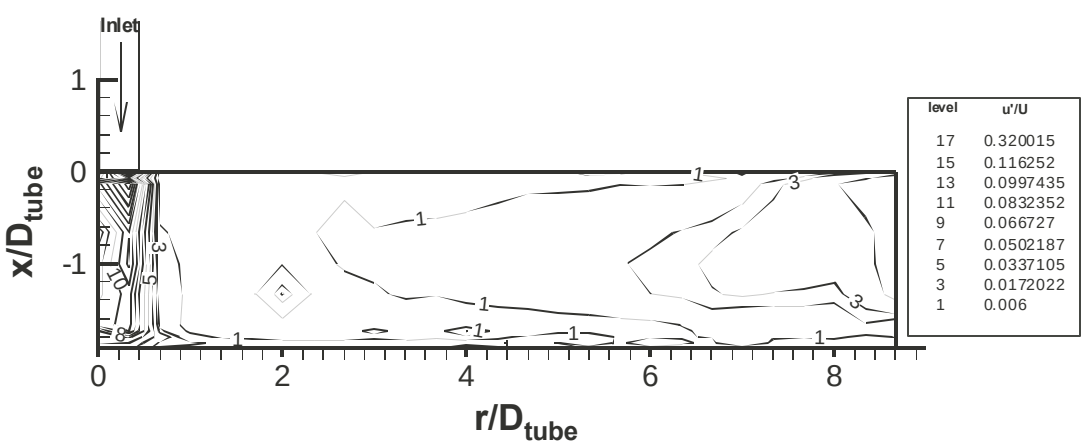

Figure 38. Distribution of root-mean-squared axial velocity component $u'/V_{b,in}$ for a semi-confined impinging jet and its surroundings, Re_{jet} = 2510.

The rms radial velocity fluctuations are generally considerably larger than the rms axial fluctuations. Although a local Reynolds number for the bulk outflow between the plates would vary from $Re_{D,h}$ (= 0.25 Re_{jet}/(r/D)) ≈ 1260 at r/D = 1/2 to zero at r_o, the turbulent fluctuations remain significant, and there is no evidence of a laminarization phenomenon. Figure 39 presents the normalized distribution of v′. High values are seen in the wall jet and moderate values mostly in its wake region or the half of the plenum near the wall jet. Moderate to high values also appear near the perforated plate in the region directly affected by the main recirculating eddy. Near the perforated plate in the range 0 < r/D < 7, v′ is still moderate while u′ is low. For the most part, v′ is the same order or larger than the mean radial V so the local turbulence intensities v′/V{r,x} are of the order of 100 percent or greater turbulence levels. These large relative values of v′ imply the likelihood that there are considerable fluctuations in the incident angle as the flow approaches the holes in the perforated plate. This situation differs significantly from flow conditioning applications of perforated plates in wind tunnels.

As shown by the velocity vectors in Figure 37, the eddy structure observed in the plenum region of the 0.6-scale MIR model with oil flow exhibited only a single torroidal vortex near the outer radius at Re ≈ 2500. On the other hand, the structure observed in the water flow apparatus (with a 4% open area perforated plate, similar to that in the oil flow apparatus) at the same Reynolds number showed two counter-rotating toroidal vortices (Figures 23 and 24). Therefore the difference in eddy structure was examined by conducting a series of flow visualization experiments at varying flow rates in both the oil flow and water flow models.

Flow visualization in the oil flow apparatus was achieved by injecting small air bubbles in the inlet flow line. The results were recorded photographically. Various camera shutter speeds were used to record bubble path lines. The results shown in Figure 40 were obtained using a duration of one second for Re ≈ 1650, and 1/2 second for Re ≈ 2200 and Re ≈ 4200. The photographic and lighting techniques were the same as for flow visualization in the water flow apparatus as described earlier in this report.

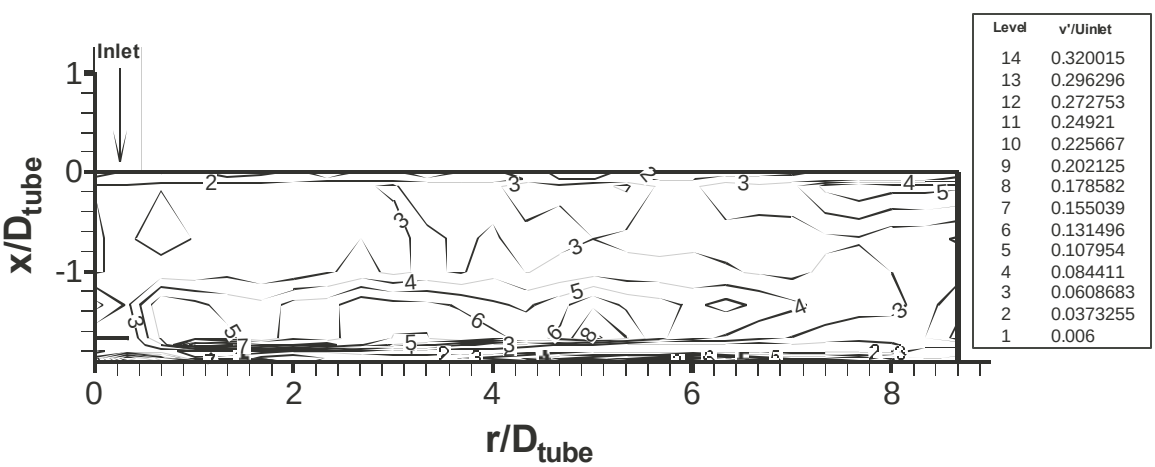

Figure 39. Distribution of root-mean-squared radial velocity component $v'/V_{b,in}$ for a semi-confined impinging jet and its surroundings, Re_{jet} = 2510.

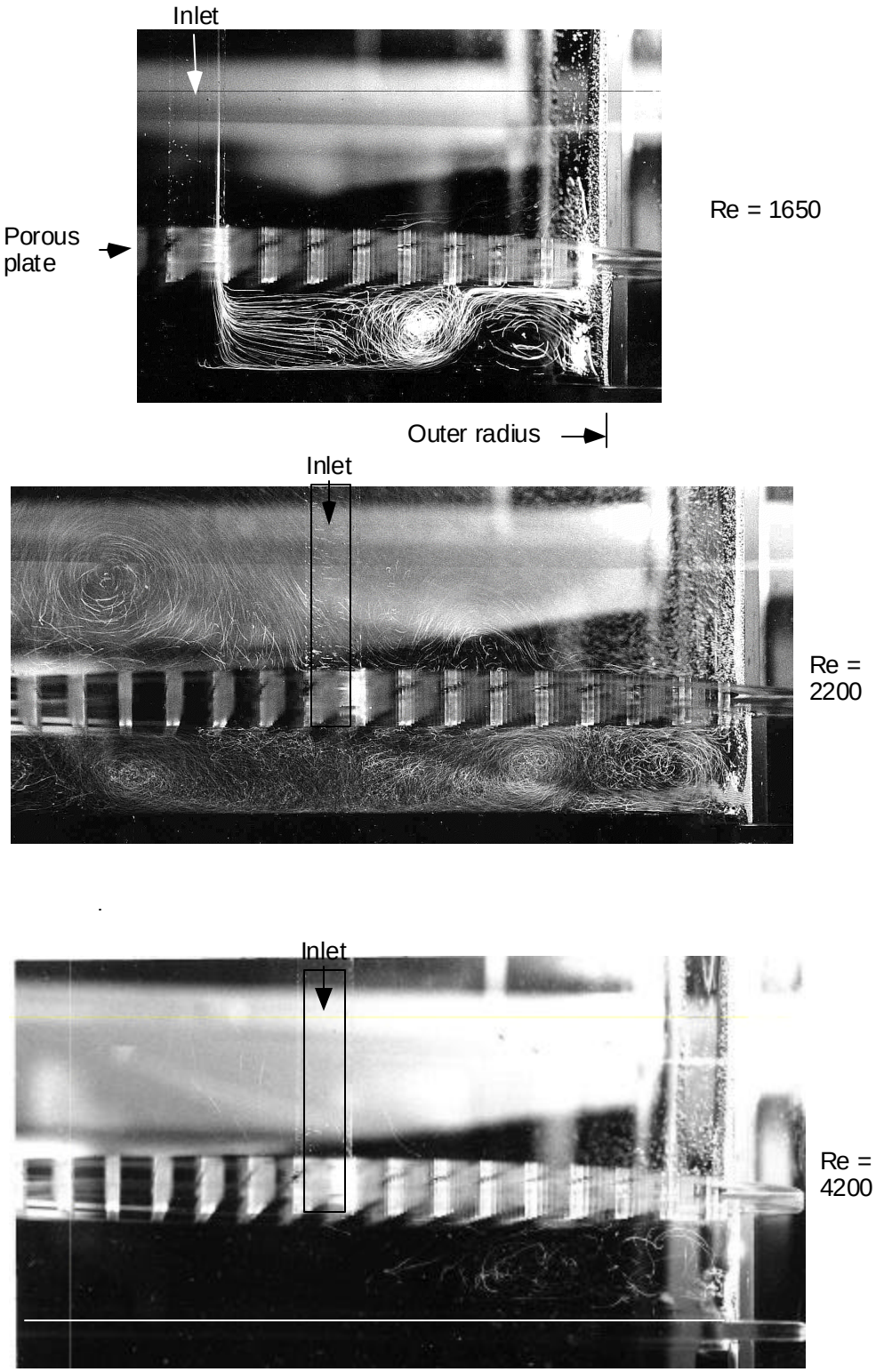

Figure 40. Eddy structure visualized in plenum region of 0.6-scale model.

Flow visualization in the oil flow apparatus clearly shows a double vortex structure for inlet tube Reynolds numbers less than approximately 2,100. The double vortex structure is shown in the photograph for Re ≈ 1650 in Figure 40. The eddy structure changes from a double structure to a single vortex between Re ≈ 2100 and Re ≈ 2300. This transition is characterized by flow which oscillates non-periodically from a double vortex structure to a single vortex structure. The photograph for Re ≈ 2200 shows part of the wall jet flow recirculating in an inner vortex and part of the flow proceeding along the wall to the outer vortex. The photograph for Re ≈ 4200 shows a single vortex structure.

The flow visualization experiments conducted in the oil flow apparatus implied that a similar transition in eddy structure should exist in the water flow apparatus, but at a higher Reynolds number. Without simulated fuel elements downstream of the perforated plate, the transition occurred at Re ≈ 2900-3200. However, with the simulated fuel elements in place, the double eddy structure was observed for all inlet flow rates up to Re ≈ 4500, the maximum achievable in the apparatus. It is concluded that the presence of the simulated fuel elements could have induced the wall jet flow to separate from the wall and form the double eddy structure. However, time (and funding available) did not permit conducting comparable experiments in the oil flow apparatus with simulated fuel elements installed. The effects of these changes in plenum flow pattern on convective mass transfer with the fuel elements remains unclear.

Effect of perforated plate

Holes in the perforated bottom plates of typical basket designs have length-to-diameter ratios (L/D_{hole}) of about 0.5 to 5. Conceptually, one could attempt to estimate the effects of such plates on the mean flow magnitude and direction plus the turbulence components by applying the method of Taylor and Batchelor [1949] who considered gauze screens. However, it is not clear whether their approach would be valid for perforated plates with L/D_{hole} greater than the order of one. In the present experiment, $L/D_{hole} \approx 3.2$ which is an intermediate value for typical designs of canister baskets.

In the plenum region upstream of the perforated plate, the radial velocity component is generally greater than the axial component, except in the recirculating eddy, and the fluctuating radial component is much greater than the axial counterpart. As shown in Figure 37 one set of measurements was obtained downstream of the hole, essentially at the entrance of the basket which would carry an array of fuel rods. In the radial direction these data were taken at the same location as the holes but in the spanwise or circumferential direction they were offset slightly. The locus of the hole centers was along y ≈ 7.5 mm and the data were taken at y ≈ 10.95 mm. The axial location was about 6.5 mm downstream of the plate. Thus, relative to the holes the measurements were at about 1.7 diameters from their outlets and at a radius of about 0.9 diameters. We believe these locations would have provided data characteristic of the expanding jets from the holes at their outer edges.

If the flow through the holes were uniform, the average bulk velocity $V_{b,hole,avg}$ would have been about 0.16 m/sec, giving a hole Reynolds number of about forty. These limited downstream data give $0.136 < U < 0.166$ m/sec or a ten percent variation. The lower values were near the center of the simulated canister. As one sees from Figure 37, the flow is predominantly parallel to the axis of the canister. The radial mean velocity was about one percent of the axial component (or less)

except near the hole nearest the center (about twelve percent there). Relative to $V_{b,hole,avg}$, the rms axial fluctuations were about 3 to 7 percent and the radial ones were about 0.5 to 1 percent. In absolute values, upstream of the plate the radial fluctuations ranged from about 0.09 to 0.18 m/sec and in the jets downstream the range was about 0.0008 to 0.002 m/sec, a reduction of about two orders-of-magnitude in the radial fluctuations. The reduction for the axial fluctuations was approximately a factor of four.

The apparent effects of the perforated plate at these conditions is to convert the predominantly radial mean flow in the plenum region to an axial flow and to reduce turbulence substantially. Since the turbulence of the jets provides the initial freestream turbulence relative to fuel elements it is likely that there would be a substantial effect on the convective mass transfer (drying or passivation) of the elements. However, it would be a mistake to generalize this observation to other conditions. Taylor and Batchelor [1949] show the effects vary with grid resistance which, in turn, varies with both the hole configuration and Re_{hole}. Additional measurements are desirable, both with the present model and with other conditions.

6. NUMERICAL MODELS OF FLOW IN THE SNF CANISTER

The intent of the computational modeling work was to assess the ability of industrial computational fluid dynamics codes to predict complex flows. These codes are readily available and used for flow predictions throughout the DOE complex. The models were initially used as is, then modified as needed to properly predict flow with representative fuel storage containers.

A number of phenomena exist within the apparatus that need to be examined to determine their importance in the overall mass transfer to the surface of the fuel rods (see Figure 41). The ultimate goal of the type of system being analyzed is to oxidize any exposed fuel on the fuel rods. In this situation, the rate at which oxygen is transferred to the surface of the rods is important. The phenomena that will impact this mass transfer include the turbulence levels within the pipe prior to impinging on the plate, the jet impingement, flow between the porous plate and canister bottom, flow through the porous plate (holes), and the flow up past the fuel rods themselves. Each of these phenomena has been analyzed with computational tools.

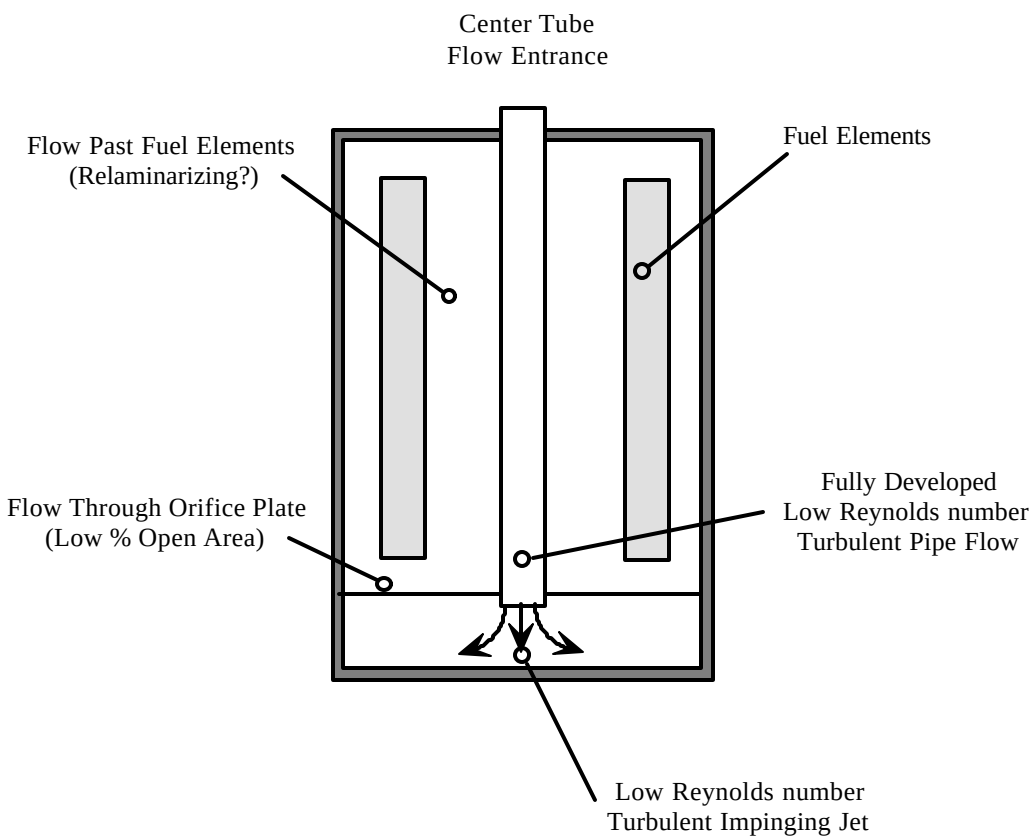

Figure 41. Different flow regions that are of interest to the development of the numerical models.

The flow through the orifice plate poses the greatest uncertainty for the modeling efforts. It also presents the greatest challenge in modeling the complete system. The size and spacing of the holes are not small relative to the size of the plate itself. This will result in the modeling complexities because the flow through each hole needs to be included in the model to properly assess flow distribution. Including

each individual hole will increase the number of elements required to mesh the complete geometry and increase computational times.

Several modeling activities were conducted to assess the slow situation in the simulated flow system. The modeling activities included low Reynolds number modeling of the inlet pipe flow, two-dimensional flow modeling of the impinging jet onto the bottom of a cylinder, three-dimensional modeling of general flow patterns into the symmetry section without the porous plate, and three-dimensional modeling of flow in the symmetry section with the porous plate.

The initial round of modeling qualitatively assessed the flow patterns in support of the experimental effort and to work towards validation of the modeling approach. The models progressed from the most basic to a complex model of the complete three-dimensional geometry. All modeling results were completed with the general-purpose finite element code FIDAP™. The results of the scoping calculations will not be presented here because they were conducted to support the design of the experiments and were intended to give "order of magnitude" guidance to the experimentalists.

The remainder of the numerical modeling report will include analysis of the turbulent flow in a long pipe, turbulent flow in the inlet section to the experimental apparatus, the impinging jet region, three-dimensional flow into a container without a plate, and three-dimensional flow within the complete system, including the porous plate.

Pipe Flow

The entrance to the flow geometry is a long pipe down the center of the apparatus. To accurately predict the flow entering the plenum region of the apparatus, the exit conditions of the pipe have to be predicted correctly. The Re of the flow in the pipe will be in the low Re turbulence range (Re • 2500).

Numerous models are available to model turbulent flows. The majority of these models are for higher Re flows. These models include k-epsilon, k-omega, renormalized group (RNG) model, eddy-viscosity, and others. There are fewer models, or variations of models for low Re flows. Within FIDAP, the k-omega model is very robust and models the viscous sublayer, rather than approximating the flow within this region. See Wilcox [1994] for details on a number of the more common turbulence models.

The low Reynolds number pipe flow was modeled axisymmetrically. The non-dimensional diameter of the pipe was assumed to be 1, and the length of the pipe was set to be 240. The large L/D ratio was used to ensure the results would be representative of fully developed flow. The experimental data to which the results are compared was taken from Reynolds [1969]. The inlet velocity and fluid viscosity were set to ensure Re = 3017 was obtained for the model.

Figure 42 shows a comparison of the non-dimensional velocity profile (U^+) for experimental and numerical data. In addition, a comparison of the velocity profile is also made. The best results are shown between the k-ω model and the experimental data. The ability to integrate through the boundary layer (better job of modeling the viscous sublayer region) leads to the improved results.

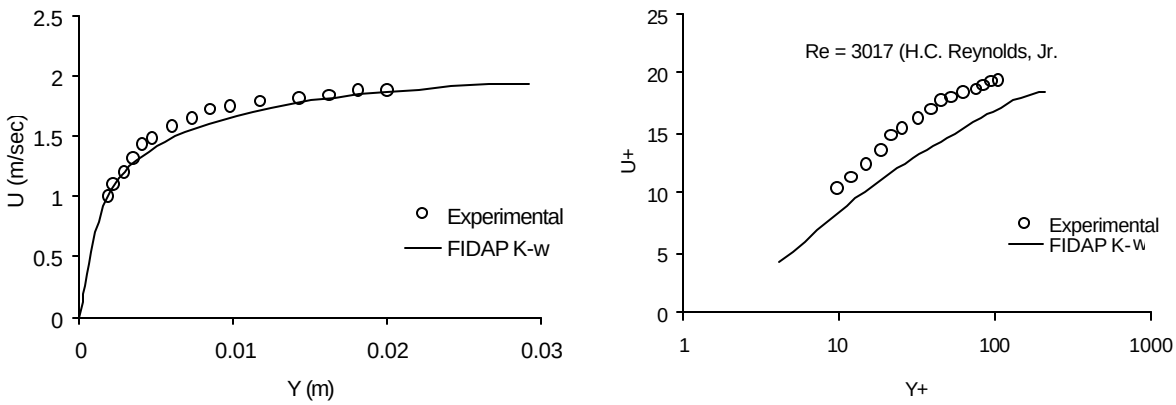

Figure 42. Comparisons between Low Re data and numerical predictions made by FIDAP (Re=3017, fully developed flow L/D = 240). The left hand side compares the measured and predicted velocity profiles, while the right hand side compares the non-dimensional velocity profile hear the wall.

The implementation of the k-ω model within FIDAP is the only potential turbulence model for low Re flows. The most common turbulence models are all designed for high Re flows (on the order of 10^5). The k-ω model is for much lower Re number flows and rather than model the viscous sublayer, adequate mesh must be used to actually capture the changes that occur very close to the wall of the computational domain.

The implementation used within FIDAP is traditionally suited for slightly higher Re than those modeled here. Overall though, the comparisons are adequate for the types of trends trying to be predicted with the present models. Some of the differences shown in the non-dimensional curves could be due to the numerically estimated wall shear stress, which is needed to non-dimensionalize the velocity. The velocity profile is in good agreement and the agreement between the two can be considered adequate for industrial type simulations.

Inlet Pipe Flow Model

The second type of pipe flow simulations considered a geometry similar to one used in the experiments. The experimental apparatus consisted of two different diameter pipes. A larger diameter pipe was used for the entrance flow, which was then connected to a smaller diameter pipe. A schematic of the geometry is shown in Figure 43.

Figure 44 shows a comparison between the measured and predicted data for the exit of the inlet apparatus for a Re of 3500. In general, there is a fair agreement between the predicted and measured data. Estimates of the wall shear stress and experimental uncertainties could account for some of the differences between the model and experimentally data points. In addition, a more refined low Re turbulence model could have improved the agreements as well.

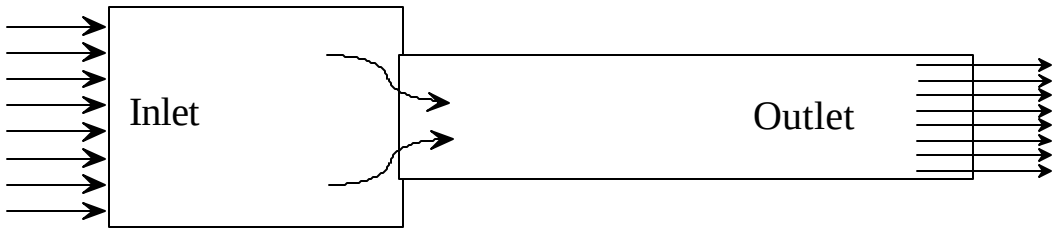

Figure 43. Schematic of inlet pipe flow geometry for experimental apparatus.

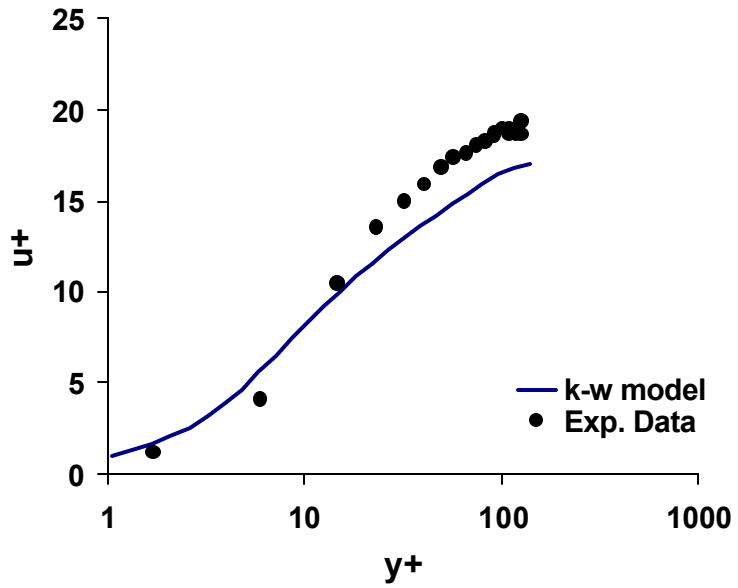

Figure 44. Comparison between measured low-Re pipe flow data and the numerical predictions of FIDAP's k-omega model at a Re = 3500. Experimental data obtained by D. McEligot and G. McCreery at the INEEL.

Modeling of Impinging Jet in 2D Geometry

Several standard turbulence models were used to analyze the flow out of the pipe onto the lower plate. The intent of this work was to examine the sensitivity of the jet spreading to the type of numerical model used (turbulence model and upwinding scheme). In addition, the length of the pipe in the model was varied to demonstrate the sensitivity of the results to this parameter as well. The geometry consisted of a long inlet pipe and the plenum region (porous outflow boundary condition selected). Flow entered the pipe, impinged on the lower plate and then exited the computational domain through a “porous” support plate.

The “porous” support plate approach is the only way to model this complex three-dimensional geometry in an axisymmetric simulation. The porous support plate approach allows for a pressure drop to be associated with the outlet boundary of the computational domain. This type of boundary

condition would be good for meshes or screens where the hole size is small relative to the problem geometry. A schematic of the system is shown in Figure 45.

The model was developed to allow for easy variation of the length of the inlet pipe. This would help assess how sensitive the outlet velocity profile was to pipe inlet conditions and length. An axisymmetric model for the pipe and plenum region was.

The turbulence models included k-ω, standard k-ε, and the RNG version of the k-ε model. Additional models were used to show the severe limitations of these models. These models are standard within FIDAP™. The k-ω model is integrated through the viscous sublayer, whereas all of the other techniques rely on a wall function approach. The wall function approach is not particularly suited for low Re flow because of the nature of the assumptions used near the wall.

Figure 46 shows representative modeling results for this jet impingement region. The turbulence models used included the standard k-ε, RNG k-ε, and the k-ω model. Figure 46 shows how widely the results varied for different models and numerical schemes.

U_z represents the flow along the direction of the pipe. It is not surprising that the results vary for the different models, but it was not expected that such a huge variation would exist. The axial velocity (U_z) varied by a factor of 3 for the different models. The radial velocity components (lower portion of Figure 46) also varied by a factor of 3. It is readily apparent that the type of model and numerical scheme selected will impact the predicted flow field. As discussed previously, the k-ω is specifically designed for low Re flows and it also gave reasonable agreement with the measured pipe data of Reynolds.

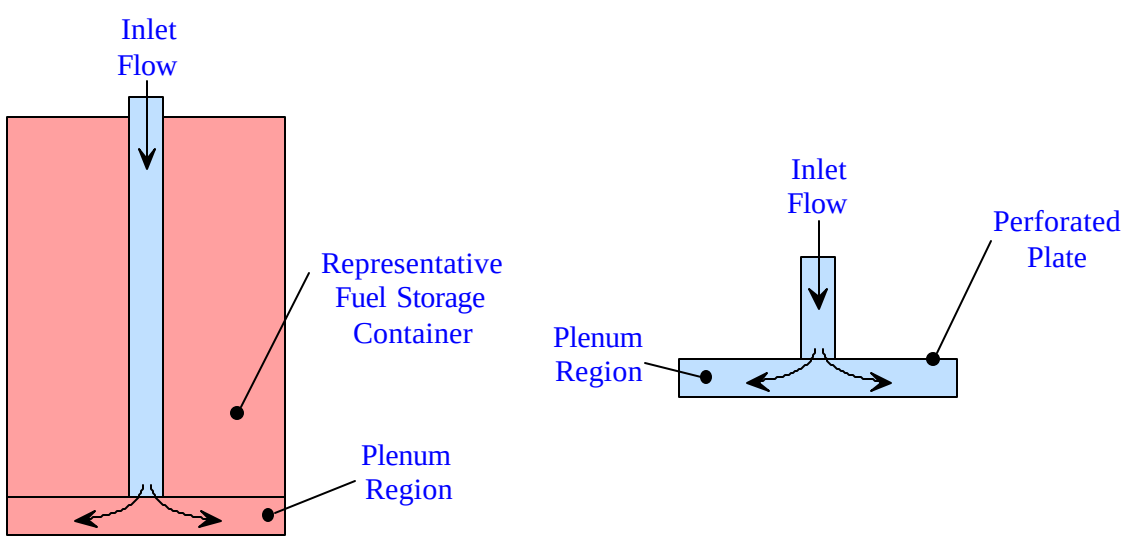

Figure 45. Schematic of impinging jet model. The porous plate boundary replaces the perforated plate that exists in the full model. System is used to examine expansion and impingement of jet onto lower plate. Distance from pipe to lower plate was 2 inlet pipe diameters.

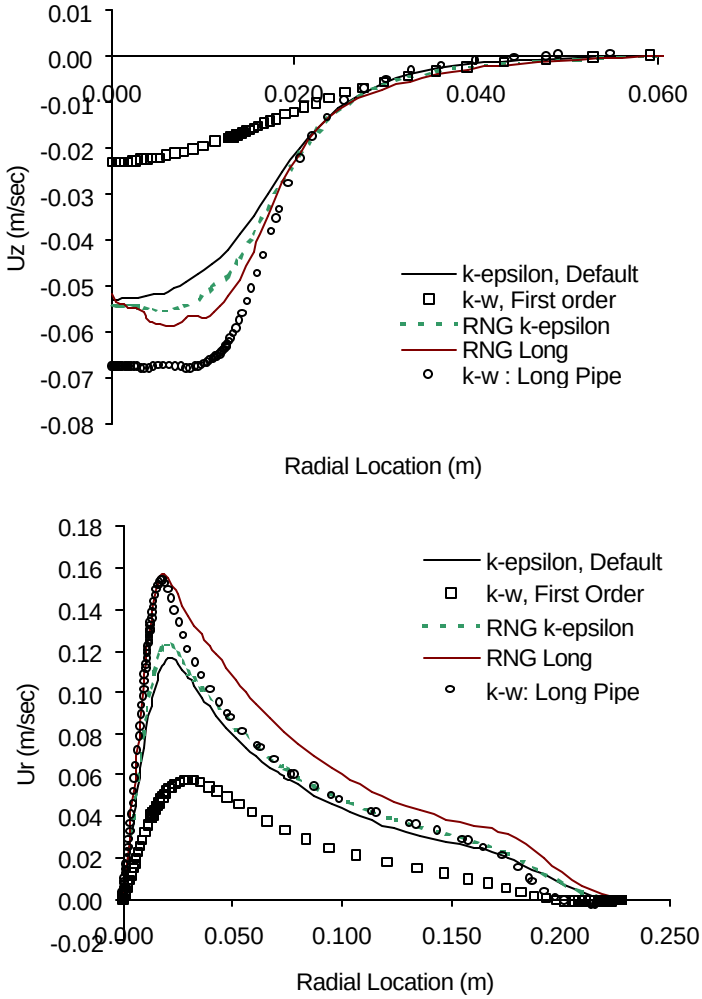

Figure 46. Comparison of different turbulence models and numerical solution schemes for flow impinging on lower plate of system. "First Order" refers to the type of upwinding scheme used for convective terms. Models used include standard k-ε, RNG k-ε, and the k-ω model.

Figure 47 shows the spread of the impinging jet as the flow moves out radially from the centerline of the pipe. The k-ω model was used for these results because of the favorable results presented for low Re pipe flow. All of these results show the proper qualitative trends for impinging jet flow onto a plate. The jet impinges on the plate, the flow spreads rapidly, increasing the speed of the flow along the bottom plate (often referred to as a "wall" jet). The flow accelerates, entrains other fluid (allowed to enter back into the flow domain through the porous plate outflow boundary condition), and then peak velocity starts to slow as the "jet" spreads and entrains other fluid.

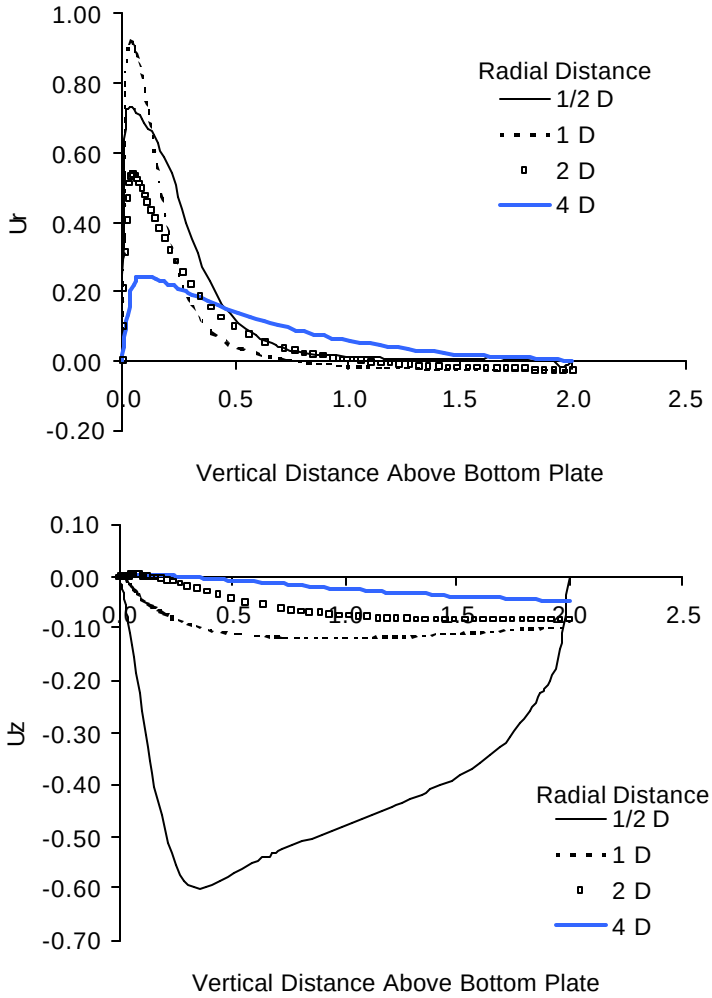

Figure 47. Vertical velocity profiles located at the indicated radial position from centerline of pipe (Re = 5,000, k-ω model, long inlet pipe).

The impinging velocity vectors are shown in Figure 48. The low Re flow exits the pipe, spreads, impinges on the plate, and then spreads over the bottom plate of the canister. These vectors are the result of a k-ω simulation with the porous plate outflow condition. The re-entrant characteristic of the flow is also shown in the lower section of Figure 48.

More simulations were also conducted to examine the impact of the porous plate on the flow in the storage container. These simulations assumed the full geometry, laminar flow, and no porous plate. These tests were to be used in conjunction with the three-dimensional simulations to better understand the impact the plate has on the flow.

The experimental results previously discussed in this report did examine flow in a more open plate structure. This open plate structure was shown to allow flow to recirculate back into the plenum region. The porous plate modeling approach used for Figure 48, show a similar flow characteristic.

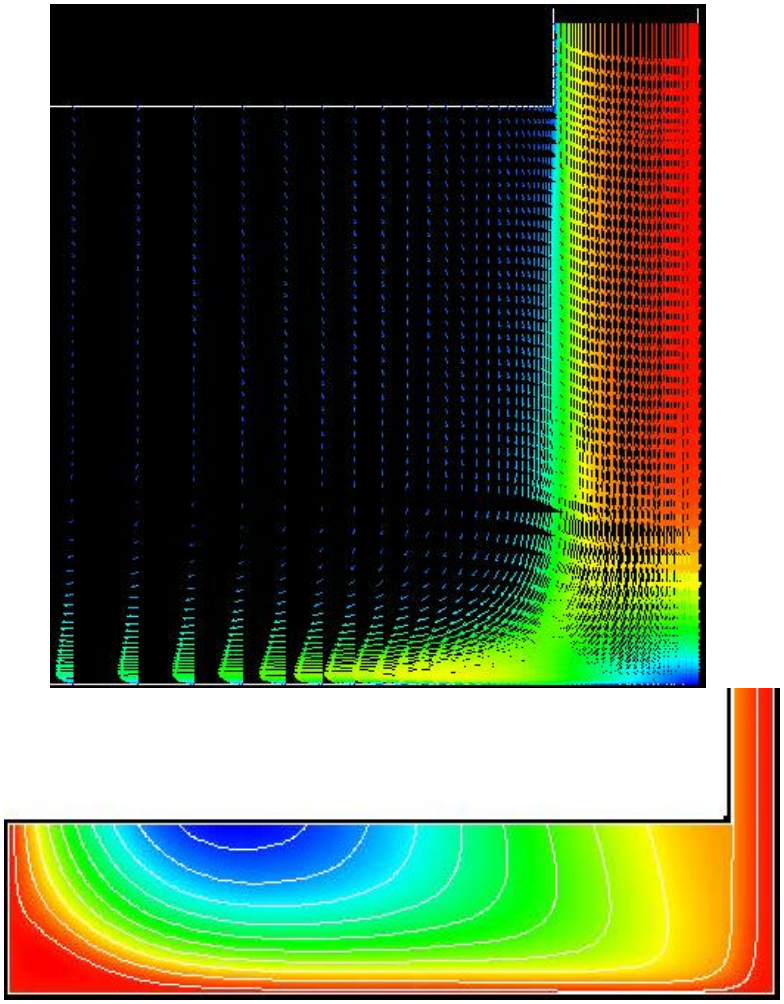

Figure 48. Flow impinging onto bottom plate. Top: High velocity vectors are colored red, low velocity vectors are colored blue. Note “boundary layer” characteristic along the bottom of the plate as the flow spreads out over the plate. Only a portion of the plenum region is shown. Bottom: Streamlines of flow in plenum region (re-entrant flow).

Figure 49 shows streamlines for a model that did not consider a porous plate in the geometry. These simulations considered laminar flow and removed a porous plate just above the plenum region. The results show the formation of a recirculation zone near the bottom of the canister. Qualitatively, these results show recirculating flow patterns similar to those of a porous plate (holes much smaller than geometry features).

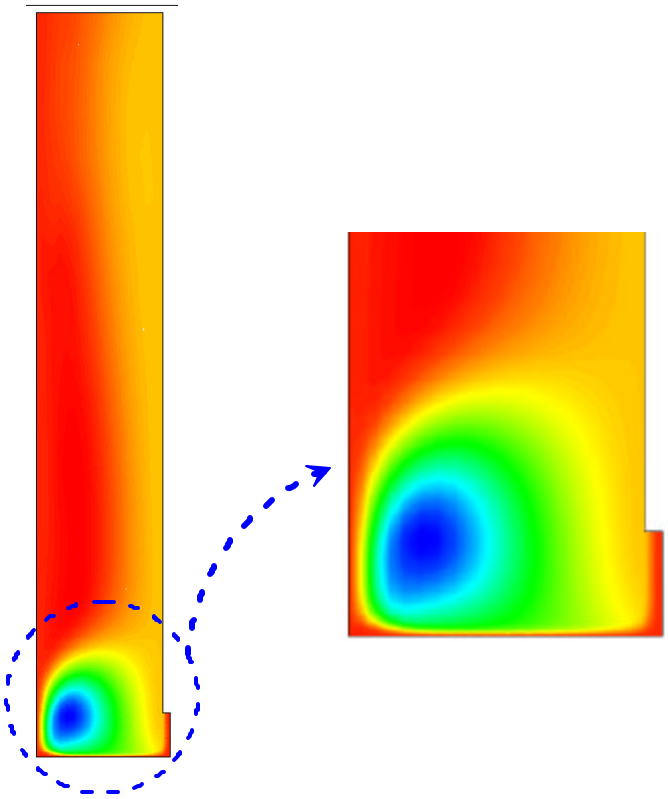

Figure 49. Flow recirculation in “open geometry” (laminar flow). Results here show how flow would recirculate in a system that did not have a porous plate to distribute the flow more evenly into the fuel storage region.

Three Dimensional Geometry without Plate

The first three-dimensional model developed only considered flow out of the pipe, impingement on the lower plate, and flow up past the representative fuel rod. Figure 50 shows the representative symmetry section and a detailed few of the mesh at the lower regions of the geometry (semicircular cut out represents fuel rod). These laminar flow predictions were conducted to later make comparisons with the three-dimensional predictions that contain the porous plate (see next section). Comparing these results would allow a qualitative analysis of the impact of the porous plate on the flow within the apparatus. The general flow characteristics could also be analyzed with this type of model.

Figures 50-52 show the geometry and typical laminar flow results. Symmetry planes were used through the middle of the fuel element and at the plane ½ way between the fuel elements. This model did not include the porous plate as mentioned above. The model consisted of roughly 80,000 elements. Flow exited the pipe, impinged on the bottom plate, flowed past the fuel element, and out the top of the domain. The intent of these simulations was purely qualitative.

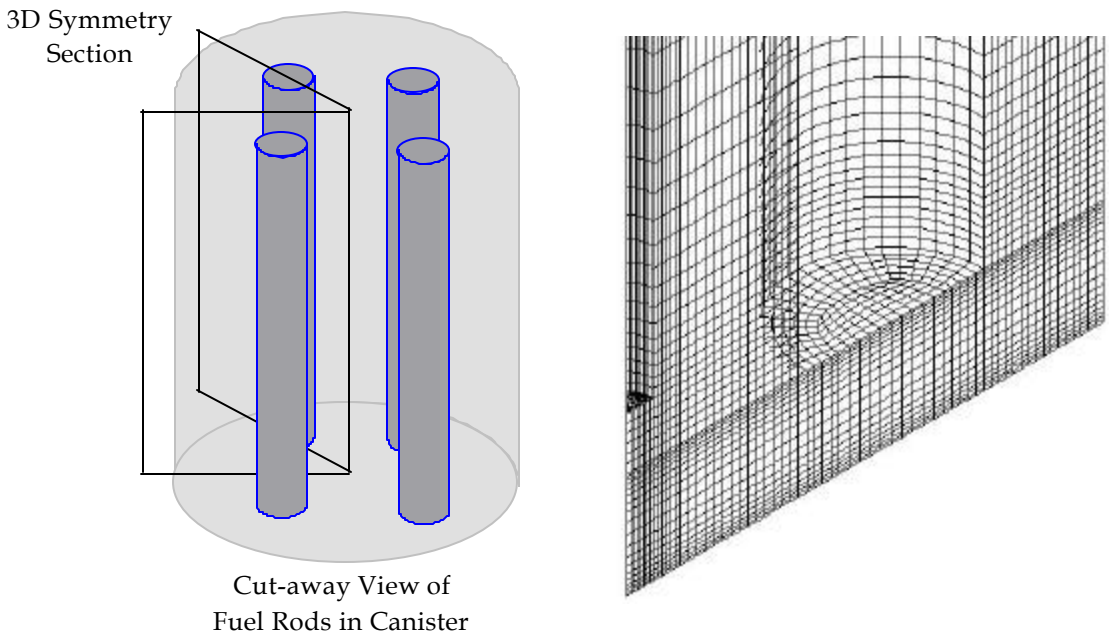

Figure 50. Schematic of symmetry section and mesh near pipe outlet and representative fuel element.

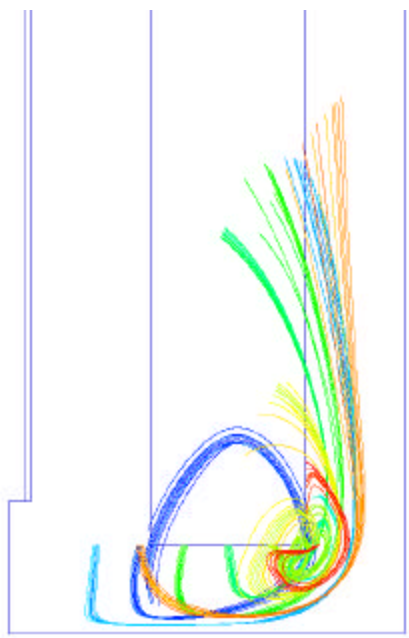

Figure 51. Flow recirculation viewed from the symmetry plane through the representative fuel element. (Laminar flow with no porous plate included in the model).

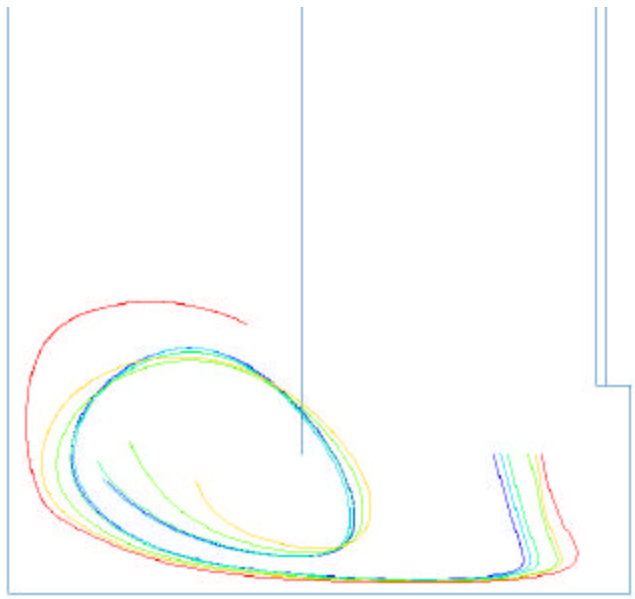

Figure 52. Flow recirculation pattern on symmetry plane between fuel rods. Flow characteristic is qualitatively similar to conditions shown in 2D simulations (see Figure 49).

Qualitative comparisons between the two-dimensional results shown in Figure 49 and those of Figures 51 and 52 show a recirculating flow. Particle traces are shown for particles introduced near the fuel element (Figure 51) and near the symmetry plane (Figure 52). In general, the recirculating characteristic of the flowfield found in Figure 49 agrees with what is shown in Figures 51 and 52. The flow, if not impeded by a porous plate, will recirculate in the lower regions of the canister, and then flow up past the fuel element.

Three Dimensional Geometry with Plate

The complete geometry was modeled next. A 1/8th symmetry section was selected for meshing. The definition of the mesh was one of the most important features of this modeling effort. Trade-offs between boundary layer mesh refinements, total mesh, and mesh aspect ratios had to be weighed in order to insure the numerical solution would converge and that the flow field would be adequately resolved. A significant amount of time was spent on refining the finite element mesh for this particular geometry.

Figure 53 shows a top view of the three-dimensional symmetry section. These simulations differ from those previously discussed because the model includes the details of the porous plate. The holes are on 1 inch centers and ¼ inch in diameter through a ¼ inch plate. A preliminary mesh consisted of over 320,000 elements. Elements were compressed above and below the porous plate to capture changes in the flow field as it enters and leaves each of the holes in the plate. The mesh was later refined and contained over 714,000 elements. Figures 54 and 55 show the final mesh for the simulations. Convergence of the problem was found to be very sensitive to the aspect ratio of the elements. This was due to the fact that the flow recirculates above as well as below the plate. Without a fine mesh, these flow features would not be detected and caused convergence problems.

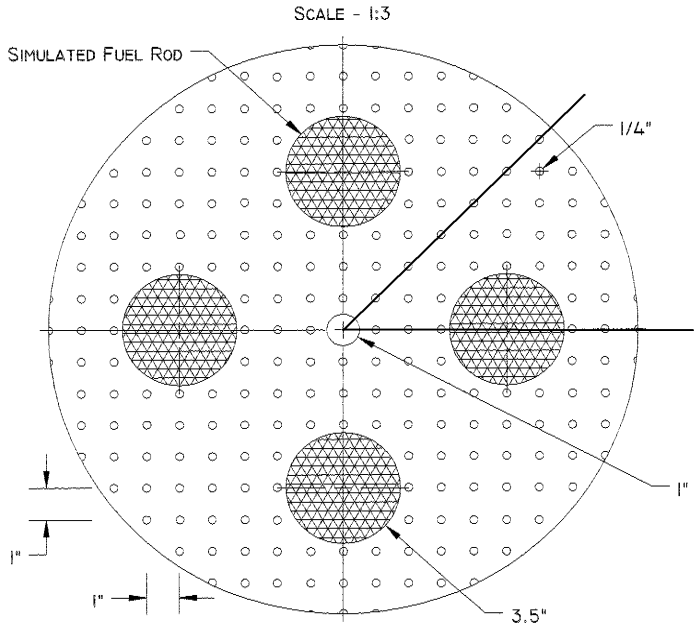

Figure 53. Top view of 3D geometry. Simulated fuel rods are shown above the plate surface. Holes are on 1-inch center to center spacing. Plate is ¼ inch thick with ¼ inch holes through the plate.

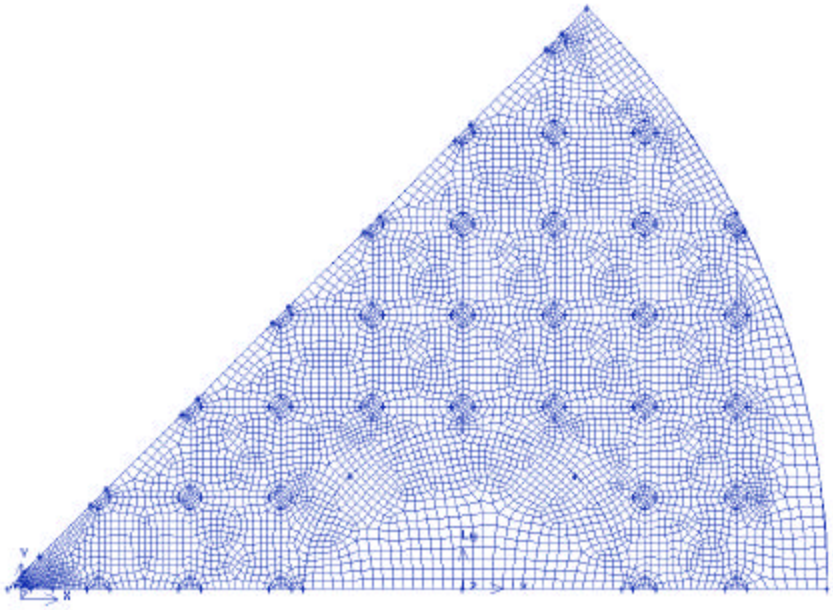

Figure 54. Top view of three-dimensional symmetry section. Holes are shown with localized mesh arranged to capture flow through holes. Large half circle is the representative fuel rod. Mesh is compressed near flow inlet (lower left) to properly resolve the flow impinging on the bottom plate.

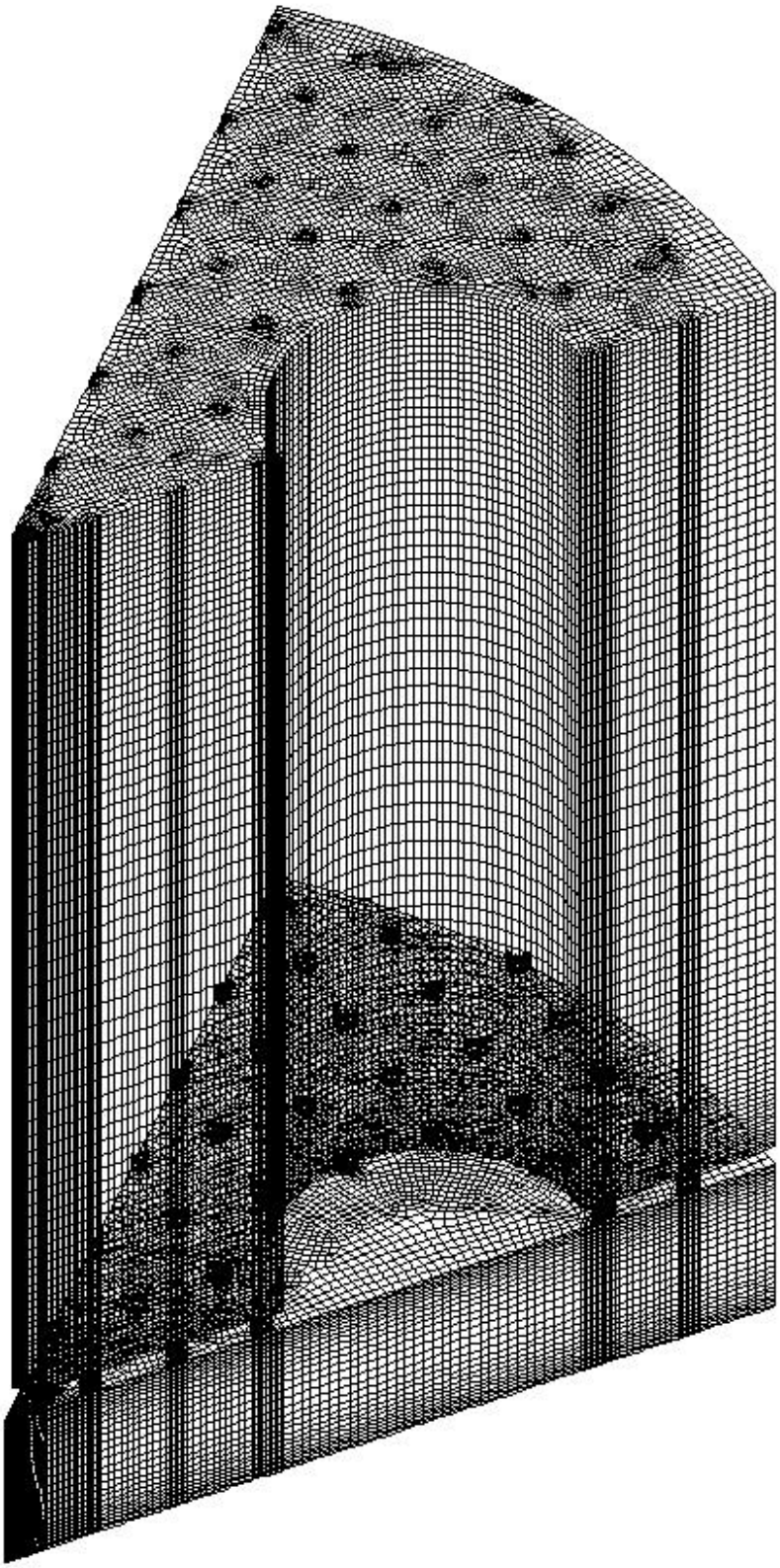

Figure 55. Side view of the geometry and mesh.

Figure 56 shows the flow impinging on the lower plate as it exits the pipe. The flow forms a small recirculation zone near the jet, the location of which is dependent on the Re of the pipe flow.

The model only considered the region below the plate and a portion of the fuel storage region above the plate. The main interest was in how the flow went through the porous plate. The results presented here considered laminar flow, not low Reynolds number turbulent flow conditions. In addition, the model did not consider the developing flow in the entrance pipe. The inlet boundary condition assumed fully-developed laminar flow prior to impinging on the plate.

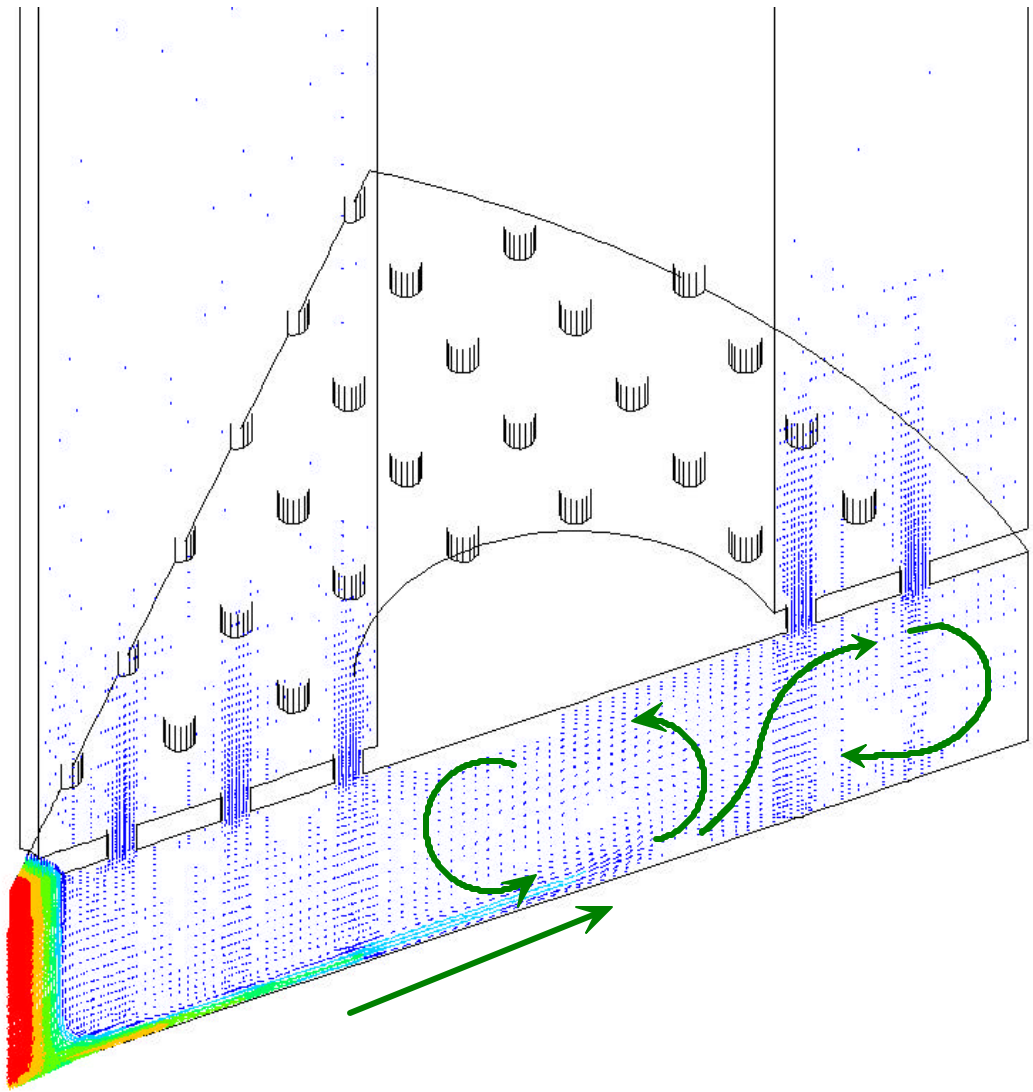

Figure 56. Side view of the 3D flowfield leaving the pipe region and entering the plenum region of the container. Model contained over 700,000 elements. Recirculation zones form in plenum region and more uniform flow occurs up past fuel element.

Figure 57 shows a comparison between the experimental results and the numerical model. The results only compare the general flow structure below the plate. The general location of the recirculation zones are in agreement. The flow leaves the entrance pipe and impinges on the bottom plate. The flow spreads out, forms 2 recirculation zones, and flows up through the porous plate. An examination of the flow in a plane parallel to the bottom plate shows a number of recirculation zones in this plane, indicating the complex nature of the flow up through the plate and past the fuel rod.

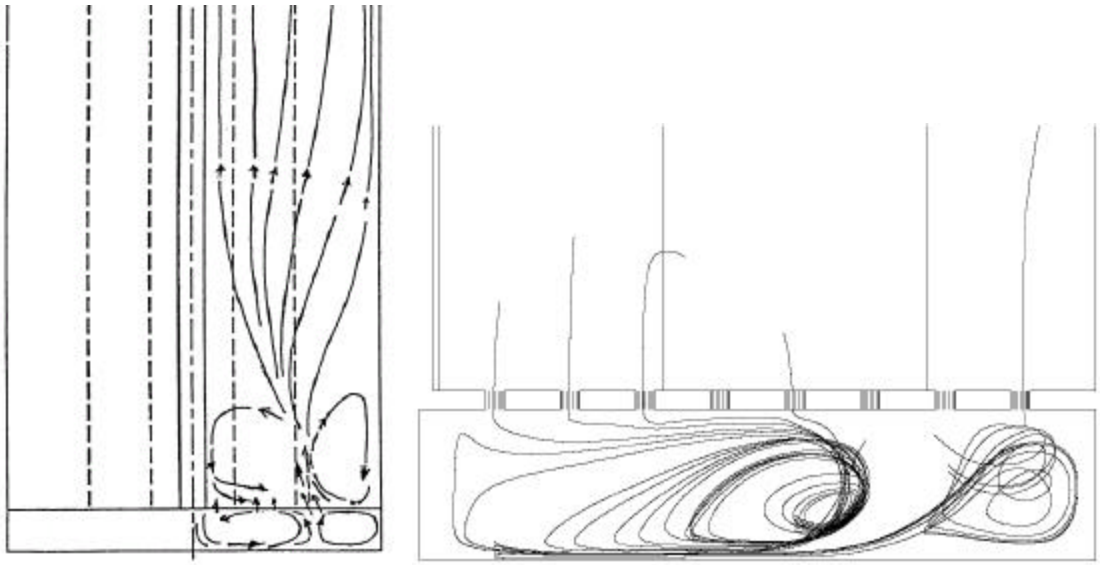

Figure 57. Qualitative comparison of flow structures below plate. Left-hand side shows the experimental results and the right hand side shows the numerical results. (Re = 2500, S/D = 2, Porosity of 4%).

7. CONCLUSIONS AND RECOMMENDATIONS

Conclusions

Our research group has developed experimental and computational results to develop reliable predictive techniques for the energy, mass and momentum transfer plus chemical reactions in drying, passivation and transfer of spent nuclear fuel from wet to dry storage. An idealized SNF canister was defined to investigate fluid flow associated with drying and passivation. The canister configuration includes flow phenomena that occur in canisters for high-enrichment and medium-enrichment fuels, where fuel element spacing in the canister is increased as compared with low enrichment fuel. The canister diameter was taken as 46 cm (18 in.) and a single basket of about 1.3 meters (4 ft.) length was considered. A long central tube served as the inlet as in one earlier concept for a passivation process. While this concept apparently has not yet been selected for application, it provides an excellent example of the coupled, complex phenomena which may be present in canister flows. Suggested design flow rates for this hypothesized application indicate that the Reynolds number in the inlet tube would be expected to be between 2500 and 5000, i.e., relatively low.

A unique flow-visualization method was developed to simulate a passivation reaction between oxygen gas and uranium hydrides found on wet-stored spent nuclear fuel elements. Using hexanoic acid as a working fluid and sodium metal to simulate a corroded area on an SNF element, we were able to visualize the effect that the reaction will have on the surrounding flow. The research showed that the reaction between the acid and the sodium produced a localized concentration of bubbles, which rose in the flow, causing various disturbances.

Although the hexanoic acid-sodium metal reaction produces hydrogen bubbles in a two-phase flow, and the passivation reaction is strictly single phase, some valuable fluids insight were obtained. During the passivation treatment, hydrogen is liberated as a byproduct of the reaction. The hydrogen is buoyant compared to the surroundings, and will therefore begin to rise. This behavior is similar to a buoyant plume that is observed in open fires. One aspect that makes our scenario different is that it is a buoyant plume in a crossflow. The rising hydrogen entrains the surrounding gases, slightly enhancing the mixing. The entrainment also causes the fluid in the freestream to convect towards the reaction, thereby “feeding” the downstream reaction areas.

The buoyant reaction product combined with the fluid in crossflow produced a billowing instability that affected the surrounding flow field. These instabilities can couple with the instabilities that occur throughout the flow in the canister to produce complex flow patterns. We also performed experiments with multiple reaction sites on the surface, including a series of in-line and staggered reaction sites. In addition to increasing the flow complexity, additional reaction sites serving to enhance the mixing of the fluids.

A water-flow experiment with a 3/4-scale model (relative to the idealized canister) has been used for overall flow visualization and velocity measurements, with and without an array of simulated fuel elements. Its purposes were to obtain initial indications of the gross flow behavior and to investigate the circumferential periodicity of the flow. Standard flow visualization techniques, using fluorescent dyes and neutrally buoyant particles illuminated by laser and white light, were employed. Observations have been made with perforated plates (representing basket

support plates) having three different hole geometries, with and without simulated fuel elements. The flow patterns exhibited are very complex and provide a non-uniform flow distribution along the simulated fuel elements.

Experiments were conducted to determine the canister flow field with three perforated plates with open areas of 50%, 8% and 4% . Experiments reported are for $Re_{inlet} = 2{,}500 \pm 100$. Although laminar flow in a smooth tube can occur at Reynolds number as high as approximately 40,000, it is believed that the tube is sufficiently long and the entrance conditions sufficiently abrupt to insure that turbulent flow exits the tube and impinges on the plate. The flow is approximately circumferentially periodic and symmetrical about cross-sections through the four outer tubes for experiments using each of the three perforated plates. This observation implies that numerical predictions and detailed measurements can concentrate on an 1/8-th sector of the idealized geometry rather than the full cross section.

With a 50% open area plate, the flow pattern is comparable to that of a submerged impinging jet on a semi-infinite plate with formation of a large vortex and entrainment and recirculation through the holes in the perforated plate near the center. Downstream flow is primarily through the outer holes. A single main recirculating eddy forms, encompassing the plenum and part of the region for the element array.

With the 4% and 8% open area plates, recirculation regions occur downstream of the perforated plate and two main recirculation zones (plus a small corner flow vortex) form upstream of the perforated plate. Flow does not reenter the inlet plenum through the smaller open area plates as it does with the 50% open area plate. In these cases the flow pattern in the inlet plenum has some features of a confined impinging jet [Morris and Garimella, 1996].

The Reynolds number in the array downstream of the plate based on hydraulic diameter is approximately 70 for $Re_{inlet} = 2{,}500$. With the tubes present, vortices persist for the majority of the tube bundle length and the flow only starts to approach a fully-developed laminar profile near the exit of the bundle ($L/D_h \approx 6$, where D_h is the hydraulic diameter). The flow distribution is uneven near the surface of the simulated fuel elements. Higher velocity is observed near the surface towards the canister centerline than towards the outside where, except near the perforated plate, the velocity is an order-of-magnitude lower. These experiments show flow across the simulated elements and resultant vortex shedding, although the vortices do not show the clear alternating pattern of a Karman vortex street [Tritton, 1977].

Velocity and turbulence distributions were measured with laser Doppler velocimetry in the INEEL Matched-Index-of-Refraction (MIR) flow system. A 0.6-scale model of the idealized canister was employed with dimensions as follows: plenum spacing $H/D = s/D = 2$, canister internal radius $r_0/D = 9$, pitch of holes in the perforated plate $p_h/D = 1$ and hole diameter $d_h/D = 1/4$ in a square pattern. Most measurements were taken at $Re_{inlet} = 2510$. Data were taken on flow in the inlet tube, the impinging jet and flow upstream of the perforated plate (inlet plenum). Flow at the exit of the inlet tube was determined to be one that was intermittently turbulent and laminar, i.e., undergoing axial transition. However, the mean velocity profile still had predominantly laminar character. Measurements included the mean distributions of radial and axial velocity components, V and U, and their root-mean-squared fluctuations, v' and u'. These data would be suitable for comparison to predictions from Reynolds stress models [Hanjalic, 1999] or k-ε-v^2 models.

Main features of the flow in the inlet plenum upstream of the perforated plate are the high velocity impinging jet, the thin expanding wall jet, a large recirculating eddy near the outer wall of the canister and relatively low velocities near the perforated plate. The flow in the wall jet remains attached until it impinges on the outer wall of the plenum region and induces the main recirculating eddy. Only a single major eddy is seen rather than the two observed with the water flow visualization. Outside the impinging and wall jets, flow is relatively quiescent with velocities about an order-of-magnitude less than the inlet velocity. In the plenum region upstream of the perforated plate, the radial velocity component at a point is generally greater than the axial component, except in the recirculating eddy.

The rms radial velocity fluctuations are generally considerably larger than the rms axial fluctuations. High values of v' are seen in the wall jet and moderate values mostly in its wake region or the half of the plenum near the wall jet. Moderate to high values also appear near the perforated plate in the region directly affected by the main recirculating eddy. Near the perforated plate in the range $0 < r/D < 7$, v' is still moderate while u' is low. For the most part, v' is the same order or larger than the mean radial V so the local turbulence intensities $v'/V\{r,x\}$ are of the order of 100 percent or greater, implying large turbulence levels. The large relative values of v' imply the likelihood that there are considerable fluctuations in the incident angle as the flow approaches the holes in the perforated plate. This situation differs significantly from flow conditioning applications of perforated plates in wind tunnels.

Comparison of the present results shows that flow in the plenum region upstream of the perforated basket support plate is sensitive to the inlet flow characteristics in the expected range of Reynolds number. What has not been determined is whether turbulent, laminar or transitional inlet flow is preferable for desired drying characteristics, or whether it matters. Further measurements are required to answer this question.

It is apparent from these experiments that, despite the conceptual simplicity of the canister design, the flow pattern is very complex. Of possible concern is the uneven flow distribution near the surface of the simulated fuel elements as demonstrated in the water flow visualization experiments. Higher velocity is observed near the element surface towards the canister centerline than towards the outside where, except near the perforated plate, the velocity is an order-of-magnitude lower. A more even flow distribution is expected to provide more uniform drying and passivation around the elements. Possible design changes that could provide more uniform distributions (if that is desirable) include (1) an optimized distribution of perforated plate holes, (2) a longer inlet plenum length (to decrease radial velocity tangent to the perforated plate which will presumably provide a more even flow distribution) and (3) a higher packing density of fuel elements, where criticality considerations allow. The canister and plate geometry could be optimized using a CFD code once it has been verified that the code can reasonably predict the present and other needed experiments.

Additional lessons learned for design of drying/passivation systems may be summarized as follows. Bypass flow routes should be avoided and flow distribution should be controlled. Assumptions of uniform flow could be very misleading. Previous measurements of flow through perforated plates for wind tunnel conditioning are not likely to be applicable to basket support

plates. Modifications of basket support plates and lower regions of canisters could be useful to distribute turbulent flow to the elements.

A number of different numerical models were developed to analyze the complex nature of flow in spent fuel canisters. Two- and three-dimensional models were developed to assess different flow features. It was found in general that the general-purpose code provided adequate results for the simulation of the low Reynolds number pipe flow. Agreement between the measured and predicted results was adequate, but refinements to the model could lead to improved comparisons.

Any of the modeling results that depended on “inlet” flow conditions to the plenum were found to be very sensitive to the assumptions made to the inlet pipe flow conditions. The selection of inlet boundary conditions is important to accurately predict turbulent flow conditions for these complex geometries. The modeling results are very sensitive to the type of turbulence model used for the simulations. Extremely large variations in the flowfield were noted for the different models. The most realistic results were obtained with a low Re turbulence model with accurate upwinding schemes. Low order upwinding schemes and poor assumptions for the inlet flow profiles lead to drastic changes in the results.

The method used to model the porous plate is critical in predicting the qualitative flow features within the system. The porous plate approach gave qualitative agreement to the experiments where a very open plate was used. But, in those situations where the plate was much more restrictive and relied on a lower open fraction (fewer and smaller holes), the porous plate approach predicted recirculation above and within the plenum region (re-entrant flow to the plenum). The actual experiments showed the flow recirculating below the plate, but not re-entering the plenum region through any of the holes. The three-dimensional models that took this into account qualitatively predicted the flow correctly.

Based on the present modeling, it appears necessary to include the details of the holes in the plate within the numerical model. It may be possible to develop a “porous plate” model for disperse holes, but model limitations may make it difficult to accurately model a wide range of design options. For example, if such a model “prevented” re-entrant flow into the plenum region, such a limitation may not detect situations where such flow truly exists. If a porous plate model were developed it would have to be developed with care to insure the proper physics are properly considered.

Numerical convergence is slow for the three-dimensional flow fields modeled. The order of magnitude changes in the velocity field across the computational domain make it difficult to obtain fast convergence. As the next generation of computing platforms is developed, it will be easier to include the necessary details to analyze the details of the flowfield. More uniform flow up past the fuel elements will be obtained through the use of a plate that restricts the flow and does not allow it to re-enter the plenum region. Detailed analyses and testing would have to be conducted to truly assess the uniform characteristic of the flow.

Recommendations

The present measurements have revealed complex flow patterns that are expected to be difficult to predict. In some regimes, predictions of flow patterns, velocities and turbulence levels would be

uncertain. Uncertainties in flow lead to uncertainties in convective mass transfer locally along fuel elements, leading further to uncertainties in drying (and passivation) rates locally.

Further work should concentrate on experiments examining the effects of a sparsely perforated plate on the turbulence field, both downstream and upstream, and the decay of turbulence fields in simulated fuel element arrays, both sparse (highly-enriched and moderately-enriched) and dense (low enrichment) plus related velocity fields.

Since suggested design flow rates for SNF storage/passivation applications indicate that the inlet Reynolds number would be expected to be between 2500 and 5000, the experiments should be conducted with inlet flow rates giving this range. The resulting Reynolds number in the fuel element array would be of the order of 100, giving strong potential for laminarization as the flow passes through the array. As shown in the present overall flow visualizations, continuous cross flow occurs in the array as the exit is approached.

Selection of models with simulated fuel elements (high-, moderate- or low -enrichment) would be conducted in coordination with technical representatives of the Spent Nuclear Fuel programs.

Additional measurements can be obtained by Particle Tracking Velocimetry (PTV) with the Moving Particle Tracking system (MPT) and by laser Doppler velocimetry (LDV). The MPT system would give additional possibilities and capabilities for quantitative 3-D flow visualization and measurements of particle fluxes and individual particle paths. The particle tracks would represent the motion of particular species in the flow. The MPT system could be employed to obtain quantitative flow field visualization in both the plenum and element array regions. In addition to the velocity field and particle flux fields, data could be reduced to examine individual particle tracks as suggested in the original proposal. This information can assist engineers in understanding variations of surface passivation through an array and approaches to modify designs to counter the non-uniformities and to improve distribution.

In order to simulate portions of the generic transport problem for an oxidizing component of a mixture, individual particles might be tracked from introduction via the central tube flow to multiple interactions with the array surfaces. New PTV techniques are being developed as part of the scope of parallel work in order to allow this individual particle tracking (IPT). Current PTV methods concentrate on small fields of view (e.g., 8 x 8 x 8 cm^3 [Kasagi and Matsunaga, 1995]). For IPT the field of view must track erratic particles in all three coordinate directions from the deduced instantaneous particle motion. The individual particle tracks and additional statistics are determined by analyzing off-line the motion of all particles that remain in the field of view as individual particles are tracked. The overall statistics for the particle transport would be derived from analysis of a large number of IPT records at the same inlet flow conditions.

Also the overall flow field would be examined quantitatively via flow visualization deduced from application of the MPT system. Equipment for the new MPT technique includes a PC-controlled camera system mounted on a longitudinal traversing system controlled by the same computer. Traversing can be programmed at variable speeds to about 15 cm/sec. The MPT system will be based on two 512 x 512 CCD cameras with framing rates of 60 fps with a C-mount lens. They will be mounted on a four foot linear traversing system with one tilting stage per camera. Illumination will be by a collimated beam strobe synchronized to the cameras. System control will be via P450-128MB computer systems and imaging will be by P450-128MB computer systems.

Control and imaging or data reduction programs are extensions of existing programs written in the C language with Windows user interface. When held in a fixed position the MPT method reverts to the successful PTV technique [Guezennec and Kiritis, 1990; Choi, Guezennec and Brodkey, 1992; Kent et al., 1993; Guezennec et al., 1994]. The flow visualization and related overall statistics will be derived from analysis of a large number of MPT records at the same inlet flow conditions. Typical results would include mean streamlines and velocity vectors plus qualitative turbulence quantities corresponding to and extending those measured with the LDV system. Attempts would also be made to obtain transient flow patterns, as in the wakes of the simulated fuel elements.

To supplement the velocity field data and particle tracks deduced via the MPT/PTV methods, measurement of instantaneous velocity components would continue by LDV at fixed positions, primarily in the array. Mean velocities and mean turbulence statistics would be determined from these time series. Thus, these results would give an Eulerian view while the new IPT method is a complementary lagrangian approach. The LDV is a two-component fiber-optics-based version mounted on a three-directional traversing mechanism. Since the traverse follows rectangular coordinates and the model geometry is circumferentially periodic, the LDV can be positioned to measure radial and longitudinal velocity components at one point and, by repositioning, circumferential and longitudinal components at an equivalent point in another region of the array. Typical results would include time-resolved, pointwise distributions of the mean velocities, U, V, W, and their Reynolds stress components. The time series would also be available for spectral and wavelet analysis [leWalle, Ashpis and Sohn, 1997; Resnikoff and Wells, 1998]. The upstream effect of the semi-confinement (by the basket support plate) on flow and turbulence fields in the plenum region would be examined via experiments varying the distance H/D between the perforated plate and the solid plate representing the bottom of a canister.

Additional parameters or phenomena which should be investigated systematically include the inlet Reynolds number and geometry, fuel rod loading, hole pattern and length in the basket support plate, positioning of the basket support plate (H/D). The results of such studies should provide new fundamental knowledge on the statistics of particle and passive scalar transport from lagrangian measurements in a rod bundle, the laminarization of turbulent flows entering an array of elements, in combined cross and longitudinal flow, and turbulence behavior in the surroundings of a semi-confined impinging jet.

8. REFERENCES

Becker, S., 2001. Advanced laser velocimetry technique. LSTM Erlangen, seminar presented at INEEL, August.

Becker, S., C. M. Stoots, K. G. Condie and D. M. McEligot, 1999. Reynolds stress development in the viscous layer of a transitional boundary layer. Proc., IUTAM Symposium on Laminar-Turbulent Transition, Sedona, Ariz., September.

Becker, S., C. M. Stoots, K. G. Condie, F. Durst and D. M. McEligot, 2002. LDA-measurements of transitional flows induced by a square rib. *J. Fluids Engineering*, in press.

Bendat, J. S., and A. G. Piersol, 1986. *Random data analysis and measurement procedures*. New York: John Wiley & Sons.

Calabrese, R. V., and S. Middleman, 1979. The dispersion of discrete particles in a turbulent flow field. *AIChE J.*, 25, No. 6, pp. 1025-1035.

Chambré, P.L. and A. Acrivos, "On Chemical Surface Reactions in Laminar Boundary Layer Flows," *J. Applied Physics*, November, 1956.

Choi, W.-C., Y. G. Guezennec and R. S. Brodkey, 1992. In situ calibration and stereo matching for 3-D particle image velocimetry. *Bull., Am. Physical Soc.*, 36.

Condie, K. G., Stoots, C. M., Becker, S., Alahyari, A. A., Durst, F., and McEligot, D. M., 1998. The structure of boundary layer transition induced by a square rib (A new large-scale MIR flow system for measurements of boundary layer transition). Tech. Report INEEL/EXT-98-01039, Idaho National Engineering and Environmental Laboratory.

Condie, K.G., McCreery, G.E., and McEligot, D.M., 2001. Measurements of Fundamental Fluid Physics of SNF Storage Canisters. Tech. Report INEEL/EXT-2001-1269, Idaho National Engineering and Environmental Laboratory.

Cook, N. H., and E. Rabinowicz, 1963. *Physical Measurement and Analysis*. Palo Alto: Addison-Wesley.

Cooper, D., D. C. Jackson, B. E. Launder and G. X. Liao, 1993. Impinging jet studies for turbulence model assessment - I. Flow-field experiments. *Int. J. Heat Mass Transfer*, 36, pp. 2675-2684.

Corino, E. R., and R. S. Brodkey, 1969. A visual observation of the wall region in turbulent flow. *J. Fluid Mech.*, 37, pp. 1-30.

Crepeau, J.C., and McIlroy, H.M., 2000. Flow visualization of a chemically reacting boundary layer, *Proc. IMECE 2000*, Orlando, Florida.

Cui, M. M., and R. J. Adrian, 1997. Refractive index matching and marking methods for highly concentrated solid-liquid flows. *Exp. Fluids*, 22, pp. 261-264.

Durst, F., J. Jovanovic and J. Sender, 1993. Detailed measurements of the near wall region of turbulent pipe flows. Proc., 9th Symp. Turb. Shear Flows, Kyoto, paper 2-2.

Durst, F., Keck, T., and Kleine, R., 1979. Turbulence quantities and Reynolds stress in pipe flow of polymer solutions measured by two-channel laser-Doppler anemometry. Proc., 6th Symp. On Turbulence, Rolla, Mo.

Durst, F., H. Kikura, I. Lekakis, J. Jovanovic and Q. Ye, 1996. Wall shear stress determination from near-wall mean velocity data in turbulent pipe and channel flows. *Exp. Fluids*, 20, pp. 417-428.

Durst, F., A. Melling and J. H. Whitelaw, 1976. *Principles and practise of laser-Doppler anemometry*. London: Academic Press.

FIDAP Users Manual, 1996. Fluent, Inc. Hanover, NH.

Fitzgerald, J. A., and S. V. Garimella, 1996. Flow field measurements in confined and submerged jet impingement. Proc., Nat. Heat Transfer Conf., ASME HTD-Vol. 333, volume 2, pp. 121-129.

Fitzgerald, J. A., and S. V. Garimella, 1998. A study of the flow field of a confined and submerged impinging jet. *Int. J. Heat Mass Transfer*, 41, pp. 1025-1034.

Guezennec, Y. G., R. S. Brodkey, N. Trigui and J. C. Kent, 1994. Algortihms for fully automated three-dimensional particle tracking velocimetry. *Exp. Fluids*, 17, pp. 209-219.

Guezennec, Y., and N. Kiritsis, 1990. Statistical investigation of errors in particle image velocimetry. *Exp. Fluids*, 10, pp. 138-146.

Hanjalic, K., 1999. Second-moment turbulence closures for CFD: Needs and prospects. *Int. J. Comp. Fluid Dyn.*, 12, pp. 67-97.

Kasagi, N., and K. Nishio, 1991. Probing turbulence with three-dimensional particle-ttracking velocimetry. *Exp. Ther. Fluid Sci.*, 4, pp. 601-612.

Kays, W. M., 1966. *Convective heat and mass transfer*. New York: McGraw-Hill.

Kays, W. M., and M. E. Crawford, 1980. *Convective heat and mass transfer, 2nd Ed.* New York: McGraw-Hill.

Kent, J. C., N. Trigui, W.-C. Choi, Y. G. Guezennec and R.S. Brodkey, 1993. Photogrammetric calibrations for improved three-dimensional particle tracking velocimetry (3-D PTV). SPIE Proc. 2005, pp. 400-412.

Langhaar, H. L., 1942. Steady flow in the transition length of a straight tube. *J. Appl. Mech.*, 9, pp. A55-A58.

leWalle, J., D. E. Ashpis and K.-H. Sohn, 1997. Demonstration of wavelet techniques in the spectral analysis of bypass transition data. NASA TP-3555.

Lindgren, E. R., 1953. Some aspects of the change between laminar and turbulent flow of liquids in cylindrical tubes. *Arkiv Fysik*, 7, p. 293.

MacManus, D., J. Eaton, R. Barrett, J. Rickards and C. Swales, 1996. Mapping the flow field induced by a HLFC perforation using a high resolution LDV. AIAA paper 96-0097.

McCreery, G. E., 1999. Inner vortex formation in the flow visualization apparatus inlet plenum. Informal memorandum, INEEL, June.

McEligot, D. M., and H. Eckelmann, 2001. Laterally converging flows: Part 3. Mean turbulence structure in the viscous layer. Manuscript in preparation.

McEligot, D. M., L. W. Ormand and H. C. Perkins, 1966. Internal low Reynolds number turbulent and transitional gas flow with heat transfer. *J. Heat Transfer*, 88, pp 239-245.

McIlroy, H.M., 2000, Visualization of the Effect of a Surface Reaction on Flow Over a Flat Plate, MS thesis, University of Idaho.

Moin, P. and K. Mahesh, 1998. Direct numerical simulation : A tool for research. *Ann. Rev. Fluid Mech.*, 30, pp. 539-578.

Morris, G. K., and S. V. Garimella, 1996. Orifice and impingement flow fields in confined jet impingement. Proc., Nat. Heat Transfer Conf., ASME HTD-Vol. 324, volume 2, pp. 101-106.

Morris, G. K., and S. V. Garimella, 1998. Orifice and impingement flow fields in confined jet impingement. *J. Elec. Packaging*, 120, pp. 68-72.

Morris, G. K., S. V. Garimella and J. A. Fitzgerald, 1998. Improved predictions of the flow field in submerged and confined impinging jets using the Reynolds stress model. Proc., 6th Intersociety Conference on Thermal and Thermomechanical Phenomena in Electronic Systems (ITherm'98), IEEE, Seattle, May, pp. 362-370.

Orr, B., E. Thomson and R. S. Budwig, 1997. Drakeol 5 thermophysical property measurements. Technical report, Mech. Engr. Dept., U. Idaho.

Parker, J., and P. Merati, 1996. An investigation of turbulent Taylor-Couette flow using laser Doppler velocimetry in a refractive index matched facility. *J. Fluids Engr.*, 118, pp. 810-818.

Patel, V. C., and M.R. Head, 1969. Some observations on skin friction and velocity profiles in fully developed pipe and channel flows. *Fluid Mech*., 38, pp. 181-201.

Resnikoff, H. L., and R. O. Wells, 1998. *Wavelet analysis.* Berlin: Springer.

Reynolds, H. C., 1969. Internal low Reynolds number turbulent heat transfer. Ph.D. thesis, Univ. Arizona.

Reynolds, H. C., M. E. Davenport and D. M. McEligot, 1968. Velocity profiles and eddy diffusivities for fully developed turbulent, low Reynolds number pipe flow. ASME Paper 68-WA/FE-34 .

Rotta, J. C., 1956. Experimentteller Beitrag zur Entstehung turbulenter Strömung in Rohr. *Ingenieur-Archiev*, 24, p. 258.

Satake, S.-I., T. Kunugi, A. M. Shehata and D. M. McEligot, 2000. Direct numerical simulation on laminarization of turbulent forced gas flows in circular tubes with strong heating. *Int. J. Heat Fluid Flow*, 21, pp. 526-534.

Schlichting, H., 1979. *Boundary layer theory, 7th ed*. New York: McGraw-Hill.

Schwartz, A. C., M. W. Plesniak and S. N. B. Murthy, 1999. Turbulent boundary layers subjected to multiple strains. *J. Fluids Eng.*, 121, pp. 526-532.

Shehata, A. M., 1984. Mean turbulence structure in strongly heated air flows. Ph.D. thesis, Univ. Arizona.

Shehata, A. M., and D. M. McEligot, 1998. Mean turbulence structure in the viscous layer of strongly-heated internal gas flows. Part I: Measurements. *Int. J. Heat Mass Transfer*, 41, pp. 4297-4313.

Sparrell, J. K., 1995. Letter, Sparrell Engineering Research Corporation, P.O. Box 130, Damariscotta, Maine 04543, 14 March.

Smith, A. M. O., 1960. Remarks on transitions in a round tube. *J. Fluid Mech.*, 7, pp. 565-576.

Stoots, C. M., S. Becker, K. G. Condie, F. Durst and D. M. McEligot, 2001. A large-scale matched-index-of-refraction flow facility for LDA studies of complex geometries. *Exp. Fluids*, 30, pp. 391-398.

Taylor, G. I., and G. K. Batchelor, 1949. The effect of wire gauze on small disturbances in a uniform stream. *Quarterly J. Mech. Appl. Math.*, 2, Pt. 1, pp. 1-29.

Thompson, B. E., O. Bouchery and K. D. Lowney, 1995. Refractive-index-matching laser velocimetry for complex nozzle entrance flow. *Laser Anemometry - 1995*, ASME FED-Vol. 229, pp. 365-370.

Tritton, D. J., 1977. *Physical fluid dynamics.* New York: Van Nostrand Reinhold.

Tufillaro, N. B., T. Abbott and J. Reilly, 1992. An experimental approach to nonlinear dynamics and chaos. Redwood City, Ca.: Addison-Wesley.

Wilcox, D.C., 1993, *Turbulence Modeling for CFD*, DCW Industries, La Cañada, California.

Yanta, W. J., and R. A. Smith, 1973. Measurements of turbulence-transport properties with a laser Doppler velocimeter. AIAA paper 73-169.